RIGIDITY PERCOLATION IN DISORDERED FIBER SYSTEMS: THEORY AND APPLICATIONS

Samuel Blackwell Heroy

A dissertation submitted to the faculty of the University of North Carolina at Chapel Hill in partial fulfillment of the requirements for the degree of Doctor of Philosophy in the Department of Mathematics.

Chapel Hill
2018

Approved by:

Peter J. Mucha

M. Gregory Forest

Daphne Klotsa

David Adalsteinnson

Theo J. Dingemans

ABSTRACT

Samuel Blackwell Heroy: Rigidity Percolation in Disordered Fiber Systems: Theory and Applications
(Under the direction of Peter J. Mucha)

Nanocomposites, particularly carbon nanocomposites, find many applications spanning an impressive variety of industries on account of their impressive properties and versatility. However, the discrepancy between the performance of individual nanoparticles and that of nanocomposites suggests continued technological development and better theoretical understanding will provide much opportunity for further property enhancement. Study of computational renderings of disordered fiber systems has been successful in various nanocomposite modeling applications, particularly toward the characterization of electrical properties. Motivated by these successes, I develop an explanatory model for 'mechanical' or 'rheological percolation,' terms used by experimentalists to describe a nonlinear increase in elastic modulus/strength that occurs at particle inclusion volume fractions well above the electrical percolation threshold. Specifically, I formalize a hypothesis given by Penu et al. (2012), which states that these dramatic gains result from the formation of a 'rigid CNT network.' Idealizing particle interactions as hinges, this amounts to the network property of *rigidity percolation*—the emergence of a giant component (within the inclusion contact network) that is not only connected, but furthermore the inherent contacts are patterned to constrain all internal degrees of freedom in the component.

Rigidity percolation has been studied in various systems (particularly the characterization of glasses and proteins) but has never been applied to disordered systems of three-dimensional rod-like particles. With mathematically principled arguments from *rigidity matroid theory*, I develop a scalable algorithm (*Rigid Graph Compression*, or *RGC*), which can be used to detect rigidity percolation in such systems by iteratively compressing provably rigid subgraphs within the rod contact networks. Prior to approaching the 3D system, I confirm the usefulness of *RGC* by using it to accurately approximate the rigidity percolation threshold in disordered systems of 2D fibers—

achieving $< 1\%$ error relative to a previous exact method. Then, I develop an implementation of *RGC* in three dimensions and determine an upper bound for the rigidity percolation threshold in disordered 3D fiber systems. More work is required to show that this approximation is sufficiently accurate—however, this work confirms that rigidity in the inclusion network is a viable explanation for the industrially useful mechanical percolation. Furthermore, I use *RGC* to quantitatively characterize the effects of interphase growth and spatial CNT clustering in a real polymer nanocomposite system of experimental interest.

ACKNOWLEDGEMENTS

From my advisors, Drs. Peter J. Mucha and M. Gregory Forest, I simply could not ask anything more. How does one get two top tier advisors to guide his or her doctoral study? I have no idea, but it happened to me, and it will shape not only this research, but my entire career. In addition to their formal involvement in my PhD committee, the rest of my committee has also been indispensable to my research and each member has been a joy to work with. Dr. Daphne Klotsa's course on soft matter research helped me to understand how geometry underplays a large body of the materials research canon, besides being one of the most enjoyable classes I have had in graduate school. Both she and Dr. Theo Dingemans, professors in the Applied Physical Sciences department at UNC, have provided great and advice helped me guide my research towards realistic applications as part of a mathematics/applied physical sciences collaborative group. While Dr. David Adalsteinsson has been less directly involved with my research, he has proved very helpful whenever I have met with him, and his introductory course on scientific computation has helped guide my overall understanding of this field.

Several people have contributed greatly to the development of my research and scholarly activity over the years—first and foremost, Drs. Dane Taylor (SUNY-Buffalo) and Feng "Bill" Shi, have been highly involved in my research as postdoctoral research associates and as young faculty members. In particular, the idea of rigid graph compression was originally conceived by Dr. Taylor, while much of the code I use has roots in Dr. Shi's work. Dr. Maruti Hegde, a staff scientist working for Dr. Dingemans, has provided great scientific understanding, while Ryan Fox and Minzhi Jiang, graduate students in the Applied Physical Sciences department, have done the same within our mathematics/applied physical sciences collaborative group. Laurie Straube, Sara Kross, and Jean Foushee-Tyson (staff in UNC mathematics office) have been incredibly helpful in constantly looking out for me as well as all the students within our department over these five years.

I am also grateful for the support of various friends in the UNC community within and outside of the math department, as they have enriched my experience here and supported my study, either

academically or simply morally—especially, in alphabetical order—Manuchehr Aminian, Aaron Barrett, Dr. Nicholas Battista, Francesca Bernardi, Emma Buckingham, Brandon Byers, Alyssa Byrnes, Martin Dewitt, Colin Guider, Dr. Alex Hoover, Dr. Caitlin Hult, Zeliha Kihiliç, Dr. Michael Malahe, Laura Manuel, Katri Morgan, Dr. John Palowitch, Jacob Perry, Dr. Ian Phillipe, Andrew Prudhom, David Raps, Dr. Quentin Robinson, Sean Rogers, Dr. Saray Shai, Alexis Sparko, Dr. Natalie Stanley, Aditi and Shirish Sundareson, Sterling Swygert, Charlie Talbot, Ben Vadala Roth, William Weir, Caroline Yang,... Finally, of course none of this would be possible without the full support of my family–Anna, Bill, Rob, Katie, Alex, Jessica, Katie, and Gigi.

The research reported in Chapters 2 and 3 of this dissertation has been submitted for publication to the *SIAM* journal: *Multi-scale Modeling and Simulation*. The research reported in Chapter 4 is in preparation for a journal (which one is to be decided). I hope to expand the research in Chapter 5 for a future publication. All of this work has been partially supported by the Army Research Office under grant W911NF-16-1-0356.

PREFACE

In between college and enrolling in a doctoral program, I was a middle/high school math teacher in various Title I schools in Nashville, Tennessee (the title indicates that a high percentage of students come from low income backgrounds). I wish I could offer some bright story about how I made a great impact on the lives of students from all of the five schools I worked at across the Metropolitan Nashville Public Schools system. However, the truth is that I more or less applied to graduate school to escape the demands of being an inexperienced teacher who had no idea how to simultaneously manage a room full of kids, almost all of whom were below grade level and many of whom carried serious issues from outside of the school halls with them. This dissertation is on one hand dedicated to all of the people who supported me in that more difficult time of my life, both helping me to do the best I could in that role and also guiding me to find something better suited to my interests and abilities. That of course includes first my family and close friends, as well as various teachers and principals (some more than others) in the public school system, and the Teach for America staff in the Greater Nashville Office. On the other hand, I dedicate this dissertation to the many students I had—given the difficult learning environments and external quandaries that children in low-income communities are routinely put in, it is incredible how many are able to even make it through the education system and it is awe-inspiring what they are able to accomplish. With all of the support I have been given over the years, I feel it incumbent on me to not forget that educational disparity as I continue along my career path, and to one day do something that may help to reverse it.

TABLE OF CONTENTS

LIST OF FIGURES

LIST OF ABBREVIATIONS AND SYMBOLS

γ_c	Radius of carbon nanotubes
γ_M	Radius of Matern process seeds
γ_{max}	Radius of max crystalline growth
γ_r	Radius of interaction
$\Delta \boldsymbol{p}_{i,j}$	D-dimensional vector difference between position vectors $\boldsymbol{p}_i$ and $\boldsymbol{p}_j$
ζ	Aspect ratio
λ_s	Point process intensity
λ_d	Mean number of daughter points
μ	Average
ν	Correlation length exponent
π	Percolation probability
ρ	Configuration
Σ	Covariance matrix
ϕ	Volume fraction of particle phase
ϕ_c	Volume fraction of carbon nanotube phase
ϕ_{min}	Volume fraction of particle phase at the rigidity or contact percolation threshold
$\phi_{min,c}$	Volume fraction of particle phase at the electrical percolation threshold
$\phi_{min,r}$	Volume fraction of particle phase at the rheological percolation threshold
σ	Standard deviation
$\chi(D)$	Motions of a rigid body in D dimensions
A	Adjacency matrix
CF	Central force
CNT	Carbon nanotube
D	Number of dimensions
d_{ij}	Distance between points $\boldsymbol{p}_i$ and $\boldsymbol{p}_j$
E_{bulk}	Bulk Young's or elastic modulus
e_{ij}	Edge between vertices i and j
$G(V, E)$	Graph with vertex set V vertices and edge set E

$\boldsymbol{I_n}$	$n \times n$ identity matrix
K_n	Complete graph on n vertices
KD	K-dimensional
L	Length of domain
L_s	Length of subdomain
L_v	Length of voxel
ℓ	Length of a rod
N_c	Number of contacts
n_ℓ	Number of balls per unit length
n_r	Number of rods
NMP	N-Methyl-2-pyrrolidone
ODPA-P3	Polyetherimide 3,3',4,4'-oxdiphthalic dianhydride
$\boldsymbol{p}_i$	D-dimensional vector indicating the position of point i
PEI	Polyetherimide
q	Number density of rods
q_c	Number density of rods at the contact percolation threshold
q_{min}	Number density of rods at the rigidity percolation threshold
R	Rigid component
RGC	Rigid Graph Compression
s	Fractional distance
S_i	Number of points in a coordinate labeling for a rigid component R_i
SE(D)	Special Euclidean group in D dimensions
SWCNT	Single walled carbon nanotube
$\boldsymbol{u}_i$	D-dimensional vector indicating the velocity of point i
$\boldsymbol{u}$	$D\|V\|$-dimensional vector indicating the concatenated velocities of each point in a system
V_{crys}	Crystallinity
v	Fractional volume
$\boldsymbol{X}$	Rigidity matrix

CHAPTER 1: INTRODUCTION

> "I agree with you," replied the stranger; "we are unfashioned creatures, but half made up, if one wiser, better, dearer than ourselves– such a friend ought to be—do not lend his aid to perfectionate our weak and faulty natures. I once had a friend, the most noble of human creatures, and am entitled, therefore, to judge respecting friendship. You have hope, and the world before you, and have no cause for despair. But I—I have lost everything and cannot begin life anew. $\sim$ Mary Shelley's *Frankenstein; or, the Modern Prometheus* (1818)

1.1 Overview

In the past quarter century following their first confirmed synthesis (Iijima and Ichihashi, 1993), carbon nanotubes have received a remarkable amount of attention—alongside other promising nanoparticles—from both engineers and physical scientists. Yet while the promise of these nanoparticles is immense on account of their extremely impressive mechanical and electrical properties, the industrial use of nanocomposites (particularly carbon nanocomposites) has not at this point matched the hopes of many researchers. While the properties of individual carbon nanotubes (CNTs) are unparalleled, the bulk properties of carbon nanocomposites are less impressive (though often still quite useful). This discrepancy is thought to result from CNTs' tendency to bundle and agglomerate, as well as to the lack of interfacial bonding between the CNTs and the polymer matrix (Coleman et al., 2005). Despite these hindrances, CNTs have use in many present-day applications and much research is dedicated to finding novel applications for carbon nanocomposites, as well as other nanocomposites (see De Volder et al. 2013 for a comprehensive discussion of applications). Coinciding with this persistent engineering interest is increased attention to theoretical modeling of nanocomposites (see Coleman et al. 2004; Fralick et al. 2012; Shi et al. 2014, as well as many other studies). Because nanocomposites are inherently complex, highly disordered systems, theoretical and computational studies require new methods which account for the interactions of the many individual particles, yet remain valid and computationally tractable at large system sizes.

My doctoral research in particular focuses on using network scientific tools to assess mechanical properties of nanocomposites. From simple renderings of disordered particle systems, I look to capture within their totalities of particle interactions emergent network properties, which I hypothesize

give rise to measurable properties. The majority of this research is dedicated to studying network properties—in particular *rigidity percolation* (which I introduce in Sec. 1.3)—of these simple computational renderings. In the introductory chapter of this dissertation, I will first outline in Sec. 1.2 successes related to modeling of nanocomposites' electrical property properties, which motivate my analogous study of mechanical properties. Then, I detail experimental results that are of interest to my study in Sec. 1.3, before moving to lay out the organization of this dissertation in Sec. 1.4.

1.2 Modeling of nanocomposites' electrical properties

High aspect ratio particles (e.g., thin rods) of nanoscopic or microscopic scales are routinely incorporated into polymeric host materials to enhance attributes such as electrical and thermal conductivity, charge storage, and mechanical resilience. These composites often exhibit a nonlinear response with respect to the density (measured by volume fraction, ϕ) of rods or other filaments: the property gain scales linearly at small volume fractions, then increases dramatically as ϕ passes through a critical threshold ϕ_{min}. When considering the conductivity of a poorly conducting polymer enhanced with highly conductive rods, this sharp transition is associated with 'contact percolation,' wherein interacting rods form a giant, spatially extended network component (Shi et al., 2014).

In the simplest conception of contact percolation, two perfectly conducting rectangular plates are placed at each end of a three dimensional domain and highly conductive nanoparticles are dispersed within the domain. One technique for studying this system is to idealize it as a three-dimensional lattice, wherein sites are occupied (conducting) with some probability—this approach has been studied in various forms for many years (Stauffer and Aharony, 1992), and has been successful in reproducing experimentally observed bulk conductivity properties (Shi et al., 2013). However, the more faithful representation involves Monte Carlo simulation of randomly placed 'sticks' (capped cylinders, or spherocylinders) of some aspect ratio—study of this system traces back to Balberg and Binenbaum (1984), who first determined the nature of the the percolation threshold's dependence on aspect ratio and macroscopic anisotropy. In either case, percolation theory has proven successful in capturing the dramatic power-law scaling of conductivity enhancements at and above the percolation threshold (Shi et al., 2013, 2014).

Beyond simply identifying whether or not a (nano)composite has percolation in its inclusion phase, methods from network science and graph theory are useful in making tractable the computa-

tional problems that arise in studying electrical properties of large systems. In particular, Shi et al. (2013, 2014) efficiently attained the current distribution of random nanorod/random lattice resister networks by solving Kirchoff's law on the subgraph given by the network's plate constrained 2-core (i.e. the component containing all nodes of degree ≥ 2 that are connected to the boundary plates). By only considering this subgraph (thereby filtering out 90% of the edges in networks near the percolation threshold), the authors were able to efficiently attain current distributions and recover bulk conductivity in sufficiently large networks without removing any current-carrying particles from the respective system of interest. Similar graph-theoretic techniques have been used to successfully capture dieletric properties (Simoes et al., 2008), as well as the relationship between system disorder and bulk conductance in real nanocomposites (Silva et al., 2011).

Another layer of complexity comes from particle anisotropy and particle distribution heterogeneity. Shi et al. (2014) explored nanorod anisotropy by using orientational probability distribution functions from kinetic Brownian rod dispersion flow codes to simulate particle distributions (Forest et al., 2004, 2008). This approach allows for accurate estimation of percolation thresholds and mean conductivity, given realistic processing conditions in sheared thin films of nanorod dispersions. Related work has examined the influence of processing conditions on percolation and conductivity in dispersions of carbon nanotubes, which have different rheological properties from their nanorod counterparts (Seidel and Puydupin-Jamin, 2011). Furthermore, this latter study implemented a multi-scale model that purportedly mimics the experimentally observed spatial agglomeration of nanotubes, in order to explain the ultra-low percolation thresholds observed in experimental data. Other simulation-based models have also accounted for spatial agglomeration of nanotubes—interestingly, one study predicts that agglomeration has a net reducing effect on conductivity in polymer nanocomposites, and claims this is the main factor in the discrepancy between observed conductivity and relevant theoretical limitations (Gong et al., 2014). Another study (in the same journal) predicts that a certain amount of agglomeration is beneficial to electrical conductivities at low volume fractions (Tarlton et al., 2017). Clearly, there is a richness of geometrical considerations to modeling real nanocomposites (polydispersity presents another), and these considerations have important implications to their electrical properties as well as general importance to the greater body of nanocomposite modeling.

1.3 Mechanical percolation

In addition to the well-understood gains in conductivity at the contact percolation threshold, a sharp rise in mechanical stability at volume fractions greater than or equal to the contact percolation threshold has been observed in numerous composite systems (Favier et al., 1995b, 1997; Liu et al., 2016; Noël et al., 2014; Zhang et al., 2013; Penu et al., 2012). However, characterization of the physical mechanism underlying this so-called 'mechanical percolation' remains an open problem—no emergent phenomenon (akin to contact percolation) in rod or rod-polymer interactions has been shown to trigger this macroscopic behavior. Motivated by the success in network-based modeling of nanocomposites' electrical properties, my ultimate goal is to develop network-based computational tools that can be used to assess nanocomposites' electrical properties.

1.3 Experimental characterizations

The nature of mechanical percolation varies considerably with the complexity of the composite system. As an example, cellulose fibers (or whiskers) obtained from tunicin have high tensile modulus ($\sim$120-150 GPa) and high aspect ratio (10-20 nm width and 100 nm to several μm length) (Favier et al., 1997, 1995b). In cellulose fiber-reinforced composites, generic percolation models with fitting parameters tuned to data accurately describe the relationship of different moduli to the volume fraction ϕ of cellulose fibers (Favier et al., 1997, 1995a; Ouali et al., 1991). The reactivity of readily available hydroxyl groups along the whiskers makes hydrogen bonding interactions especially favorable, such that contacts transmit bending modes in addition to compression modes, thereby fixing the angles between contacting particles (Favier et al., 1997; Kalia et al., 1976). Thus, the presence of a spatially extended network component of contacting particles is posited to drastically increase the stiffness of these composite materials, consistent with experimental results as well as with physically-based two-dimensional simulations (Favier et al., 1995b, 1997; Wilhelm and Frey, 2003). In other systems, however, attractive forces are relatively soft and only transmit compressive and tensile forces, so that contact percolation alone is not enough to mechanically stabilize the network and additional constraints are needed. In such systems, experiments show that mechanical percolation occurs at higher volume fractions than electrical percolation, both when the reinforcement particles are of high aspect ratio (Celzard et al., 2001; Liu et al., 2016; Penu et al., 2012), and otherwise (Niklaus and Shea, 2011; Noël et al., 2014).

The mechanical properties of any composite material depend on the specific properties of each phase, the volume fraction as well as morphology of the reinforcing components, and the interfacial properties (Kalia et al., 1976). Homogenization models, such as the Halpin-Tsai equations, have been successfully adapted to a variety of systems with different morphologies and interfacial properties to predict modulus as a function of volume (or weight) fraction of the reinforcing phase (Coleman et al., 2006; Affdl and Kardos, 1976). Micromechanical modeling efforts have provided more sophisticated and accurate models, which take into account the interplay between random microstructure and interphase (Baxter et al., 2016; Baxter and Robinson, 2011; Fralick et al., 2012; Qiao and Brinson, 2009). While many different classes of mechanical models are generally useful and have more immediate predictive capability than my study here, none of these demonstrate an explicit mechanism for the emergent nonlinear gain in mechanical properties generated by favorable interactions between particles within the reinforcing phase.

1.3 Rigidity: a microstructural mechanism for mechanical percolation?

In my work, I look to explore a hypothesis posed by Penu et al. (2012), who explored the relationship between electrical and mechanical ('rheological' in their study) percolation thresholds in an ensemble of studies of CNT-based nanocomposites. In some of these studies, the electrical percolation threshold $\phi_{min,c}$ occurrs at lower density than the rheological percolation threshold $\phi_{min,r}$—in others, the reverse is true. Attempting to reconcile this disparity, Penu et al. (2012) proposed that there is a 'soft' rheological percolation threshold at low $\phi(< \phi_{min,c})$, and another 'hard' one at higher $\phi(> \phi_{min,r})$. The lower threshold is posited as a transition wherein nanotubes become close enough to be connected by a polymer macromolecular coil, while the higher threshold is posited as emerging from the presence of a rigid network. The study of Penu et al. (2012) does not explicitly define a rigid network of CNTs, but rather the authors cite a theoretical prediction given by Celzard et al. (2001) for the ratio of the 'hard' rheological percolation threshold ('vectorial percolation') to the electrical percolation threshold ($\phi_{min,r}/\phi_{min,c} = \frac{D^2-1}{2D-1}$ for dimension D, 1.6 for $D = 3$). While some experimental measurements fall in the range of this ratio, this macroscopic theoretical prediction—derived from an analysis of glass/crystal systems—falls short in many systems wherein the inclusions have high aspect ratio (i.e. random two dimensional fibers, as shown in Ch. 3) and I contend that a simulation-based characterization will give rise to a more powerful prediction of rheological/mechanical/vectorial percolation.

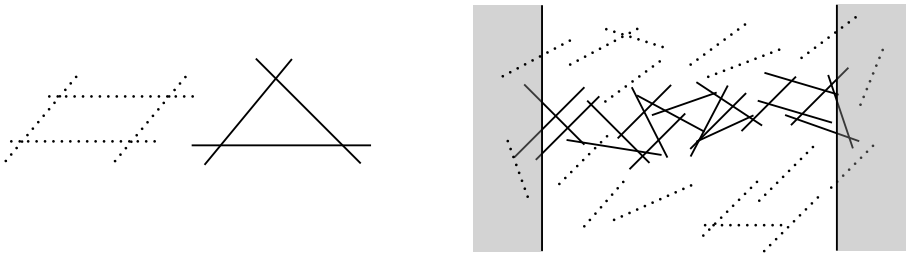

Figure 1.1: **Rigidity in two-dimensional rod-hinge systems.** *Left*: Supposing that rods interact as hinges at intersections, four rods connected pairwise in two dimensions are 'floppy' (dotted) in that they may deform through different interior angles, whereas three rods connected pairwise are 'rigid' (solid). *Right*: A large component of mutually rigid rods may add mechanical stability to a host composite. I use rigidity characterization algorithms to detect the presence of such a component connecting two boundaries (vertical rods) bounding a large computational domain. In order to keep the rod distribution uniform throughout the (white) domain, I allow rods to be placed in the 'buffer' regions (grey rectangles) on the exterior sides of the boundaries.

It is my hypothesis that mechanical or rheological percolation occurs when the reinforcing phase has sufficient volume fraction so as to coalesce into a giant *rigid scaffold* or *spanning rigid component*, wherein the individual reinforcing particles are not only in contact, but furthermore the constraints that result from these connections are sufficient to eliminate any nontrivial degrees of freedom ('floppy modes') within the component (see Figure 1.1). My study is motivated by the success in using Monte Carlo simulations of nanoparticle dispersions to characterize electrical properties through the resultant networks of particle interactions (as discussed in the previous subsection). I use a similar network representation of nanoparticle interactions to characterize the dispersions' mechanical properties, assuming that stiff rods interact solely through pairwise attractive contacts in an otherwise soft medium.

As will be discussed in Ch. 2, a number of studies have been devoted to the characterization of *rigidity* and *rigidity percolation*, but none of the associated methods have proven adequate for large three-dimensional rod systems. Unlike previous studies of rigidity percolation, my work takes the perspective that large rigid scaffolds are 'built up' from simple topological patterns that apply at any scale. With this perspective, I identify and prove primitive *rigid motifs*—specific contact rules that determine when a small set of interacting rigid components are together rigid—so that these motifs may be condensed into larger rigid components. In two dimensions, these motifs do not require specification as to whether the separate components be individual particles or compositions themselves; and only minimal specification as to whether these particles be rods,

ellipsoids, curvilinear fibers, whiskers, etc. In three dimensions, the problem is only slightly more complicated in that axisymmetric particles have one less degree of freedom (5) than more complex rigid bodies which lack axisymmetry (6)—giving rise to different treatment between the base particles and compositions of particles. The algorithm I develop using this 'topological building blocks' perspective—*rigid graph compression* (RGC)—is therefore applicable to any number of spatial dimensions upon selection of appropriate motifs, and is also applicable to systems of varying particle shape (nanorods, ellipsoids, curvilinear fibers, etc.).

I use the term 'disordered particle systems' to denote physical networks of randomly distributed, high aspect ratio, and completely inflexible particles—this study is specifically oriented towards the study of cylindrical particles (which may be used to model stiff fibers, rods, whiskers, nanotubes, etc.). In two dimensions, these cylinders may be infinitesimally thin line segments which physically intersect (termed 'Mikado models' in Head et al. 2003a,b; Wilhelm and Frey 2003), while in three dimensions the cylinders must have finite radii to intersect. I model contacts between particles as hinges, such that intersecting particles may pivot about their contact points, but Van der Waals forces, friction, etc. keep them in contact at these points (as in Figure 1.1). When a component of particles has enough contacts such that these constraints keep all the particles fixed relative to each other, they may only move as a single *rigid component*, and I refer to the rods in this body as being mutually rigid.

This previous discussion assumes that all contacts have the effect of enhancing mechanical properties—however, an abundance of constraint-forming contacts limits the random motion of particles and thus adds stress to the system. From this perspective, rigidity percolation constitutes the onset of stress, as any further contacts have an effect of adding constraints beyond those required to fully constrain a spatially extending component's internal degrees of freedom. The perspective required for applications naturally depends on the types of particle interactions and other considerations in the system of interest. In any case, development of rigidity percolation detection software can help guide understanding of nanocomposites' mechanical properties and provide a basis for optimizing such properties.

1.4 Outline of the dissertation

In Ch. 2, I discuss existing methods for rigidity characterization, as well as their strengths and drawbacks for modeling disordered particle (rod/fiber) systems, before introducing the algorithm

central to this dissertation, rigid graph compression. In Ch. 3, I apply this algorithm to two-dimensional fibers, showing that it can be used to approximate the rigidity percolation threshold to within 1% accuracy relative to a previous exact method. In Ch. 4, I apply RGC to systems of three-dimensional fibers, wherein no previous methods exist for accurate characterization of rigidity percolation, and establish an upper bound for the associated rigidity percolation threshold. Moreover, I outline methods that can aid in establishing—as well as improving—the tightness of this upper bound estimation to the true threshold. In Ch. 5, I use this analysis of 3D fiber systems, as well as other methods, to assess experimental results for a nanocomposite of interest. Finally, I conclude this dissertation by summarizing these findings and discussing important next steps for simulation-based study of nanocomposite systems.

CHAPTER 2: RIGID GRAPH COMPRESSION

> Chemistry is that branch of natural philosophy in which the greatest improvements have been and may be made; it is on that account that I have made it my peculiar study; but at the same time, I have not neglected the other branches of science. A man would make but a very sorry chemist if he attended to that department of human knowledge alone. If your wish is to become really a man of science and not merely a petty experimentalist, I should advise you to apply to every branch of natural philosophy, including mathematics.
> $\sim$ Professor Waldman

2.1 Overview

In this chapter, I develop a methodology for studying rigidity in disordered or 'off-lattice' systems of interacting particles, which will be studied in both Chapters 3 and 4. While these results for 2D and 3D fiber systems are specific case studies, I note that the algorithm developed in this section is applicable to systems in which the disordered particles have any shape (e.g. ellipsoids, spheres, etc.), so long as these base particles have no internal degrees of freedom. Regardless of the dimension, a *configuration*, or realization of a randomly disordered particle dispersion, will be denoted ρ–this encodes geometrical information (spatial centers and orientations), which informs topological information. More specifically, a contact graph is extracted wherein nodes correspond to particles and edges correspond to contacts between those particles. Rigid Graph Compression (RGC) will be used to determine which particles in a configuration ρ are rigid with respect to one another (locally), and to determine the sizes of components of mutually rigid particles in ρ. After attaining this latter information for systems of many different domain sizes and particle densities, it is possible to estimate the rigidity percolation threshold and associated correlation coefficient (as will be done in Sec. 3.4 and 4.4.2).

Importantly, though RGC is indiscriminate to the shape of particle under consideration, it is only relevant to systems wherein contacts between particles are hinge-like—that is, if two particles i and j contact at some point $\boldsymbol{p}$, then they can rotate about $\boldsymbol{p}$ but stay fixed relative to $\boldsymbol{p}$. More precisely, the distance from $\boldsymbol{p}$ to any point in i and j stays fixed for all time, but the distance between some point $\boldsymbol{p_i} \neq \boldsymbol{p}$ in i to a point $\boldsymbol{p_j} \neq \boldsymbol{p}$ in j may vary as a function of time. This condition is a

simplistic idealization of the 'soft' attractive forces present in networks of carbon nanotubes and other inclusions (see Sec. 1.3.1).

2.2 Previous methods

Many previous studies have been used to consider the rigidity of disordered particle systems, particularly in two dimensions. Here, I present the methods of these studies (Secs. 2.2.1–2.2.3), and then attend to their efficacies for studying rigidity percolation in disordered fiber systems, as well as to the information structure required for algorithmic implementation (2.2.4).

2.2 Maxwell counting

The oldest (and simplest) technique for studying rigidity is Maxwell counting, which predicts that a system is rigid if the number of constraints is equal to the number of inherent degrees of freedom were the system's particles all completely unbound (Maxwell, 1864). This condition can best be represented using central force (CF) networks–simple graphs $G(V, E)$ embedded in D-dimensional Euclidean space wherein the set of edges ('bonds'), E, denotes fixed distances between members of the vertex set, V ('nodes' or 'atoms'). In this representation, Maxwell counting translates to the equality $|E| = D|V| - \chi(D) \approx D|V|$, where $\chi(D)$ is equal to the number of rigid motions of the system in D dimensions.

In a previous study, this condition has been applied to study rigidity percolation in 2D 'random networks of stiff fibers,' with number density of unit-length rods $q = n_r/L^2$, where n_r is the number of rods, and L is the length of the simulation area (Latva-Kokko and Mäkinen, 2001; Latva-Kokko et al., 2001). In this system, the number of contacts N_c scales linearly with the total number and density of rods (Kallmes and Corte, 1960):

$$N_c \approx n_r q/\pi \tag{2.1}$$

In two-dimensional space, a contact between two rods constrains two degrees of freedom. Assuming without justification (and incorrectly) that all such constraints are independent of one another, one infers that the network becomes rigid at the rigidity percolation threshold $q_{\min}$ satisfying:

$$3n_r = 2N_c = \frac{2n_r q_{\min}}{\pi} \Rightarrow q_{\min} = \frac{3}{2}\pi \doteq 4.71\,. \tag{2.2}$$

As I will show in Ch. 3, the density predicted for rigidity percolation based on Maxwell counting in this system is far too low—indeed, it is even lower than the contact percolation threshold for two-dimensional isotropically random rod systems ($q_c \doteq 5.71$) (Pike and Seager, 1974). Importantly, the number of contacts per rod obeys a Poisson distribution, and thus many constraints redundantly bind the same free motions within the system ('floppy modes'), while others are left unconstrained (Latva-Kokko and Mäkinen, 2001; Latva-Kokko et al., 2001). In other systems—such as glasses and crystals (trivially), these redundant constraints are apparently less common, as the Maxwell prediction is more accurate (Phillips and Thorpe, 1985).

2.2 Laman, the pebble game, and Henneberg constructions

The inadequacy of Maxwell's condition in disordered systems necessitates a description accounting for dependence between constraints. *Laman's condition* can be used to determine when the constraints in a 2D CF network are independent (Laman, 1970).

Theorem 2.1 (Laman's Condition)**.** *The edges of a graph $G(V, E)$ are independent in two dimensions if and only if no subgraph containing V' vertices has more than $2V' - 3$ edges. If a graph has exactly $2V' - 3$ edges within each subgraph on V' vertices, then it is called a Laman graph.*

Rigid graph characterization based on direct application of Laman's Condition would require iterating tests upon every subgraph of a CF network G, which would be computationally hopeless for all but the smallest systems. However, an equivalent formulation of this condition is the following: the edges of $G(V, E)$ are independent in two dimensions if and only if, for each edge $e_{ij} \in E$, the graph formed by adding three new edges between i and j has no subgraph on V' nodes with more than 2V' edges. Jacobs and Thorpe developed this corollary into a "pebble game" test for independence of edges with computational complexity that scales in the worst case as $\mathcal{O}(|V|^{1.2})$ (Jacobs and Thorpe, 1995; Jacobs and Hendrickson, 1997). In 2D CF networks, each node is assigned a pair of 'pebbles' to represent the two degrees of freedom of a point in a plane. Each bond between these nodes pins down one of their allotted pebbles, so long as there are sufficient pebbles for each bond—otherwise, some edges are redundant, or 'stressed.' Once the pebble game is implemented, the locations of free pebbles and enumeration of independent edges allow for decomposition of the network into sets of mutually rigid nodes, alongside an accurate count of the system's net degrees of freedom. The pebble game has been applied to a variety of systems, including CF networks with

random topologies (e.g. Erdős Rényi graphs), wherein Thorpe *et al.* show that networks undergo a rigidity transition as the mean coordination number (average degree) approaches ≈ 4 (Thorpe et al., 1999).

The pebble game is deconstructive in that it is used for partitioning a graph into rigid and floppy components. An alternative goal is the construction of rigid graphs, which can be accomplished for 2D CF networks using *Henneberg constructions*, inductive rules for the construction of Laman graphs (Henneberg, 1911). Constructions begin with an edge connecting two vertices (a trivially rigid graph). Then, the following steps are repeated iteratively: a new vertex is added, adjoined either (a) to two vertices via two new edges; or (b) to two previously adjacent nodes, while the old edge between these latter nodes is severed and a third edge is placed between the new node and another previously existing node. As noted above, every Henneberg construction is a Laman graph; but perhaps more surprisingly, every Laman graph can be realized by Henneberg constructions (Tay and Whitely, 1985).

2.2 Rigidity matroid theory

Unlike the approaches described above, rigidity matroid theory uses a graph's embedding in Euclidean space, or 'framework' (equivalent to a configuration), $\rho(G)$, to characterize its rigidity through the language of linear algebra (Cucuringu et al., 2012; Graver, 1991; Hendrickson, 1992). Consider the set of node positions to be a dynamical system such that $\boldsymbol{p}_i(t)$ is the D-dimensional position of node i at time t. The condition that each edge $e_{ij} \in E$ maintains a fixed distance d_{ij} between nodes i and j requires $\sum_{D'=1}^{D} |p_i^{D'}(t) - p_j^{D'}(t)|^2 = d_{ij}^2 \;\; \forall e_{ij} \in E$. Since this quadratic system is not computationally convenient, it is convenient to linearize by differentiating each side with respect to time, obtaining:

$$(\boldsymbol{p}_i(t) - \boldsymbol{p}_j(t)) \cdot (\boldsymbol{u}_i(t) - \boldsymbol{u}_j(t)) = 0 \qquad \forall e_{ij} \in E \tag{2.3}$$

where $\boldsymbol{u}_i(t) = d\boldsymbol{p}_i(t)/dt$ is the instantaneous velocity of node i. The totality of these constraints informs an $|E| \times D|V|$ matrix, $\boldsymbol{X}$—the rigidity matrix of $\rho(G)$—satisfying $\boldsymbol{X}\boldsymbol{u} = \boldsymbol{0}$, where $\boldsymbol{u}$ is the $D|V|$-vector of velocities and $\boldsymbol{0}$ is the corresponding all-zero vector. A vector $\boldsymbol{u}$ satisfying $\boldsymbol{X}\boldsymbol{u} = \boldsymbol{0}$ is an *infinitesimal motion* of $\rho(G)$, and the right nullspace of $\boldsymbol{X}$ includes the full set of such motions. If G is embedded in Euclidean space $\mathbb{R}^D$ and the right nullspace of $\boldsymbol{X}$ spans only the $D(D+1)/2$

rigid-body motions of translation and rotation, the framework $\rho(G)$ is said to be *infinitesimally rigid*. Otherwise, $\rho(G)$ is *infinitesimally flexible*.

Importantly, it has been shown generically that if a framework $\rho(G)$ is infinitesimally rigid, then all other realizations of G are infinitesimally rigid (Gluck, 1975). Therefore, one can (generically) infer rigidity from the topology of a graph itself, rather than from any particular embedding in space. We note that this argument breaks down when at least one nontrivial minor of $\boldsymbol{X}$ has a zero determinant—however, these cases occur with probability zero in disordered particle systems. Practically, determining the rigidity of $\rho(G)$ thus reduces to computing the rank of $\boldsymbol{X}$, and using the rank nullity theorem to then determine the dimension of the matrix's null space, which corresponds injectively to the underlying graph's degrees of freedom count.

2.2 Relationship to rigidity percolation in disordered Particle systems

These prior methodologies have been central to the study of graph rigidity; however, none are entirely suited to study of rigidity percolation in disordered particle systems. First, the techniques described in Secs. 2.2.2–2.2.3 have been developed for CF networks; however, in disordered particle systems, the position of each contact between two particles is fixed relative to the entirety of both of these particles, which may include any number of contacts with other particles. In two studies (Latva-Kokko and Mäkinen, 2001; Latva-Kokko et al., 2001), Latva Kokko and colleagues introduce augmented constraints between second nearest neighbors to extend the pebble game to 2D disordered fiber systems, and use this extended method to determine the critical rod density of rigidity percolation as well as the scaling of rigid component size near the threshold. However, because it depends on Laman's condition for 2D graphs, the pebble game cannot extend exactly to three dimensions in its current form, and it is unclear whether any such breadth first search algorithm could even possibly account for the complicated variety of three dimensional floppy modes. Instead, the pebble game has been only approximately extended to 3D glass-like networks (Chubynsky and Thorpe, 2007); it is unclear whether or not this approximate extension can be modified for 3D disordered fiber systems, and if it indeed can, what accuracy it might obtain.

One can instead augment rigidity matroid theory for disordered systems (see Sec. 3.2). However, while rigidity matroid theory is (unlike the pebble game) valid in any number of dimensions, rigidity matrices do not offer any local information about which sets of rods are rigid relative to others. That is, while one could in principle use rigidity matrices to tally the macroscopic degrees of freedom

in various large systems, they would not immediately characterize rigidity percolation (barring an extremely exhaustive brute force search of submatrices) (Hendrickson, 1992). Furthermore, because rigidity matrices rely on the full set of particle intersection points, many of these points will be spatially close at sufficiently high particle densities, subjecting the analysis of the corresponding matrix to numerical error (Hendrickson, 1992; Cucuringu et al., 2012).

Finally, I consider another previously used technique for rigidity analysis of disordered fiber systems, in which rods are considered to be stiff springs that connect at their intersection points (Wilhelm and Frey, 2003; Head et al., 2003a,b). These points are first subjected to a perturbation (corresponding to physical deformation), and then the spring system is relaxed using nonlinear optimization. If the initial pairwise distance between two nodes is maintained after relaxation, then the points (and the rods containing them) are deemed rigid with respect to one another; otherwise, they are not. This method does allow for characterization of rigidity percolation—achieving similar results to those of the pebble game (Wilhelm and Frey, 2003)—but being a search for the "lowest point of a complicated high-dimensional valley with extremely steep slopes but hardly varying base altitude" (Wilhelm and Frey, 2003), it was observed to be highly unstable in large 2D fiber systems and has not been attempted in 3D fiber systems.

To help guide the development of scalable algorithms for rigidity analyses in both two dimensions and beyond, I highlight that there is a hierarchy of information required across these previous methods. Maxwell's counting requires only the global density of particles (q); the pebble game and Henneberg constructions require topological information, specifying which *contact points* are adjacent (i.e., an edge list or adjacency matrix); rigidity matroid theory and the spring relaxation method additionally require the *spatial locations* of particle intersection points. In the next section, I derive an alternative method that stems from rigidity matroid theory, and can therefore be generalized to higher dimensions. However, in application this method is a scalable topological algorithm that only requires a list of particle contacts instead of the full knowledge of the locations of contacts.

2.3 Motif-based rigidity decomposition

I now introduce a novel methodology for rigidity analysis of disordered particle systems in any number of dimensions with any particle shape. In Sec. 2.3.1, I adapt rigidity matroid theory (described in Sec. 2.2.3) to disordered particle systems; and in Sec. 2.3.2, I describe an algorithm that utilizes this constructive adaptation for the purpose of deconstructing disordered particle systems

into their inherent rigid components. The next two chapters will specify this algorithm for systems of fibers in two and three dimensions, and conclude with analysis of appropriate numerical results.

2.3 Rigidity matroid theory for interacting rigid components

Here, I use rigidity matroid theory to study the motions of small numbers of interacting rigid components. The motions of any rigid component in D dimensions can be fully determined from $D+1$ points contained in the component, the translations and rotations of which together generate the Special Euclidean group *SE(D)* (Cederberg, 2001). (In principle, fewer coordinates are needed if employing angular constraints, but for simplicity I choose to work with $D+1$ points.) Hence, for some rigid body $R \subset \mathbb{R}^D$, defined as the union of volumes enclosed within some integer number $n_r > 0$ of D-dimensional rods, I affix a (nonunique) *coordinate labeling* of R composed of at least $D+1$ points $\{\boldsymbol{p}_i\}$ which fully capture the rigid motions of R. Importantly, no more than two points in a coordinate labeling may be collinear, or else the coordinate labeling will only capture a subset of the rigid motions of the corresponding body. Due to the rigidity of R, the pairwise distances between the points are fixed, providing $\binom{D+1}{2}$ constraint rows in the corresponding rigidity matrix $\boldsymbol{X}$, each having the form:

$$\Delta\boldsymbol{p}_{i,j} \cdot \boldsymbol{u}_i - \Delta\boldsymbol{p}_{i,j} \cdot \boldsymbol{u}_j = 0, \tag{2.4}$$

where $\boldsymbol{u}_i$ and $\boldsymbol{u}_j$ are the instantaneous velocities corresponding respectively to points $\boldsymbol{p}_i$ and $\boldsymbol{p}_j$ affixed in R and $\Delta\boldsymbol{p}_{i,j} = \boldsymbol{p}_i - \boldsymbol{p}_j$. Note that regardless of the dimension of the rod network, if R includes only a single rod, then it has a spatial dimension 1, and so only two points are needed to specify its rigid motions.

When two or more rigid components $\{R_i\}$ interact in contact, I denote the composite system by $R_1 * R_2 * \ldots$ and the corresponding composite rigidity matrix by $\boldsymbol{X}_1 * \boldsymbol{X}_2 * \ldots$. For such systems, I construct sets of *minimal coordinate labelings*, wherein each rigid component's coordinate labeling is chosen such that interaction points between other rigid components are included wherever possible. For a given set of coordinate labelings of $\{R_i\}$, a *constraint graph* may be constructed encoding the topology of interactions (i.e., physical constraints) between the rigid components. This graph is constructed by creating for each rigid component R_i with S_i points in its coordinate labeling a (S_i)-clique—that is, an all-to-all connected subgraph. The constraint graph is defined as the union of these cliques.

The formalism above will be used in Secs. 3.2 and 4.2.2 to prove certain topological rules for aggregating rigid components into larger rigid components. These rules are encoded into *primitive rigid motifs,* which represent topological 'building blocks' of rigidity. I use the term 'primitive' because these motifs may not be decomposed into simpler motifs, yet many larger, more complicated patterns of interaction can be constructed from these motifs, analogous to the formation of Laman graphs from Henneberg constructions. In order to organize this discussion, I adopt the naming schema "*Motif* xDy" with x indicating the spatial dimension and y indicating the number of aggregating rigid components in the motif.

2.3 Algorithmic framework for Rigid Graph Compression

Whereas the language above used for rigid motif identification is constructive, the main purpose for these rigid motifs is in deconstruction of disordered particle systems into their inherent rigid components. The primitive rigid motifs described above will be used to identify large-scale rigid components agglomerated from rigid components identified at smaller scales, starting from the microscopic scale of primitive rigid motifs acting on individual particles. In so doing, it is convenient to work in terms of *contact graphs* in which each node represents a rigid component and edges indicate contacts or interactions between such components. Importantly, this network construction contrasts the *constraint graphs* described earlier (in which nodes represented coordinate labelings and edges represent rigidity constraints).

The RGC algorithm involves initialization (Step 1), followed by iterative identification and compression of rigid motifs (Steps 2 & 3): (1) given the spatial locations of a candidate set of interacting rigid particles ρ, construct a contact network of rods represented as nodes and contacts between rods represented as edges; (2) identify rigid motifs in the contact network; (3) compress each rigid motif instance into a single node, yielding a reduced set of rigid components (with weights or multi-edges corresponding to the number of contacts between the compressed components) and an updated contact network; (4) return to Step 2. The format of this algorithm can be adapted to include any number of motifs in any number of dimensions (with only slight modification). Not all rigid motifs incorporated into RGC must be primitive—indeed, it is more computationally efficient to utilize some nonprimitive constructions (i.e those used in Secs. 3.3 and 4.3). The implementation of the general algorithm with rigid motifs *rigid motif 1*, *rigid motif 2*,...*rigid motif n* on a configuration ρ is described through pseudocode in Algorithm 1.

Algorithm 1 : Rigid Graph Compression (RGC)

Generate Contact Graph $G(V, E)$ from ρ
while $\exists$ *rigid motif 1* OR *rigid motif 2* OR $\cdots$ *rigid motif n* $\in G$ **do**
    Identify *rigid motif 1* in G
    for each *rigid motif 1* in G **do**
        Compress(G,{nodes in *rigid motif 1*}, {edges in *rigid motif 1*})
    Identify *rigid motif 2* in G
    for each *rigid motif 2* in G **do**
        Compress(G,{nodes in *rigid motif 2*}, {edges in *rigid motif 2*})
    $\cdots$
    Identify *rigid motif n* in G
    for each *rigid motif n* in G **do**
        Compress(G,{nodes in *rigid motif n*}, {edges in *rigid motif n*})
    Identify *rigid motif 1*, *rigid motif 2*, $\cdots$ *rigid motif n* in G

procedure COMPRESS($G, \{nodes\}, \{edges\}$)
    Rewire all out-edges within $\{edges\}$ to a node $x \in nodes$, assign a weight/multi-edge of x to any out-edges that are rewired x times
    Delete all nodes in $\{nodes\}$ except x.

Finally, I note that this algorithm relies on an implicit assumption that two rigid components cannot share particles. That is, RGC can only identify a particle as being part of a single rigid component. This has been shown to be untrue in CF networks (Chubynsky and Thorpe, 2007), and it also untrue in 3D disordered fiber systems (see Fig. 4.3)—however, I conjecture that this false assumption is inconsequential to the detection of a spanning rigid component. Evidence for the conjecture is presented in the last paragraph of Sec. 4.4.2.

CHAPTER 3: RIGIDITY PERCOLATION IN DISORDERED SYSTEMS OF TWO-DIMENSIONAL FIBERS

> One secret which I alone possessed was the hope to which I had dedicated myself; and the moon gazed on my midnight labours, while, with unrelaxed and breathless eagerness, I pursued nature to her hiding-places. Who shall conceive the horrors of my secret toil as I dabbled among the unhallowed damps of the grave or tortured the living animal to animate the lifeless clay? My limbs now tremble, and my eyes swim with the remembrance; but then a resistless and almost frantic impulse urged me forward; I seemed to have lost all soul or sensation but for this one pursuit. ∼Victor Frankenstein

3.1 Overview

In this chapter, I consider the application of RGC (introduced in Sec. 2.3) to disordered systems of 2D rods. In particular, rods or fibers are treated as infinitesimally thin line segments which interact only at intersection points. In Sec. 3.2, I begin by using the rigidity matroid theory for interacting rigid components to prove three rigid motifs for 2D disordered rod systems and then specify how these motifs are incorporated into the algorithmic framework of Sec. 2.3.2. I perform a rigorous percolation analysis of these results of this implementation in Sec. 3.4, and finally discuss some related considerations in Sec. 3.5.

3.2 Primitive rigid motifs in two dimensions

I now use the language of rigid components developed in Sec. 2.3 to identify three primitive rigid motifs in disordered systems of 2D rods. In this treatment, rigid components are here defined as rods or sets of connected rods, but there is very little about the formalism requiring that the individual particles be rods, and the results of this treatment may with only slight modification be extended to ellipsoids, curvilinear filaments, and other 2D shapes, so long as the interactions between the particles are hinge-like. The three rigid motifs are presented below, simultaneously with their respective proofs, and then depicted in Fig. 3.1.

Theorem 3.1 (Motif 2D2)**.** *The composition of two rigid components R_1 and R_2 that intersect at two or more points $\boldsymbol{p}_1, \boldsymbol{p}_2, ...$ in two dimensions is rigid.*

Proof. As a first case, I assume both rigid components are inherently 2D (that is, $n_r^1, n_r^2 > 1$) and represent each aggregating rigid component using a coordinate labeling with three noncollinear

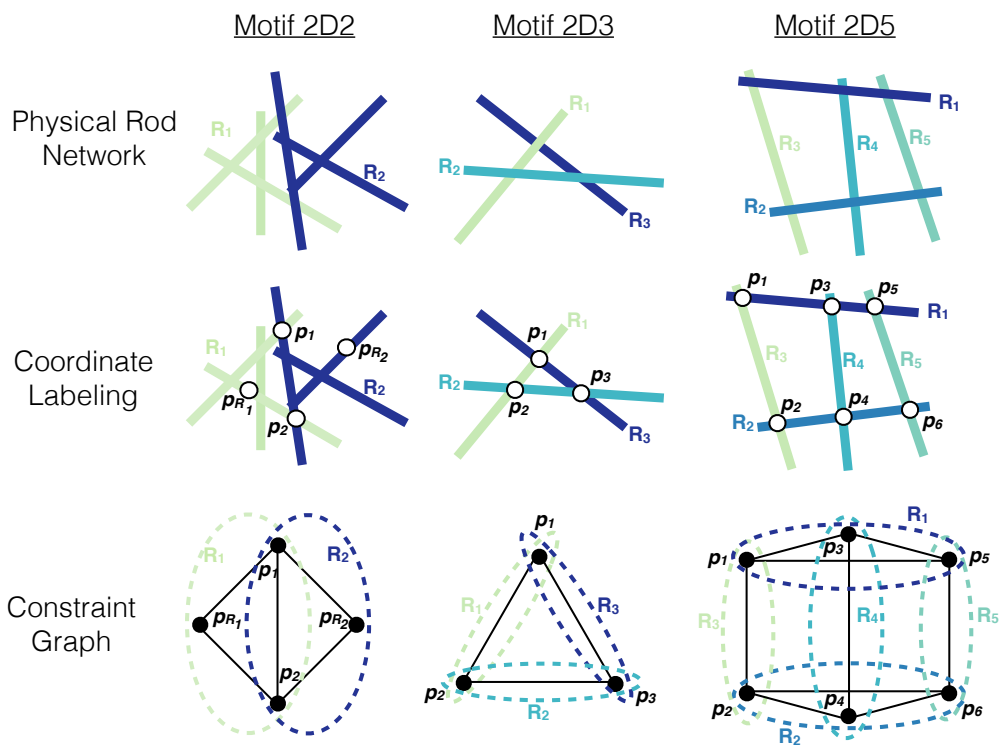

Figure 3.1: **Derivation of three primitive rigid motifs for 2D rod-hinge systems.** *Top Row*: Rigid components, which may be individual rods or sets of connected rods, distinguished here by color, intersect with three specific topologies as described in Sec. 3.2 to form larger-scale rigid components: (left column) two rigid components R_1 and R_2 interacting at a pair of points; (middle column) three rigid components R_1, R_2 and R_3 interacting pairwise; and (right column) five rigid components, $R_1, \ldots, R_5$ interacting in an identified pattern. For simplicity, I depict the rigid bodies in the middle and right columns as rods, but the proofs are general to include composite rigid components. *Middle Row*: Coordinate labelings are affixed to each rigid component: three noncollinear points are required to describe the motions of a 2D rigid component consisting of multiple rods, whereas individual rods are 1D and require only two points (although more may be used).For each motif, I identify a set of minimal coordinate labelings that include intersection points whenever possible (see text for clarification). *Bottom Row*: The coordinate labelings give rise to constraint graphs in which edges (black lines) indicate distances between adjacent points that are fixed. The dashed ellipses group the rigid components to which these points belong. By Theorems 3.1, 3.2, and 3.3, these constraint graphs and the motifs that generated them are rigid in two dimensions.

points. Importantly, I require for both coordinate labelings that two of these points, $\boldsymbol{p}_1$ and $\boldsymbol{p}_2$, be the intersection points between the rigid components so that the composite labeling is minimal (if there are more than two intersection points, I pick two arbitrarily). I denote the remaining two coordinate labeling points for R_1 and R_2 as $\boldsymbol{p}_{R_1}$ and $\boldsymbol{p}_{R_2}$, respectively, and choose them arbitrarily, subject to being noncollinear with $\boldsymbol{p}_1$ and $\boldsymbol{p}_2$, from the sets $R_1 \backslash R_2$ and $R_2 \backslash R_1$ (that is, in the restriction of

the space R_1 to points not in R_2, and vice versa). Thus, the coordinate labelings for R_1 and R_2 are the sets $\{\boldsymbol{p}_1, \boldsymbol{p}_2, \boldsymbol{p}_{R_1}\}$ and $\{\boldsymbol{p}_1, \boldsymbol{p}_2, \boldsymbol{p}_{R_2}\}$, respectively. (See, for example, the coordinate labeling in Fig. 3.1.)

I determine the rigidity of the composite system $R_1 * R_2$ through the rigidity matrix $\boldsymbol{X}_1 * \boldsymbol{X}_2$, obtained by combining the rigidity matrices of the individual rigid components:

$$\boldsymbol{X}_1 = \begin{bmatrix} \Delta\boldsymbol{p}_{1,2} & -\Delta\boldsymbol{p}_{1,2} & \mathbf{0} \\ \Delta\boldsymbol{p}_{1,R_1} & \mathbf{0} & -\Delta\boldsymbol{p}_{1,R_1} \\ \mathbf{0} & \Delta\boldsymbol{p}_{2,R_1} & -\Delta\boldsymbol{p}_{2,R_1} \end{bmatrix}, \tag{3.1}$$

$$\boldsymbol{X}_2 = \begin{bmatrix} \Delta\boldsymbol{p}_{1,2} & -\Delta\boldsymbol{p}_{1,2} & \mathbf{0} \\ \Delta\boldsymbol{p}_{1,R_2} & \mathbf{0} & -\Delta\boldsymbol{p}_{1,R_2} \\ \mathbf{0} & \Delta\boldsymbol{p}_{2,R_2} & -\Delta\boldsymbol{p}_{2,R_2} \end{bmatrix}. \tag{3.2}$$

Note that $\boldsymbol{X}_1$ and $\boldsymbol{X}_2$ are each of size 3×6 with $\Delta\boldsymbol{p}_{i,j} = \boldsymbol{p}_i - \boldsymbol{p}_j$ and each $\boldsymbol{p}_i \in \mathbb{R}^2$ denoting a length-2 row vector encoding the (x, y)-coordinates of a coordinate-labeling point. The 5×8 rigidity matrix of the composite system $R_1 * R_2$ is given by

$$\boldsymbol{X}_1 * \boldsymbol{X}_2 = \begin{bmatrix} \Delta\boldsymbol{p}_{1,2} & \Delta\boldsymbol{p}_{2,1} & \mathbf{0} & \mathbf{0} \\ \Delta\boldsymbol{p}_{1,R_1} & \mathbf{0} & \Delta\boldsymbol{p}_{R_1,1} & \mathbf{0} \\ \mathbf{0} & \Delta\boldsymbol{p}_{2,R_1} & \Delta\boldsymbol{p}_{R_1,2} & \mathbf{0} \\ \Delta\boldsymbol{p}_{1,R_2} & \mathbf{0} & \mathbf{0} & \Delta\boldsymbol{p}_{R_2,1} \\ \mathbf{0} & \Delta\boldsymbol{p}_{2,R_2} & \mathbf{0} & \Delta\boldsymbol{p}_{R_2,2} \end{bmatrix}, \tag{3.3}$$

where the first row derives from $R_1 \cap R_2$, the second and third rows from R_1, and the fourth and fifth rows from R_2. I group these elements into blocks such that the diagonal blocks are

$$\left\{ \begin{bmatrix} \Delta\boldsymbol{p}_{1,2} & -\Delta\boldsymbol{p}_{1,2} \end{bmatrix}, \begin{bmatrix} \Delta\boldsymbol{p}_{R_1,1} \\ \Delta\boldsymbol{p}_{R_1,2} \end{bmatrix}, \begin{bmatrix} \Delta\boldsymbol{p}_{R_2,1} \\ \Delta\boldsymbol{p}_{R_2,2} \end{bmatrix} \right\}, \tag{3.4}$$

each of which has full row rank (i.e., rank 1, 2, and 2, respectively), because $\boldsymbol{p}_{R_1}$ and $\boldsymbol{p}_{R_2}$ are each individually noncollinear with $\boldsymbol{p}_1$ and $\boldsymbol{p}_2$, by construction of the coordinate labelings. Because each diagonal block has full row rank, the block triangular matrix also has full row rank. Therefore,

$\text{rank}(\boldsymbol{X}_1 * \boldsymbol{X}_2) = 5$, $\dim(\text{null}(\boldsymbol{X}_1 * \boldsymbol{X}_2)) = 8 - 5 = 3$, and the composition is rigid—that is, the minimum number of degrees of freedom for a rigidity matrix of a two-dimensional system is 3.

In the case that $n_r^2 1 = 1$ (a rigid component that is a single rod), R_1 only requires two points to specify its rigid motions, and so I choose these to be $\boldsymbol{p}_1$ and $\boldsymbol{p}_2$, giving the 3×6 rigidity matrix

$$\boldsymbol{X}_1 * \boldsymbol{X}_2 = \begin{bmatrix} \Delta\boldsymbol{p}_{1,2} & -\Delta\boldsymbol{p}_{1,2} & \mathbf{0} \\ \Delta\boldsymbol{p}_{1,R_2} & \mathbf{0} & -\Delta\boldsymbol{p}_{1,R_2} \\ \mathbf{0} & \Delta\boldsymbol{p}_{2,R_2} & -\Delta\boldsymbol{p}_{2,R_2} \end{bmatrix}, \tag{3.5}$$

which trivially has full row rank and thus a right nullspace dimension of 3. Because individual distinct straight rods cannot intersect at more than one point, n_r^1 and n_r^2 cannot simultaneously both be one, so the two cases complete the proof. □

The necessity of two contacts in this latter scenario (where $n_r^1 = 1$) begs the following (rather obvious) lemma, which differentiates rigidity percolation from contact percolation:

Lemma 3.1. *Every rod in a rigid 2D rod-hinge system (with $n_r > 1$) must have at least two contacts.*

Proof. Suppose that a single rod R_1 has exactly one contact $\boldsymbol{p}_1$ with a rigid component R_2. Only two points are required to specify the rigid motions of R_1; I choose these to be $\boldsymbol{p}_1$ and $\boldsymbol{p}_{R_1}$. For R_2, I choose the coordinate labeling $\{\boldsymbol{p}_1, \boldsymbol{p}_{R_{2a}}, \boldsymbol{p}_{R_{2b}}\}$. The corresponding 4×8 rigidity matrix is

$$\boldsymbol{X}_1 * \boldsymbol{X}_2 = \begin{bmatrix} \Delta\boldsymbol{p}_{1,R_1} & -\Delta\boldsymbol{p}_{1,R_1} & \mathbf{0} & \mathbf{0} \\ \Delta\boldsymbol{p}_{1,R_{2a}} & \mathbf{0} & -\Delta\boldsymbol{p}_{1,R_{2a}} & \mathbf{0} \\ \Delta\boldsymbol{p}_{1,R_{2b}} & \mathbf{0} & \mathbf{0} & -\Delta\boldsymbol{p}_{1,R_{2b}} \\ \mathbf{0} & \mathbf{0} & \Delta\boldsymbol{p}_{R_{2a},R_{2b}} & -\Delta\boldsymbol{p}_{R_{2a},R_{2b}} \end{bmatrix}, \tag{3.6}$$

which trivially cannot have rank > 4 and thus its right nullspace dimension is at least 4, implying the composition is not rigid. □

Theorem 3.2 (Motif 2D3)**.** *The composition of three rigid components R_1, R_2, and R_3 intersecting pairwise in two dimensions at three or more points including $\boldsymbol{p}_1 \in (R_1 \cap R_3)$, $\boldsymbol{p}_2 \in (R_1 \cap R_2)$, $\boldsymbol{p}_3 \in (R_2 \cap R_3)$, is rigid.*

Proof. First, suppose $n_r^1 > 1$, $n_r^2 > 1$, and $n_r^3 > 1$. As in the proof of Thm. 3.1, I choose a minimal coordinate labeling for each rigid component, each of which includes two intersection points and one additional point, giving the sets of labelings: $\{\boldsymbol{p}_{R_1}, \boldsymbol{p}_1, \boldsymbol{p}_2\}$, $\{\boldsymbol{p}_{R_2}, \boldsymbol{p}_2, \boldsymbol{p}_3\}$, and $\{\boldsymbol{p}_{R_3}, \boldsymbol{p}_3, \boldsymbol{p}_1\}$. The composition's 9×12 rigidity matrix is larger in this scenario:

$$\boldsymbol{X}_1 * \boldsymbol{X}_2 * \boldsymbol{X}_3 = \begin{bmatrix} \Delta\boldsymbol{p}_{1,2} & -\Delta\boldsymbol{p}_{1,2} & \mathbf{0} & \mathbf{0} & \mathbf{0} & \mathbf{0} \\ \Delta\boldsymbol{p}_{1,R_1} & \mathbf{0} & \mathbf{0} & -\Delta\boldsymbol{p}_{1,R_1} & \mathbf{0} & \mathbf{0} \\ \mathbf{0} & \Delta\boldsymbol{p}_{2,R_1} & \mathbf{0} & -\Delta\boldsymbol{p}_{2,R_1} & \mathbf{0} & \mathbf{0} \\ \mathbf{0} & \Delta\boldsymbol{p}_{2,3} & -\Delta\boldsymbol{p}_{2,3} & \mathbf{0} & \mathbf{0} & \mathbf{0} \\ \mathbf{0} & \Delta\boldsymbol{p}_{2,R_2} & \mathbf{0} & \mathbf{0} & -\Delta\boldsymbol{p}_{2,R_2} & \mathbf{0} \\ \mathbf{0} & \mathbf{0} & \Delta\boldsymbol{p}_{3,R_2} & \mathbf{0} & -\Delta\boldsymbol{p}_{3,R_2} & \mathbf{0} \\ \Delta\boldsymbol{p}_{1,3} & \mathbf{0} & -\Delta\boldsymbol{p}_{1,3} & \mathbf{0} & \mathbf{0} & \mathbf{0} \\ \Delta\boldsymbol{p}_{1,R_3} & \mathbf{0} & \mathbf{0} & \mathbf{0} & \mathbf{0} & -\Delta\boldsymbol{p}_{1,R_3} \\ \mathbf{0} & \mathbf{0} & \Delta\boldsymbol{p}_{3,R_3} & \mathbf{0} & \mathbf{0} & -\Delta\boldsymbol{p}_{3,R_3} \end{bmatrix}. \quad (3.7)$$

The first three rows derive from R_1, the second three from R_2, and the third from R_3. Row permutation of $\boldsymbol{X}_1 * \boldsymbol{X}_2 * \boldsymbol{X}_3$ gives

$$\begin{bmatrix} \Delta\boldsymbol{p}_{1,2} & -\Delta\boldsymbol{p}_{1,2} & \mathbf{0} & \mathbf{0} & \mathbf{0} & \mathbf{0} \\ \Delta\boldsymbol{p}_{1,3} & \mathbf{0} & -\Delta\boldsymbol{p}_{1,3} & \mathbf{0} & \mathbf{0} & \mathbf{0} \\ \mathbf{0} & \Delta\boldsymbol{p}_{2,3} & -\Delta\boldsymbol{p}_{2,3} & \mathbf{0} & \mathbf{0} & \mathbf{0} \\ \Delta\boldsymbol{p}_{1,R_1} & \mathbf{0} & \mathbf{0} & -\Delta\boldsymbol{p}_{1,R_1} & \mathbf{0} & \mathbf{0} \\ \mathbf{0} & \Delta\boldsymbol{p}_{2,R_1} & \mathbf{0} & -\Delta\boldsymbol{p}_{2,R_1} & \mathbf{0} & \mathbf{0} \\ \mathbf{0} & \Delta\boldsymbol{p}_{2,R_2} & \mathbf{0} & \mathbf{0} & -\Delta\boldsymbol{p}_{2,R_2} & \mathbf{0} \\ \mathbf{0} & \mathbf{0} & \Delta\boldsymbol{p}_{3,R_2} & \mathbf{0} & -\Delta\boldsymbol{p}_{3,R_2} & \mathbf{0} \\ \Delta\boldsymbol{p}_{1,R_3} & \mathbf{0} & \mathbf{0} & \mathbf{0} & \mathbf{0} & -\Delta\boldsymbol{p}_{1,R_3} \\ \mathbf{0} & \mathbf{0} & \Delta\boldsymbol{p}_{3,R_3} & \mathbf{0} & \mathbf{0} & -\Delta\boldsymbol{p}_{3,R_3} \end{bmatrix}. \quad (3.8)$$

The same block diagonal argument from the proof in Thm 3.1 may be applied to show that this matrix has full row rank and thus right nullspace dimension 3. Explicitly, the diagonal blocks

$$\left\{ \begin{bmatrix} \Delta \boldsymbol{p}_{1,2} & -\Delta \boldsymbol{p}_{1,2} \end{bmatrix}, \begin{bmatrix} -\Delta \boldsymbol{p}_{1,3} \\ -\Delta \boldsymbol{p}_{2,3} \end{bmatrix}, \begin{bmatrix} -\Delta \boldsymbol{p}_{1,R_1} \\ -\Delta \boldsymbol{p}_{2,R_1} \end{bmatrix}, \begin{bmatrix} -\Delta \boldsymbol{p}_{2,R_2} \\ -\Delta \boldsymbol{p}_{3,R_2} \end{bmatrix}, \begin{bmatrix} -\Delta \boldsymbol{p}_{1,R_3} \\ -\Delta \boldsymbol{p}_{3,R_3} \end{bmatrix} \right\} \tag{3.9}$$

are each full row rank because the three points in a coordinate labeling are necessarily noncollinear. Therefore, the matrix is of full row rank (9) and the dimension of the right nullspace is $12 - 9 = 3$, which is again the minimum for all two-dimensional network rigidity matrices.

If one or more of the individual rigid components are single rods, then for each of these I may drop one of $\boldsymbol{p}_{R_1}$, $\boldsymbol{p}_{R_2}$, or $\boldsymbol{p}_{R_3}$, as well as the two corresponding constraints, giving no net change in the dimension of the right nullspace. Therefore, the composition is rigid. □

Theorem 3.3 (Motif 2D5)**.** *If five rigid components $\{R_1, \ldots, R_5\}$ intersect in two dimensions at six or more points such that $\boldsymbol{p}_1 \in (R_1 \cap R_3)$, $\boldsymbol{p}_2 \in (R_2 \cap R_3)$, $\boldsymbol{p}_3 \in (R_1 \cap R_4)$, $\boldsymbol{p}_4 \in (R_2 \cap R_4)$, $\boldsymbol{p}_5 \in (R_1 \cap R_5)$, $\boldsymbol{p}_6 \in (R_2 \cap R_5)$, then their composition is rigid—except in the degenerate case in which $\{\boldsymbol{p}_1, \boldsymbol{p}_3, \boldsymbol{p}_5\}$ and $\{\boldsymbol{p}_2, \boldsymbol{p}_4, \boldsymbol{p}_6\}$ are collinear (rod-sharing) sets, and the vectors $\Delta \boldsymbol{p}_{1,2}$, $\Delta \boldsymbol{p}_{3,4}$, $\Delta \boldsymbol{p}_{5,6}$ are mutually parallel (which occurs with probability 0).*

Proof. In the first case, I assume that the intersection points contained in R_1 ($\boldsymbol{p}_1, \boldsymbol{p}_3$, and $\boldsymbol{p}_5$) are noncollinear (they do not all lie along the same rod) as are those contained in R_2 ($\boldsymbol{p}_2, \boldsymbol{p}_4$, and $\boldsymbol{p}_6$). I also assume that $n_r^1 > 1, ..., n_r^5 > 1$. Then, I choose as coordinate labelings: $\{\boldsymbol{p}_1, \boldsymbol{p}_3\, \boldsymbol{p}_5\}$ for R_1, $\{\boldsymbol{p}_2, \boldsymbol{p}_4\, \boldsymbol{p}_6\}$ for R_2, $\{\boldsymbol{p}_1, \boldsymbol{p}_2, \boldsymbol{p}_{R_3}\}$ for R_3, $\{\boldsymbol{p}_3, \boldsymbol{p}_4, \boldsymbol{p}_{R_4}\}$ for R_4, and $\{\boldsymbol{p}_5, \boldsymbol{p}_6, \boldsymbol{p}_{R_5}\}$ for R_5. These labelings inform $5(3)$ constraints, given in the rigidity matrix:

$$\boldsymbol{X}_1 * ... * \boldsymbol{X}_5 =$$

$$\begin{bmatrix}
\Delta\boldsymbol{p}_{1,2} & -\Delta\boldsymbol{p}_{1,2} & \mathbf{0} & \mathbf{0} & \mathbf{0} & \mathbf{0} & \mathbf{0} & \mathbf{0} & \mathbf{0} \\
\Delta\boldsymbol{p}_{1,3} & \mathbf{0} & -\Delta\boldsymbol{p}_{1,3} & \mathbf{0} & \mathbf{0} & \mathbf{0} & \mathbf{0} & \mathbf{0} & \mathbf{0} \\
\mathbf{0} & \Delta\boldsymbol{p}_{2,4} & \mathbf{0} & -\Delta\boldsymbol{p}_{2,4} & \mathbf{0} & \mathbf{0} & \mathbf{0} & \mathbf{0} & \mathbf{0} \\
\mathbf{0} & \mathbf{0} & \Delta\boldsymbol{p}_{3,4} & -\Delta\boldsymbol{p}_{3,4} & \mathbf{0} & \mathbf{0} & \mathbf{0} & \mathbf{0} & \mathbf{0} \\
\Delta\boldsymbol{p}_{1,5} & \mathbf{0} & \mathbf{0} & \mathbf{0} & -\Delta\boldsymbol{p}_{1,5} & \mathbf{0} & \mathbf{0} & \mathbf{0} & \mathbf{0} \\
\mathbf{0} & \mathbf{0} & \Delta\boldsymbol{p}_{3,5} & \mathbf{0} & -\Delta\boldsymbol{p}_{3,5} & \mathbf{0} & \mathbf{0} & \mathbf{0} & \mathbf{0} \\
\mathbf{0} & \Delta\boldsymbol{p}_{2,6} & \mathbf{0} & \mathbf{0} & \mathbf{0} & -\Delta\boldsymbol{p}_{2,6} & \mathbf{0} & \mathbf{0} & \mathbf{0} \\
\mathbf{0} & \mathbf{0} & \mathbf{0} & \Delta\boldsymbol{p}_{4,6} & \mathbf{0} & -\Delta\boldsymbol{p}_{4,6} & \mathbf{0} & \mathbf{0} & \mathbf{0} \\
\mathbf{0} & \mathbf{0} & \mathbf{0} & \mathbf{0} & \Delta\boldsymbol{p}_{5,6} & -\Delta\boldsymbol{p}_{5,6} & \mathbf{0} & \mathbf{0} & \mathbf{0} \\
\Delta\boldsymbol{p}_{1,R_3} & \mathbf{0} & \mathbf{0} & \mathbf{0} & \mathbf{0} & \mathbf{0} & -\Delta\boldsymbol{p}_{1,R_3} & \mathbf{0} & \mathbf{0} \\
\mathbf{0} & \Delta\boldsymbol{p}_{2,R_3} & \mathbf{0} & \mathbf{0} & \mathbf{0} & \mathbf{0} & -\Delta\boldsymbol{p}_{2,R_3} & \mathbf{0} & \mathbf{0} \\
\mathbf{0} & \mathbf{0} & \Delta\boldsymbol{p}_{3,R_4} & \mathbf{0} & \mathbf{0} & \mathbf{0} & \mathbf{0} & -\Delta\boldsymbol{p}_{3,R_4} & \mathbf{0} \\
\mathbf{0} & \mathbf{0} & \mathbf{0} & \Delta\boldsymbol{p}_{4,R_4} & \mathbf{0} & \mathbf{0} & \mathbf{0} & -\Delta\boldsymbol{p}_{4,R_4} & \mathbf{0} \\
\mathbf{0} & \mathbf{0} & \mathbf{0} & \mathbf{0} & \Delta\boldsymbol{p}_{5,R_5} & 0 & \mathbf{0} & \mathbf{0} & -\Delta\boldsymbol{p}_{5,R_5} \\
\mathbf{0} & \mathbf{0} & \mathbf{0} & \mathbf{0} & \mathbf{0} & \Delta\boldsymbol{p}_{6,R_5} & \mathbf{0} & \mathbf{0} & -\Delta\boldsymbol{p}_{6,R_5}
\end{bmatrix}. \quad (3.10)$$

As in the proof of Thm 3.2, I have arranged the rows for convenience in rank computation—rows $2, 5, 6$ derive from R_1; $3, 7, 8$ from R_2; $1, 10, 11$ from R_3; $4, 12, 13$ from R_4; and $9, 14, 15$ from R_5. This matrix may be partitioned to have the diagonal blocks:

$$\boldsymbol{A} = \begin{bmatrix} \Delta\boldsymbol{p}_{1,2} & -\Delta\boldsymbol{p}_{1,2} \end{bmatrix},$$

$$\boldsymbol{B} = \begin{bmatrix}
-\Delta\boldsymbol{p}_{1,3} & \mathbf{0} & \mathbf{0} & \mathbf{0} \\
\mathbf{0} & -\Delta\boldsymbol{p}_{2,4} & \mathbf{0} & \mathbf{0} \\
\Delta\boldsymbol{p}_{3,4} & -\Delta\boldsymbol{p}_{3,4} & \mathbf{0} & \mathbf{0} \\
\mathbf{0} & \mathbf{0} & -\Delta\boldsymbol{p}_{1,5} & \mathbf{0} \\
\Delta\boldsymbol{p}_{3,5} & \mathbf{0} & -\Delta\boldsymbol{p}_{3,5} & \mathbf{0} \\
\mathbf{0} & \mathbf{0} & \mathbf{0} & -\Delta\boldsymbol{p}_{2,6} \\
\mathbf{0} & \Delta\boldsymbol{p}_{4,6} & \mathbf{0} & -\Delta\boldsymbol{p}_{4,6} \\
\mathbf{0} & \mathbf{0} & \Delta\boldsymbol{p}_{5,6} & -\Delta\boldsymbol{p}_{5,6}
\end{bmatrix}, \quad \boldsymbol{C} = \begin{bmatrix}
-\Delta\boldsymbol{p}_{1,R_3} & \mathbf{0} & \mathbf{0} \\
-\Delta\boldsymbol{p}_{2,R_3} & \mathbf{0} & \mathbf{0} \\
\mathbf{0} & -\Delta\boldsymbol{p}_{3,R_4} & \mathbf{0} \\
\mathbf{0} & -\Delta\boldsymbol{p}_{4,R_4} & \mathbf{0} \\
\mathbf{0} & \mathbf{0} & -\Delta\boldsymbol{p}_{5,R_5} \\
\mathbf{0} & \mathbf{0} & -\Delta\boldsymbol{p}_{6,R_5}
\end{bmatrix}.$$

Matrix $\boldsymbol{A}$ trivially has full row rank and matrix $\boldsymbol{C}$ has full rank due to the points in each coordinate labeling being noncollinear. I use a series of elementary row operations to eliminate the last six

entries in row $B_{6,\bullet}$, and then place $B_{6,\bullet}$ between $B_{1,\bullet}$ and $B_{2,\bullet}$, giving that $\boldsymbol{B}$ is rank equivalent to:

$$\boldsymbol{B'} = \begin{bmatrix} -\Delta\boldsymbol{p}_{1,3} & \mathbf{0} & \mathbf{0} & \mathbf{0} \\ c_1\Delta\boldsymbol{p}_{3,4} + c_2\Delta\boldsymbol{p}_{3,5} & \mathbf{0} & \mathbf{0} & \mathbf{0} \\ \mathbf{0} & -\Delta\boldsymbol{p}_{2,4} & \mathbf{0} & \mathbf{0} \\ \Delta\boldsymbol{p}_{3,4} & -\Delta\boldsymbol{p}_{3,4} & \mathbf{0} & \mathbf{0} \\ \mathbf{0} & \mathbf{0} & -\Delta\boldsymbol{p}_{1,5} & \mathbf{0} \\ \Delta\boldsymbol{p}_{3,5} & \mathbf{0} & -\Delta\boldsymbol{p}_{3,5} & \mathbf{0} \\ \mathbf{0} & \Delta\boldsymbol{p}_{4,6} & \mathbf{0} & -\Delta\boldsymbol{p}_{4,6} \\ \mathbf{0} & \mathbf{0} & \Delta\boldsymbol{p}_{5,6} & -\Delta\boldsymbol{p}_{5,6} \end{bmatrix},$$

where $c_1 = \frac{Det[\Delta\boldsymbol{p}_{4,6},\Delta\boldsymbol{p}_{2,4}]\cdot Det[\Delta\boldsymbol{p}_{5,6},\Delta\boldsymbol{p}_{2,6}]}{Det[\Delta\boldsymbol{p}_{3,4},\Delta\boldsymbol{p}_{2,4}]\cdot Det[\Delta\boldsymbol{p}_{5,6},\Delta\boldsymbol{p}_{4,6}]}$ and $c_2 = \frac{Det[\Delta\boldsymbol{p}_{4,6},\Delta\boldsymbol{p}_{2,6}]\cdot Det[\Delta\boldsymbol{p}_{5,6},\Delta\boldsymbol{p}_{1,5}]}{Det[\Delta\boldsymbol{p}_{3,5},\Delta\boldsymbol{p}_{1,5}]\cdot Det[\Delta\boldsymbol{p}_{4,6},\Delta\boldsymbol{p}_{5,6}]}$ ($Det[\boldsymbol{i},\boldsymbol{j}]$ indicates the determinant of $\begin{bmatrix} \boldsymbol{i} \\ \boldsymbol{j} \end{bmatrix}$). The upper 2×2 block of this latter matrix has determinant $c_1 Det[\Delta\boldsymbol{p}_{3,4}, \Delta\boldsymbol{p}_{1,3}] + c_2 Det[\Delta\boldsymbol{p}_{3,5}, \Delta\boldsymbol{p}_{1,3}]$. Because I assume under generic conditions that none of these vectors are parallel, each of the terms in this determinant are nonzero. Then, upon appropriate substitution and use of the geometric equality $Det([\boldsymbol{i}\ \ \boldsymbol{j}]^T) = |i||j|\sin\theta$ (where $|\cdot|$ refers to the 2-norm and θ is the angle formed between $\boldsymbol{i}$ and $\boldsymbol{j}$), I find that this determinant is zero if and only if:

$$\frac{|\Delta\boldsymbol{p}_{1,5}|\sin\theta_1}{|\Delta\boldsymbol{p}_{2,6}|\sin\theta_2} = \frac{|\Delta\boldsymbol{p}_{1,3}|\sin\theta_3}{|\Delta\boldsymbol{p}_{2,4}|\sin\theta_4}, \tag{3.11}$$

where θ_1 refers to the angle between $\Delta\boldsymbol{p}_{1,5}$ and $\Delta\boldsymbol{p}_{5,6}$; θ_2 refers to the angle between $\Delta\boldsymbol{p}_{2,6}$ and $\Delta\boldsymbol{p}_{5,6}$; θ_3 refers to the angle between $\Delta\boldsymbol{p}_{1,3}$ and $\Delta\boldsymbol{p}_{3,4}$; and θ_4 refers to the angle between $\Delta\boldsymbol{p}_{2,4}$ and $\Delta\boldsymbol{p}_{3,4}$ (see Fig. 3.2).

Under generic conditions in which none of the vectors in $\boldsymbol{X}_1 * ... * \boldsymbol{X}_5$ are parallel, the quantities on the left hand side of Eq. 3.11 do not fully determine those on the right (see Fig. 3.2). Therefore, Eq. 3.11 is satisfied with probability 0 and the upper left 2×2 block in $\boldsymbol{B'}$ has full rank. Additionally, as each pair of vectors is nonparallel under generic conditions, each 2×2 block along the diagonal of $\boldsymbol{B'}$ has full rank. Therefore $\boldsymbol{B}$ itself has full rank, and the 15×18 matrix $\boldsymbol{X}_1 * ... * \boldsymbol{X}_5$ has full row rank and right nullspace dimension 3. If any one or more components R_3, R_4, and/or R_5 are

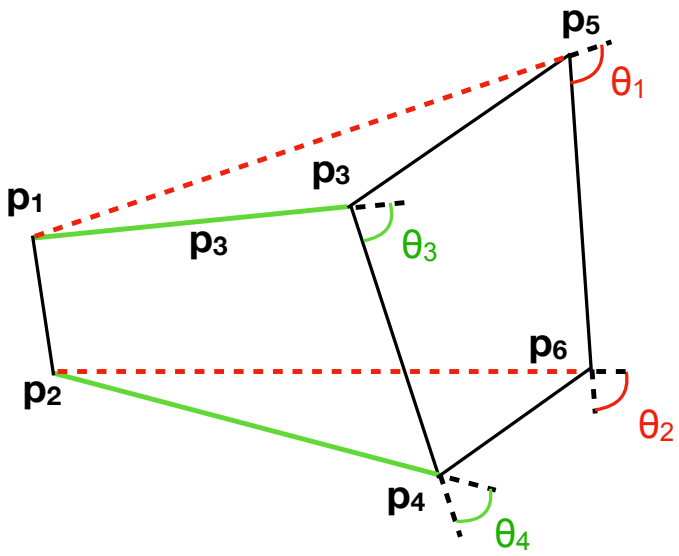

Figure 3.2: **Visualization of quantities of interest in Eqs. 3.11.** Given that $\boldsymbol{p}_1, \boldsymbol{p}_3, \boldsymbol{p}_5$ and $\boldsymbol{p}_2, \boldsymbol{p}_4, \boldsymbol{p}_6$ form noncollinear sets, the variables $|\Delta\boldsymbol{p}_{1,5}|$, $|\Delta\boldsymbol{p}_{2,6}|$, θ_1, and θ_2 (red) do not fully determine $|\Delta\boldsymbol{p}_{1,3}|$, $|\Delta\boldsymbol{p}_{2,4}|$, θ_3, and θ_4 (green).

singleton rods, I omit the corresponding point(s) $\boldsymbol{p}_{R_i}$ and the corresponding pair(s) of constraint rows, giving no net change in the resultant degrees of freedom calculation.

The careful reader will note that if points $\boldsymbol{p}_1$, $\boldsymbol{p}_3$, and $\boldsymbol{p}_5$ lie along the same rod (as would be necessary if R_1 is a singleton rod), then the vectors $\Delta\boldsymbol{p}_{1,5}$ and $\Delta\boldsymbol{p}_{3,5}$ are parallel—in this case, the matrix $\boldsymbol{B}$ above would not have full row rank. In the first case, I excluded this possibility—now, I turn to the case in which the sets $\{\boldsymbol{p}_1, \boldsymbol{p}_3, \boldsymbol{p}_5\}$ and $\{\boldsymbol{p}_2, \boldsymbol{p}_4, \boldsymbol{p}_6\}$ are both collinear sets (i.e. each set of three intersections shares a single rod). This collinearity condition makes my task more challenging, as each of the three *collinear* points in $\{\boldsymbol{p}_1, \boldsymbol{p}_3, \boldsymbol{p}_5\}$ ($\{\boldsymbol{p}_2, \boldsymbol{p}_4, \boldsymbol{p}_6\}$) lie in R_1 (R_2), yet I must choose three *noncollinear* points in each coordinate labeling. First, I choose $\boldsymbol{p}_3$ to lie between $\boldsymbol{p}_1$ and $\boldsymbol{p}_5$, and $\boldsymbol{p}_4$ to lie between $\boldsymbol{p}_2$ and $\boldsymbol{p}_6$ (this is arbitrary—as R_3, R_4, and R_5 have the same connectivities). Then, I choose as coordinate labelings $\{\boldsymbol{p}_1, \boldsymbol{p}_5\, \boldsymbol{p}_{R_1}\}$ for R_1, and $\{\boldsymbol{p}_2, \boldsymbol{p}_6\, \boldsymbol{p}_{R_2}\}$ for R_2, where $\boldsymbol{p}_{R_1}$ and $\boldsymbol{p}_{R_2}$ are chosen to be noncollinear with $\boldsymbol{p}_1$ and $\boldsymbol{p}_5$ ($\boldsymbol{p}_2$ and $\boldsymbol{p}_6$). I choose coordinate labelings R_3, R_4, and R_5 as before.

This choice of labelings give $3(5)$ constraints as above, but I have included 11 as opposed to 9 points in these constraints, and so even if these constraints are linearly independent, the resulting degrees of freedom calculation is $2(11) - 15 = 7$. However, as alluded to in Sec. 2.2.4, these former constraints of the form Eq. 2.4 do not account for the fact that all points along a single rod are rigid

with respect to another. Given that $\boldsymbol{p}_3$ lies between $\boldsymbol{p}_1$ and $\boldsymbol{p}_5$, I account for this using the geometric equality:

$$\boldsymbol{p}_3 = s\boldsymbol{p}_5 + (1-s)\boldsymbol{p}_1, \tag{3.12}$$

where $s = \frac{|\Delta \boldsymbol{p}_{1,3}|}{|\Delta \boldsymbol{p}_{1,5}|} \in (0,1)$. We can think of this equation parametrically, with s giving the fractional distance along the line segment from $\boldsymbol{p}_1$ to $\boldsymbol{p}_5$ at which $\boldsymbol{p}_3$ is located. Because this fractional distance is fixed (i.e. $\boldsymbol{p}_3$ cannot shift along its containing rod), I also have the condition that $\frac{ds}{dt} = 0$, and therefore:

$$\boldsymbol{u}_3 = s\boldsymbol{u}_5 + (1-s)\boldsymbol{u}_1 \tag{3.13}$$

I can similarly derive that $\boldsymbol{u}_4 = s'\boldsymbol{u}_6 + (1-s')\boldsymbol{u}_2$, where $s' = \frac{|\Delta \boldsymbol{p}_{2,4}|}{|\Delta \boldsymbol{p}_{2,6}|} \in (0,1)$. Each equation introduces two *augmented* constraints into the augmented 19×22 composite rigidity matrix. Using similar steps, I can show that this latter matrix has full row rank unless $\Delta \boldsymbol{p}_{1,2}$, $\Delta \boldsymbol{p}_{3,4}$, and $\Delta \boldsymbol{p}_{5,6}$ are mutually parallel (which I excluded by hypothesis). The case in which one but not both of the sets $\{\boldsymbol{p}_1, \boldsymbol{p}_3, \boldsymbol{p}_5\}$ and $\{\boldsymbol{p}_2, \boldsymbol{p}_4, \boldsymbol{p}_6\}$ are collinear follows similarly.

□

3.3 Algorithmic details of Rigid Graph Compression applied to 2D disordered fiber systems (*2D-RGC-5*)

Algorithms *2D-RGC-3* and *2D-RGC-5* are implementations of Algorithm 1. Essentially, *2D-RGC-5* incorporates the three rigid motifs of the previous section, while *2D-RGC-3* only incorporates the 2- and 3-body rigid motifs. Rather than identifying instances of Motif 2D3 directly, I make use of an available fast algorithm (Palla et al., 2005; Hagberg et al., 2008) for identifying *k-clique communities*, which are sets of k-cliques (complete subgraphs on k nodes), joined pairwise at $k-1$ points. In particular, any 3-clique community (see Fig 3.3) is necessarily a composite rigid motif in 2D, by repeated application of Motifs 2D2 and 2D3. Furthermore, every instance of Motif 2D3 is a member of a 3-clique communities (at that spatial scale), although the same cannot be said for Motif 2D2. I describe *2D-RGC-5* explicitly via psuedocode in Algorithm 2, and then illustrate its implementation on a configuration in Fig. 3.3.

I conjecture that while the order of the three motif compression steps of Algorithm 2 could be chosen in $3! = 6$ possible ways, this order does not affect the resulting analysis. In the case that rigid

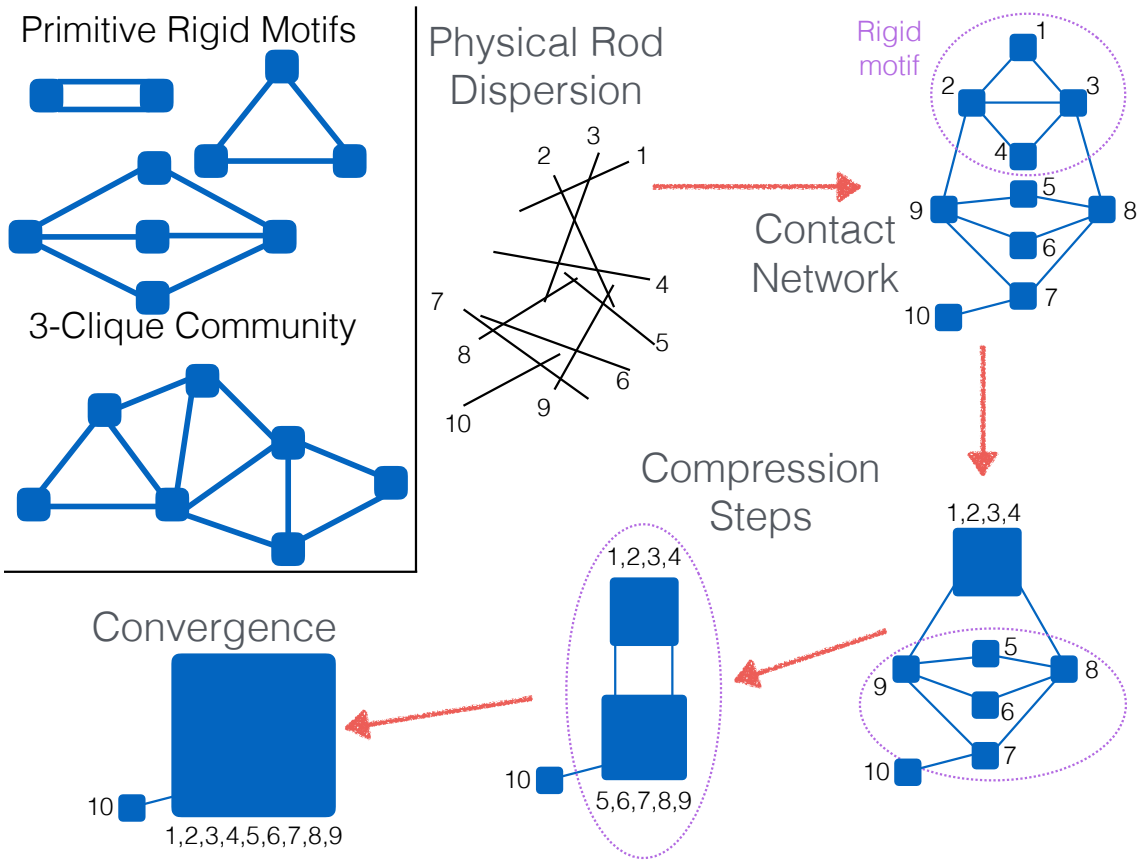

Figure 3.3: **Graph compression of rod-hinge systems using rigid motifs** Using a 10-component rod-hinge system as an example, I describe *2D-RGC-5* (Algorithm 2), which iteratively compresses 2- and 5-component primitive rigid motifs, as well as 3-clique communities (see top left inset for contact network representations of these motifs). In the first step, the physical rod dispersion is transformed into a rod contact network. This contact network contains both a 3-clique community (nodes 1-4) and a 5-component motif (5-9). In two steps, each of these motifs are compressed into a single compound node. These two composite nodes are connect by two edges, which is the 2-component primitive rigid motif and is then compressed in the final step, giving one compound node representing rods 1-9 connected to another node representing rod 10. Stopping in the absence of any other primitive rigid motifs, RGC thus identifies two rigid components within the candidate rod-hinge system.

Algorithm 2 : Rigid Graph Compression (2D-RGC-5)

Generate Contact Graph $G(V, E)$ from $\{R\}$
while $\exists$ 3-clique communities OR 2-component motifs OR 5-component motifs $\in G$ **do**
    Identify 3-clique communities in G
    for each 3-clique community in G **do**
        Compress(G,{nodes in 3-clique community}, {edges in 3-clique community})
    Identify 2-component motifs in G
    for each 2-component motif in G **do**
        Compress(G,{nodes in 2-component motif}, {edges in 2-component motif})
    Identify 5-component motifs in G
    for each 5-component motif in G **do**
        Compress(G,{nodes in 5-component motif}, {edges in 5-component motif})
    Identify 3-clique communities, 2-component motifs, 5-component motifs in G

procedure COMPRESS($G, \{nodes\}, \{edges\}$)
    Rewire all out-edges within $\{edges\}$ to a node $x \in nodes$, assign a weight of two to any out-edges that are rewired ≥ 2 times
    Delete all nodes in $\{nodes\}$ except x.

motifs do not intersect, any motif compression order trivially gives the same result; but when two or more rigid motifs intersect (their contact network representations share at least one node), this conclusion is slightly more nuanced. Below, I argue that any motif compression order will yield the same results when Algorithm 2 is subjected to intersecting motifs. In general, iterative graph compression of two intersecting motifs might achieve different final states if different orderings of motif compression are used. However, in testing the motifs used here on small systems (described below), I do not find any cases where the output of *2D-RGC-5* or *2D-RGC-3* is affected by the order of compression of 2-, 3-, and 5-component motifs (as well as 3-clique communities).

First, I consider simple cases in which the different motifs share at least one node in common. For example, suppose a 2-component and a 3-component motif intersect. There are two ways in which this may occur: the former may be fully contained in the latter, or the motifs may simply share a node (see the top two graphs in Fig. 3.4). In the former case, application of Motif 2D2 yields another 2D2 motif (which is then compressed), while application of Motif 2D3 compresses the graph in a single step. In the latter case, application of Motif 2D3 leads to Motif 2D2, and vice versa. In Fig. 3.4, I enumerate the possible (nonisomorphic) ways in which any of the 2-, 3-, and 5-component

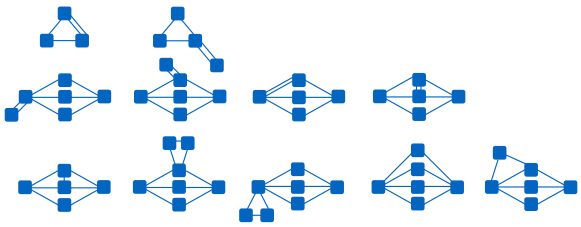

Figure 3.4: **Nonisomorphic intersections of 2-, 3-, and 5-component motifs.** Top Row: Simplest nonisomorphic cases involving intersections of (that is, containing both) the 2- and 3-body primitive rigid motifs. Middle Row: Simplest intersections of 2- and 5-component motifs. Bottom Row: Simplest intersections of 3- and 5-component motifs. Each of these networks compress to a single rigid component regardless of the order in which the 2D primitive rigid motifs are compressed.

motifs may intersect pairwise. It is easy to check that any order of motif compression will yield a single rigid component in these cases.

I have additionally employed the graphlet-based exhaustive search method used in Sec. 3.5 to verify that each ordering of graph compression gives the same output for all rod contact networks generated with up to $n_r = 8$ rods. Generally, I thus expect that graph compression ordering is very likely inconsequential in two dimensions (the three-dimensional case is similar, and is discussed in Sec. 4.2.1).

3.4 Numerical experiments

3.4 Experimental design

In order to characterize rigidity percolation in 2D disordered fiber systems, I recreate the experimental system of (Latva-Kokko and Mäkinen, 2001): unit-length rods are placed with uniformly random position and orientation in a rectangular domain. This domain is divided into an $L \times L$ square region, with $1 \times L$ 'buffer regions' on the left and right sides along one dimension, to eliminate bias in the rod density near these boundaries. I effectively place a large, length L (infinitesimally thin) rod along the boundary between each buffer region with the interior square domain, and define rigidity percolation by the presence of a spanning rigid component containing both of these boundaries (see Fig. 1.1). Periodic boundary conditions are used in the other dimension.

For this analysis, I generate configurations wherein rods are dispersed in domains of size $L = 40, 60, 80, 100, 120, 140$, and 160. In each domain size, 15 different rod densities $q = r/(q_c L^2)$ are considered, where $q_c \doteq 5.71$ is the contact-percolation threshold for 2D disordered fiber systems systems (Pike and Seager, 1974)—these densities are chosen so as to be centered about the rigidity

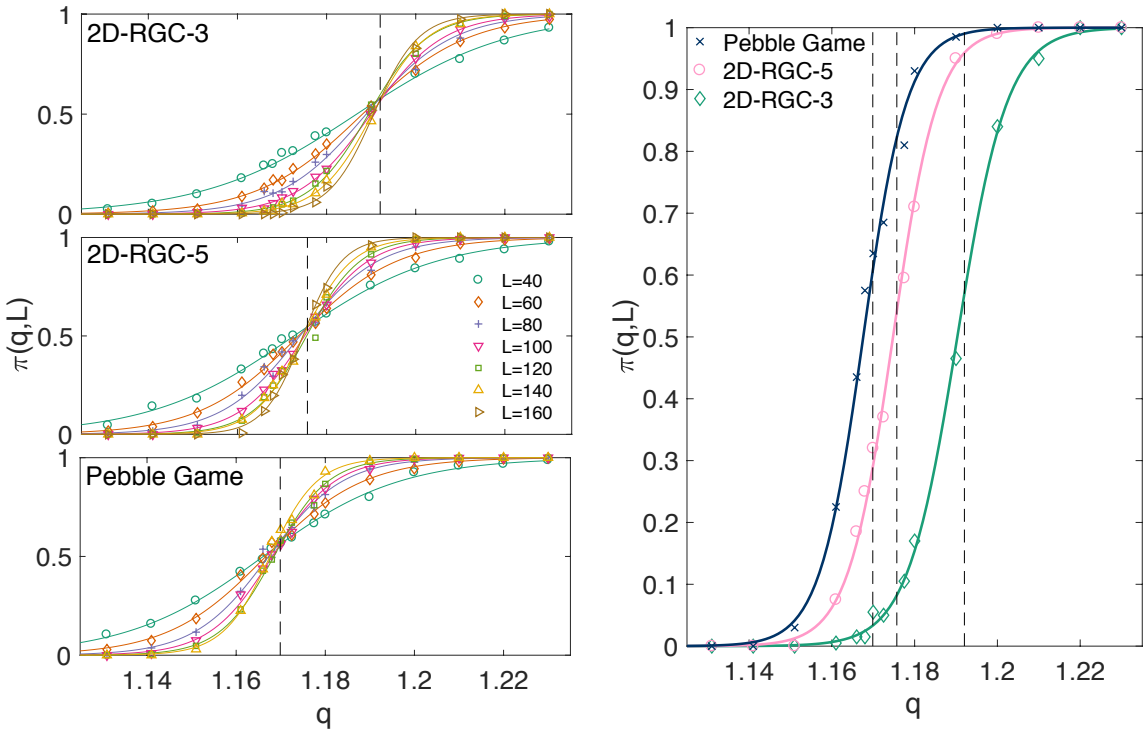

Figure 3.5: **Comparison of 2D-RGC-3, 2D-RGC-5, and pebble-game algorithms for 2D rigidity percolation.** *Left*: For all three rigidity-detection algorithms, there is a phase transition in $\pi(q, L)$ that becomes sharper with increasing L—an extrapolation algorithm is used to estimate rigidity percolation thresholds (vertical dashed lines) from these individual curves. The transitions identified using the RGC algorithms approximate that of the pebble game, with that of the *2D-RGC-5* being the closer approximation. Incorporation of yet more rigid motifs would further increase the accuracy of this approximation. *Right*: Rigidity percolation transitions for each of the three algorithms are displayed for a large domain size, $L = 140$.

percolation estimate found in (Latva-Kokko and Mäkinen, 2001). In each configuration, I check for the presence of a spanning rigid component using each of three algorithms: *2D-RGC-3* and *2D-RGC-5* (described in previous subsection); and the pebble game (Sec. 2.2.2). Between 150 and 1100 simulation trials are implemented at each (q, L) pair to approximate the probability of rigidity percolation $\pi(q, L)$ across this parameter space (see Fig. 3.5).

3.4 Results

In order to accurately estimate the rigidity percolation threshold $q_{\min}$ and correlation length exponent ν (associated with the divergence of the correlation length about $q_{\min}$) corresponding to each algorithm, I first assume a data collapse in accordance with classical percolation theory

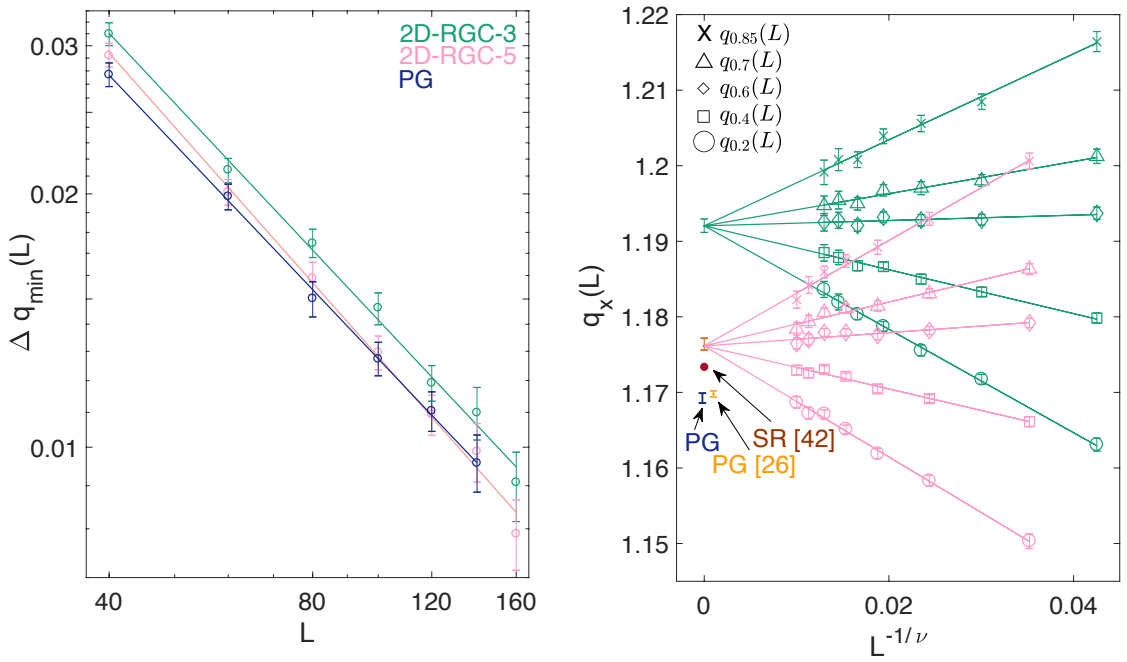

Figure 3.6: **Estimation of correlation length exponent and rigidity percolation threshold for RGC and pebble game algorithms.** *Left*: Using each rigidity characterization algorithm, I use the relation $\Delta q_{\min}(L) \sim L^{-1/\nu}$ to estimate ν. *Right*: An extrapolation scheme is used to estimate $q_{\min}$ using each of the three rigidity detection algorithms. For comparison, I display the rigidity percolation threshold found in (Latva-Kokko and Mäkinen, 2001) using the pebble game (PG [26]), in my own pebble game calculations (PG), and in (Wilhelm and Frey, 2003) using spring relaxation (SR).

(Latva-Kokko and Mäkinen, 2001; Stauffer and Aharony, 1992):

$$\pi(q - q_{\min}, L) = \Pi([q - q_{\min}]L^{1/\nu}), \tag{3.14}$$

from which I find $\frac{d\pi}{dq} = L^{1/\nu}\phi'([q - q_{\min}]L^{1/\nu})$ for $q \to q_{\min}$. As in Latva-Kokko and Mäkinen (2001), I invert the scaling of $d\pi/dq$ with $L^{1/\nu}$, finding that

$$\Delta q_{\min}(L) := \langle\sqrt{(q_{est} - q_{av})^2}\rangle \tag{3.15}$$

scales as $L^{-1/\nu}$, where q_{est} is the density at which a spanning cluster first appears for a particular set of simulations at a given L and q_{av} is the average of these simulations (angular brackets denote averages). For each algorithm and domain size L, I estimate $\Delta q_{\min}(L)$, the standard deviation of the rigidity percolation threshold (this use of $\mathbf{\Delta}$ is not to be used with the prior one, which indicated

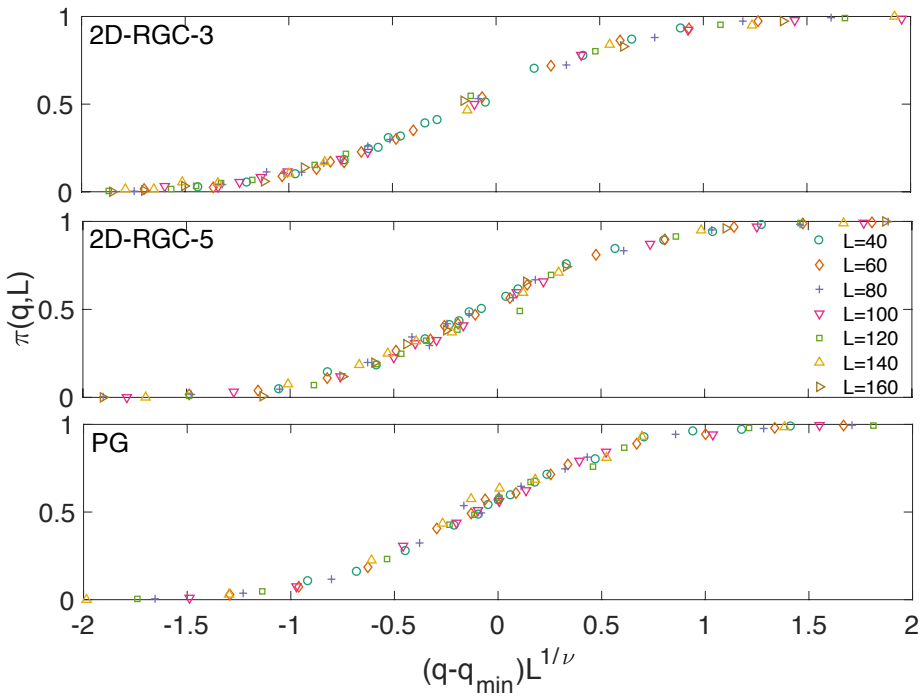

Figure 3.7: **Demonstration of data collapse.** Using the identified values of ν and $q_{\min}$ for each rigidity detection algorithm, I find the data collapse assumption (according to Eq. 3.14) to be quite sound.

a vector difference), by fitting a cumulative logistic distribution $F(q;\mu,\sigma) = 1/(1+e^{-\frac{q-\mu}{\sigma}})$ to the set of values $\pi(q,L)$, and then setting $\Delta q_{\min}(L)$ equal to the standard deviation $\sigma\pi/\sqrt{3}$ of this distribution. I fit $\log \Delta q_{\min}(L)$ versus $\log L$ (left panel of Fig. 3.6) via least squares minimization to estimate ν, using a simple case resampling method to simultaneously determine confidence intervals for every $\Delta q_{\min}(L)$ estimation. From each set of $\Delta q_{\min}(L)$ samples, I estimate a fit for ν and use the collection of these fits to calculate the corresponding confidence intervals. I thereby obtain $\nu \doteq 1.1682, 1.1025, 1.1812$ for *2D-RGC-3*, *2D-RGC-5*, and the pebble game, respectively, with corresponding 95% confidence intervals of $[1.1137, 1.2546]$, $[1.0474, 1.1670]$, and $[1.1036, 1.2340]$. While the correlation length exponent estimated by *2D-RGC-5* is comparatively low, I note the confidence intervals from the three methods overlap.

Having estimated ν, I seek to now estimate $q_{\min}$. To derive a scaling law, I expand $\pi(q,L)$ around $q = q_{\min}$ in Eq. 3.14 and invert, deriving the condition:

$$q_x(L) = (\text{constant}) \cdot L^{-1/\nu} + q_{\min}\,, \tag{3.16}$$

where $q_x(L)$ is a probability distribution such that $\pi(q_x(L), L) = x$ for some $x \in [0, 1]$ (Latva-Kokko and Mäkinen, 2001; Stauffer and Aharony, 1992). I use this equation to extrapolate the $q_x(L)$ values as $L \to \infty$ to predict $q_{\min}$ for each algorithm as follows. First, I find $q_x(L)$ via inverse prediction from the corresponding cumulative distribution $F(q; \mu, s)$ for $x = 0.2, 0.4, 0.6, 0.7, 0.85$. Then, I fit each set of $\log q_x(L)$ values against $-\nu^{-1} \log L$, with the constraint that each of these fits must coincide at the intercept with the q axis (see right panel of Fig. 3.6). I estimate the intercepts to be $q_{\min} \doteq 1.1920, 1.1757$, and 1.1692 for *2D-RGC-3*, *2D-RGC-5*, and the pebble game, respectively, with corresponding 95% confidence intervals of [1.1912, 1.1929], [1.1756, 1.1767], and [1.1686, 1.1698]. Taking the pebble game estimate to be the true threshold, I find the relative errors for the *2D-RGC-3* and *2D-RGC-5* estimates to be 1.9% and 0.6%, respectively. Finally, having identified $q_{\min}$ and ν for each rigidity-detection algorithm, I confirm that the rescaling data collapse $\pi(q, L) = \Pi([q - q_{\min}]L^{1/\nu})$ assumption is quite accurate (see Fig. 3.7).

3.5 Related directions

To better understand the discrepancies between the rigidity percolation transition as predicted by RGC and the pebble game, I apply each algorithm to graphlets—small connected nonisomorphic graphs—in the rod contact network representation. I limit this search to graphlets with minimal degree two (on account of Lemma 3.1). I confirm that *2D-RGC-3* perfectly characterizes rigidity for all graphlets of $n_r \leq 4$ components, but of course fails to detect that the $n_r = 5$ Motif 2D5 is rigid, and thus misses a number of $n_r > 5$ cases as well (the yellow motifs in Fig. 3.8). By accounting for the rigidity of Motif 2D5, *2D-RGC-5* is accurate for all graphlets with $n_r \leq 6$, but misses three $n_r = 7$ cases (purple motifs in Fig. 3.8). By incorporating these primitive rigid motifs with 7 components, one might develop a *2D-RGC-7* algorithm and estimate $q_{\min}$ with even higher accuracy relative to the two RGC versions used in this study.

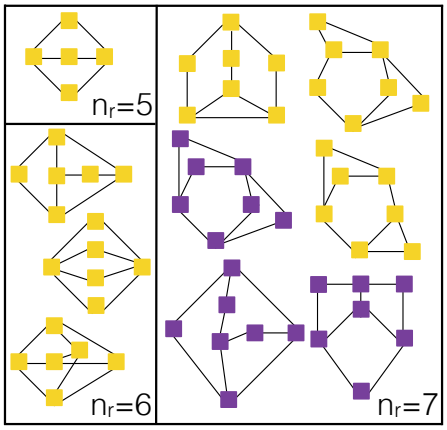

Figure 3.8: **Rigid motifs not identified by 2D-RGC-3 and/or 2D-RGC-5.** Exhaustive search of rod contact networks containing up to seven rods reveals seven rigid motifs incorrectly identified as floppy by 2D-RGC-3 only (yellow), and three other rigid motifs incorrectly identified as floppy by both 2D-RGC-3 and 2D-RGC-5 (purple). These latter motifs—which are classified as rigid via the pebble game—could potentially be incorporated into a 2D-RGC-7 algorithm.

CHAPTER 4: RIGIDITY PERCOLATION IN DISORDERED SYSTEMS OF THREE-DIMENSIONAL FIBERS

> Of my creation and creator I was absolutely ignorant, but I knew that I possessed no money, no friends, no kind of property. I was, besides, endued with a figure hideously deformed and loathsome; I was not even of the same nature as man. I was more agile than they and could subsist upon coarser diet; I bore the extremes of heat and cold with less injury to my frame; my stature far exceeded theirs. When I looked around I saw and heard of none like me. Was I, then, a monster, a blot upon the earth from which all men fled and whom all men disowned? $\sim$ 'the monster'

4.1 Overview

Unlike in the two-dimensional case, rigidity percolation in systems of disordered 3D fibers remains an open problem. While this problem is challenging, and this dissertation comes short of a complete rigidity analysis of such systems, the methodology used in this section provides a clear path towards a solution. In Sec. 4.2, I develop the rigidity motifs in three dimensions according to the methodology discussed in Ch. 2. In Sec. 4.3, I organize these motifs into the rigidity decomposition algorithm *3D-RGC*, which I implement on systems of randomly dispersed fibers in Sec. 4.4. Finally, in Sec. 4.5, I discuss methods for showing that this algorithm achieves sufficient accuracy and conclude this chapter.

4.2 Primitive 3D rigid motifs

4.2 Differences between rigidity analysis in 2 and 3 dimensions

In two dimensions, 'fibers' essentially amount to line segments (one could lower the aspect ratio in a different study, in which case fibers would be considered as thin rectangles), which interact at intersection points. In three dimensions, line segments (with infinite aspect ratio) intersect with probability zero. Fibers must have nonzero radii in order for intersections to occur. Therefore, in this study, I consider pairs of fibers to be interacting if their nearest points fall within some distance γ_r of one another.

Another difference between 2D and 3D fiber systems arises from the increased number of degrees of freedom in three dimensional rigid bodies. In the plane, line segments ($n_r = 1$) and other nonlinear rigid bodies ($n_r > 1$) each have $\chi(2) = 3$ degrees of freedom (two from translation and

one from rotation)—allowing for the equivalency of scales in *2D-RGC*. However, in three dimensions a composite rigid body ($n_r > 1$) has $\chi(3) = 6$ degrees of freedom (three from translation and three from rotation in 'yaw,' 'pitch,' and 'roll'), while a cylinder or axisymmetric body—that lacks marking or is otherwise indistinguishable for rotation around the axis of symmetry—has five. This difference can be illustrated with coordinate labelings.

Being that a line segment has dimension one, only two points are necessary to specify the rigid motions of a rod using a coordinate labeling. Because a complete graph on two vertices has one edge, the resulting rigidity matrix has size $1 \times 2(3)$ and thus right nullspace dimension five (recall from Sec. 2.3.1 that the right nullspace dimension of a rigidity matrix is equal to the degrees of freedom of the corresponding body). If a rigid body is nonplanar, then $3 + 1 = 4$ points are necessary to specify its rigid motions. A complete graph of constraints between 4 vertices (K_4) has 6 edges—when such a graph is embedded in three dimensional space, the constraint-forming edges are rather trivially linearly independent. Thus, the rigidity matrix for a coordinate labeling of such a body has right nullspace dimension equal to $4(3) - 6 = 6$—equivalently, the group $SE(3)$ has order 6 (Cederberg, 2001). If on the other hand, a rigid body is planar but lacking cylindrical symmetry (e.g. a triangle), then $2 + 1 = 3$ points are necessary to specify its rigid motions. As well, K_3 has three edges, and the rigidity of the corresponding coordinate labeling in 3-space has right nullspace dimension equal to $3(3) - 3 = 6$. In the following subsection, it will therefore be necessary to distinguish linear rods ($n_r = 1$), which have five degrees of freedom, from other rigid bodies ($n_r > 1$), which have six.

While rods require differentiation from other rigid components in the treatment below, planar and nonplanar rigid components do not. The coordinate labeling for a planar rigid component R (with rigidity matrix $\boldsymbol{X}$) has three points, but adding a new point along with corresponding constraints to the unperturbed coordinate labeling set does not change the rank of $\boldsymbol{X}$. Hence, in each of the proofs of the next subsection, I assume that each rigid component with $n_r > 1$ is nonplanar and let the corresponding result extend to the case in which one or more components are planar.

A third and final difference between the treatment here of 2D and 3D disordered fiber systems is slightly more subtle. In two dimensions, it was only necessary to consider interactions in which pairs of rigid bodies share ≤ 2 contacts. Owing to the increased number of degrees of freedom for rigid bodies in three dimensions, this will not always be the case in the rigid motifs of the next subsection. As noted in Sec. 2.3.1, a coordinate labeling must be chosen such that no subset of ≥ 2 contained

points are collinear. However, if ≥ 2 contacts occur along a single rod, then there is a possibility in which ≥ 2 of these are collinear (i.e. if they lie along the axis of the rod). Therefore, in treating compositions between rigid bodies sharing ≥ 2 contacts in three dimensions, it is critical to attend to whether or not these contacts are rod-sharing. As in Sec. 3.2, I assume generic conditions wherein if > 2 points do not share a rod, the set of these points is noncollinear.

4.2 Primitive rigid motifs in three dimensions

Here, I present and sketch the proofs of many rigid motifs for the construction of composite rigid components in three dimensions. As in two dimensions, this list is nonexhaustive (and constructing an exhaustive list may be impossible). In order to avoid creating a new litany of symbols, I do not distinguish rods ($n_r = 1$) from other rigid components ($n_r > 1$)—both are called R_i for some i—or rod-sharing contacts from other contacts notationally. However, attention is given to the considerations of the previous subsections within the hypothesis of each proof. I assume as in two dimensions that each rigid component involved in the hypothesis shares no rods (they may of course share intersection points) with other components in the hypothesis. Because points are embedded in 3-space, $\Delta \boldsymbol{p}_{i,j}$ now indicates a 1×3 vector given by $\boldsymbol{p}_i - \boldsymbol{p}_j$ for position vectors $\boldsymbol{p}_i$ and $\boldsymbol{p}_j$. Finally, I note that in cases in which there are more than one motif with x rigid bodies (as the distinction between rods from other rigid bodies opens up this possibility), I distinguish between the different rigid motifs by lettering: *rigid motif 3DxA, 3DxB,...*

Theorem 4.1. *Motif 3D2A: The composition of two rigid components, R_1 and R_2 ($n_r^1, n_r^2 > 1$), intersecting at ≥ 3 distinct points $\boldsymbol{p}_1, \boldsymbol{p}_2, \boldsymbol{p}_3, ...$, is rigid if these points do not all share the same rod.*

Proof. As noted in the previous subsection, I assume these rigid components are both nonplanar, in which case R_1 and R_2 have four points apiece. I choose three of these points to be the intersection points, giving the coordinate labelings $\{\boldsymbol{p}_1, \boldsymbol{p}_2, \boldsymbol{p}_3, \boldsymbol{p}_{R_1}\}$ and $\{\boldsymbol{p}_1, \boldsymbol{p}_2, \boldsymbol{p}_3, \boldsymbol{p}_{R_2}\}$, where $\boldsymbol{p}_{R_1}$ is a point in $R_1 \backslash R_2$ and vice versa. The rigidity matrix for this system is given by:

$$\boldsymbol{X}_1 * \boldsymbol{X}_2 = \begin{bmatrix} \Delta \boldsymbol{p}_{1,R_1} & \mathbf{0} & \mathbf{0} & -\Delta \boldsymbol{p}_{1,R_1} & \mathbf{0} \\ \mathbf{0} & \Delta \boldsymbol{p}_{2,R_1} & \mathbf{0} & -\Delta \boldsymbol{p}_{2,R_1} & \mathbf{0} \\ \mathbf{0} & \mathbf{0} & \Delta \boldsymbol{p}_{3,R_1} & -\Delta \boldsymbol{p}_{3,R_1} & \mathbf{0} \\ \Delta \boldsymbol{p}_{1,2} & -\Delta \boldsymbol{p}_{1,2} & \mathbf{0} & \mathbf{0} & \mathbf{0} \\ \mathbf{0} & \Delta \boldsymbol{p}_{2,3} & -\Delta \boldsymbol{p}_{2,3} & \mathbf{0} & \mathbf{0} \\ \Delta \boldsymbol{p}_{1,3} & \mathbf{0} & -\Delta \boldsymbol{p}_{1,3} & \mathbf{0} & \mathbf{0} \\ \Delta \boldsymbol{p}_{1,R_2} & \mathbf{0} & \mathbf{0} & \mathbf{0} & -\Delta \boldsymbol{p}_{1,R_2} \\ \mathbf{0} & \Delta \boldsymbol{p}_{2,R_2} & \mathbf{0} & \mathbf{0} & -\Delta \boldsymbol{p}_{2,R_2} \\ \mathbf{0} & \mathbf{0} & \Delta \boldsymbol{p}_{3,R_2} & \mathbf{0} & -\Delta \boldsymbol{p}_{3,R_2} \end{bmatrix}, \tag{4.1}$$

where the first three constraints derive from $R_1 \backslash R_2$, the second three from $R_1 \cup R_2$, and the final three from $R_2 \backslash R_1$. Row permutations give that $\boldsymbol{X}_1 * \boldsymbol{X}_2$ is rank equivalent to:

$$\begin{bmatrix} \Delta \boldsymbol{p}_{1,2} & -\Delta \boldsymbol{p}_{1,2} & \mathbf{0} & \mathbf{0} & \mathbf{0} \\ \mathbf{0} & \Delta \boldsymbol{p}_{2,3} & -\Delta \boldsymbol{p}_{2,3} & \mathbf{0} & \mathbf{0} \\ \Delta \boldsymbol{p}_{1,3} & \mathbf{0} & -\Delta \boldsymbol{p}_{1,3} & \mathbf{0} & \mathbf{0} \\ \Delta \boldsymbol{p}_{1,R_1} & \mathbf{0} & \mathbf{0} & -\Delta \boldsymbol{p}_{1,R_1} & \mathbf{0} \\ \mathbf{0} & \Delta \boldsymbol{p}_{2,R_1} & \mathbf{0} & -\Delta \boldsymbol{p}_{2,R_1} & \mathbf{0} \\ \mathbf{0} & \mathbf{0} & \Delta \boldsymbol{p}_{3,R_1} & -\Delta \boldsymbol{p}_{3,R_1} & \mathbf{0} \\ \Delta \boldsymbol{p}_{1,R_2} & \mathbf{0} & \mathbf{0} & \mathbf{0} & -\Delta \boldsymbol{p}_{1,R_2} \\ \mathbf{0} & \Delta \boldsymbol{p}_{2,R_2} & \mathbf{0} & \mathbf{0} & -\Delta \boldsymbol{p}_{2,R_2} \\ \mathbf{0} & \mathbf{0} & \Delta \boldsymbol{p}_{3,R_2} & \mathbf{0} & -\Delta \boldsymbol{p}_{3,R_2} \end{bmatrix}, \tag{4.2}$$

which is a block triangular matrix with diagonal blocks:

$$\left\{ \begin{bmatrix} \Delta \boldsymbol{p}_{1,2} & -\Delta \boldsymbol{p}_{1,2} \end{bmatrix}, \begin{bmatrix} -\Delta \boldsymbol{p}_{2,3} \\ -\Delta \boldsymbol{p}_{1,3} \end{bmatrix}, \begin{bmatrix} -\Delta \boldsymbol{p}_{1,R_1} \\ -\Delta \boldsymbol{p}_{2,R_1} \\ -\Delta \boldsymbol{p}_{3,R_1} \end{bmatrix}, \begin{bmatrix} -\Delta \boldsymbol{p}_{1,R_2} \\ -\Delta \boldsymbol{p}_{2,R_2} \\ -\Delta \boldsymbol{p}_{3,R_2} \end{bmatrix} \right\}, \tag{4.3}$$

As each entry is itself a 1×3 vector, these blocks have ranks 1, 2, 3, and 3, respectively. (Note that if $\boldsymbol{p}_1$, $\boldsymbol{p}_2$, and $\boldsymbol{p}_3$ are all collinear, then at least one of the latter three diagonal blocks lose a dimension—hence, I rule out this case in the hypothesis.) Therefore, $\text{rank}(\boldsymbol{X}_1 * \boldsymbol{X}_2) \geq 9$ and $\dim(\text{null}(\boldsymbol{X}_1 * \boldsymbol{X}_2)) \leq 6$ (as $\boldsymbol{X}_1 * \boldsymbol{X}_2$ has 15 columns). Because a rigid body in three dimensions (lacking any symmetries) has six degrees of freedom, I conclude that $R_1 \cup R_2$ is rigid. □

Theorem 4.2. *Motif 3D3A: Let R_1, R_2, and R_3 be intersecting rigid bodies ($n_r^1, n_r^2, n_r^3 > 1$). If R_1 and R_2 intersect at one point $\boldsymbol{p}_1$, R_1 and R_3 intersect at two points $\boldsymbol{p}_2$ and $\boldsymbol{p}_3$; R_2 and R_3 intersect at two points $\boldsymbol{p}_4$ and $\boldsymbol{p}_5$; then the composition is rigid, unless: $\boldsymbol{p}_1$ shares a rod with both $\boldsymbol{p}_2$ and $\boldsymbol{p}_3$; or $\boldsymbol{p}_1$ shares a rod with both $\boldsymbol{p}_4$ and $\boldsymbol{p}_5$; or $\boldsymbol{p}_2$, $\boldsymbol{p}_3$, $\boldsymbol{p}_4$, and $\boldsymbol{p}_5$ all share the same rod (I exclude these cases via hypothesis).*

Proof. I choose as the coordinate labelings $\{\boldsymbol{p}_1, \boldsymbol{p}_2, \boldsymbol{p}_3, \boldsymbol{p}_{R_1}\}$ for R_1; $\{\boldsymbol{p}_1, \boldsymbol{p}_4, \boldsymbol{p}_5, \boldsymbol{p}_{R_2}\}$ for R_2; and $\{\boldsymbol{p}_2, \boldsymbol{p}_3, \boldsymbol{p}_4, \boldsymbol{p}_5\}$ for R_3, where $\boldsymbol{p}_{R_1}$ lies in $R_1 \backslash (R_2 \cup R_3)$ and $\boldsymbol{p}_{R_2}$ lies in $R_2 \backslash (R_1 \cup R_3)$. Appropriate constraints give the rigidity matrix:

$$\boldsymbol{X}_1 * \boldsymbol{X}_2 * \boldsymbol{X}_3 = \begin{bmatrix}
\Delta\boldsymbol{p}_{1,R_1} & \mathbf{0} & \mathbf{0} & \mathbf{0} & \mathbf{0} & -\Delta\boldsymbol{p}_{1,R_1} & \mathbf{0} \\
\mathbf{0} & \Delta\boldsymbol{p}_{2,R_1} & \mathbf{0} & \mathbf{0} & \mathbf{0} & -\Delta\boldsymbol{p}_{2,R_1} & \mathbf{0} \\
\mathbf{0} & \mathbf{0} & \Delta\boldsymbol{p}_{3,R_1} & \mathbf{0} & \mathbf{0} & -\Delta\boldsymbol{p}_{3,R_1} & \mathbf{0} \\
\Delta\boldsymbol{p}_{1,2} & -\Delta\boldsymbol{p}_{1,2} & \mathbf{0} & \mathbf{0} & \mathbf{0} & \mathbf{0} & \mathbf{0} \\
\Delta\boldsymbol{p}_{1,3} & \mathbf{0} & -\Delta\boldsymbol{p}_{1,3} & \mathbf{0} & \mathbf{0} & \mathbf{0} & \mathbf{0} \\
\mathbf{0} & \Delta\boldsymbol{p}_{2,3} & -\Delta\boldsymbol{p}_{2,3} & \mathbf{0} & \mathbf{0} & \mathbf{0} & \mathbf{0} \\
\Delta\boldsymbol{p}_{1,R_2} & \mathbf{0} & \mathbf{0} & \mathbf{0} & \mathbf{0} & \mathbf{0} & -\Delta\boldsymbol{p}_{1,R_2} \\
\mathbf{0} & \mathbf{0} & \mathbf{0} & \Delta\boldsymbol{p}_{4,R_2} & \mathbf{0} & \mathbf{0} & -\Delta\boldsymbol{p}_{4,R_2} \\
\mathbf{0} & \mathbf{0} & \mathbf{0} & \mathbf{0} & \Delta\boldsymbol{p}_{5,R_2} & \mathbf{0} & -\Delta\boldsymbol{p}_{5,R_2} \\
\Delta\boldsymbol{p}_{1,4} & \mathbf{0} & \mathbf{0} & -\Delta\boldsymbol{p}_{1,4} & \mathbf{0} & \mathbf{0} & \mathbf{0} \\
\Delta\boldsymbol{p}_{1,5} & \mathbf{0} & \mathbf{0} & \mathbf{0} & -\Delta\boldsymbol{p}_{1,5} & \mathbf{0} & \mathbf{0} \\
\mathbf{0} & \mathbf{0} & \mathbf{0} & \Delta\boldsymbol{p}_{4,5} & -\Delta\boldsymbol{p}_{4,5} & \mathbf{0} & \mathbf{0} \\
\mathbf{0} & \Delta\boldsymbol{p}_{2,4} & \mathbf{0} & -\Delta\boldsymbol{p}_{2,4} & \mathbf{0} & \mathbf{0} & \mathbf{0} \\
\mathbf{0} & \Delta\boldsymbol{p}_{2,5} & \mathbf{0} & \mathbf{0} & -\Delta\boldsymbol{p}_{2,5} & \mathbf{0} & \mathbf{0} \\
\mathbf{0} & \mathbf{0} & \Delta\boldsymbol{p}_{3,4} & -\Delta\boldsymbol{p}_{3,4} & \mathbf{0} & \mathbf{0} & \mathbf{0} \\
\mathbf{0} & \mathbf{0} & \Delta\boldsymbol{p}_{3,5} & \mathbf{0} & -\Delta\boldsymbol{p}_{3,5} & \mathbf{0} & \mathbf{0}
\end{bmatrix}, \quad (4.4)$$

where the constraint rows $1-6$ derive from $R_1 \cup R_3$, $7-12$ derive from $R_2 \cup R_3$, and $13-16$ derive from R_3 only. I use row permutations to find that $\boldsymbol{X}_1 * \boldsymbol{X}_2 * \boldsymbol{X}_3$ is rank equivalent to the

block triangular matrix:

$$\begin{bmatrix}
\Delta\boldsymbol{p}_{1,2} & -\Delta\boldsymbol{p}_{1,2} & \mathbf{0} & \mathbf{0} & \mathbf{0} & \mathbf{0} & \mathbf{0} \\
\Delta\boldsymbol{p}_{1,3} & \mathbf{0} & -\Delta\boldsymbol{p}_{1,3} & \mathbf{0} & \mathbf{0} & \mathbf{0} & \mathbf{0} \\
\mathbf{0} & \Delta\boldsymbol{p}_{2,3} & -\Delta\boldsymbol{p}_{2,3} & \mathbf{0} & \mathbf{0} & \mathbf{0} & \mathbf{0} \\
\Delta\boldsymbol{p}_{1,4} & \mathbf{0} & \mathbf{0} & -\Delta\boldsymbol{p}_{1,4} & \mathbf{0} & \mathbf{0} & \mathbf{0} \\
\mathbf{0} & \Delta\boldsymbol{p}_{2,4} & \mathbf{0} & -\Delta\boldsymbol{p}_{2,4} & \mathbf{0} & \mathbf{0} & \mathbf{0} \\
\mathbf{0} & \mathbf{0} & \Delta\boldsymbol{p}_{3,4} & -\Delta\boldsymbol{p}_{3,4} & \mathbf{0} & \mathbf{0} & \mathbf{0} \\
\Delta\boldsymbol{p}_{1,5} & \mathbf{0} & \mathbf{0} & \mathbf{0} & -\Delta\boldsymbol{p}_{1,5} & \mathbf{0} & \mathbf{0} \\
\mathbf{0} & \mathbf{0} & \mathbf{0} & \Delta\boldsymbol{p}_{4,5} & -\Delta\boldsymbol{p}_{4,5} & \mathbf{0} & \mathbf{0} \\
\mathbf{0} & \Delta\boldsymbol{p}_{2,5} & \mathbf{0} & \mathbf{0} & -\Delta\boldsymbol{p}_{2,5} & \mathbf{0} & \mathbf{0} \\
\mathbf{0} & \mathbf{0} & \Delta\boldsymbol{p}_{3,5} & \mathbf{0} & -\Delta\boldsymbol{p}_{3,5} & \mathbf{0} & \mathbf{0} \\
\Delta\boldsymbol{p}_{1,R_1} & \mathbf{0} & \mathbf{0} & \mathbf{0} & \mathbf{0} & -\Delta\boldsymbol{p}_{1,R_1} & \mathbf{0} \\
\mathbf{0} & \Delta\boldsymbol{p}_{2,R_1} & \mathbf{0} & \mathbf{0} & \mathbf{0} & -\Delta\boldsymbol{p}_{2,R_1} & \mathbf{0} \\
\mathbf{0} & \mathbf{0} & \Delta\boldsymbol{p}_{3,R_1} & \mathbf{0} & \mathbf{0} & -\Delta\boldsymbol{p}_{3,R_1} & \mathbf{0} \\
\Delta\boldsymbol{p}_{1,R_2} & \mathbf{0} & \mathbf{0} & \mathbf{0} & \mathbf{0} & \mathbf{0} & -\Delta\boldsymbol{p}_{1,R_2} \\
\mathbf{0} & \mathbf{0} & \mathbf{0} & \Delta\boldsymbol{p}_{4,R_2} & \mathbf{0} & \mathbf{0} & -\Delta\boldsymbol{p}_{4,R_2} \\
\mathbf{0} & \mathbf{0} & \mathbf{0} & \mathbf{0} & \Delta\boldsymbol{p}_{5,R_2} & \mathbf{0} & -\Delta\boldsymbol{p}_{5,R_2}
\end{bmatrix}. \quad (4.5)$$

I show in the following paragraph that the diagonal blocks:

$$\left\{ \begin{bmatrix} \Delta\boldsymbol{p}_{1,2} & -\Delta\boldsymbol{p}_{1,2} \end{bmatrix}, \begin{bmatrix} -\Delta\boldsymbol{p}_{1,3} \\ -\Delta\boldsymbol{p}_{2,3} \end{bmatrix}, \begin{bmatrix} -\Delta\boldsymbol{p}_{1,4} \\ -\Delta\boldsymbol{p}_{2,4} \\ -\Delta\boldsymbol{p}_{3,4} \end{bmatrix}, \begin{bmatrix} -\Delta\boldsymbol{p}_{1,5} \\ -\Delta\boldsymbol{p}_{4,5} \\ -\Delta\boldsymbol{p}_{2,5} \\ -\Delta\boldsymbol{p}_{3,5} \end{bmatrix}, \begin{bmatrix} -\Delta\boldsymbol{p}_{1,R_1} \\ -\Delta\boldsymbol{p}_{2,R_1} \\ -\Delta\boldsymbol{p}_{3,R_1} \end{bmatrix}, \begin{bmatrix} -\Delta\boldsymbol{p}_{1,R_2} \\ -\Delta\boldsymbol{p}_{4,R_2} \\ -\Delta\boldsymbol{p}_{5,R_2} \end{bmatrix} \right\} \quad (4.6)$$

have ranks 1, 2, 3, 3, 3, and 3, respectively.

The first two and last two of these block rank claims are trivial under the hypotheses that $\{\boldsymbol{p}_1, \boldsymbol{p}_2, \boldsymbol{p}_3\}$ and $\{\boldsymbol{p}_1, \boldsymbol{p}_4, \boldsymbol{p}_5\}$ are not rod-sharing sets. The third block would lose a dimension if some three member subset of $\{\boldsymbol{p}_1, \boldsymbol{p}_2, \boldsymbol{p}_3, \boldsymbol{p}_4\}$ were collinear. First, $\{\boldsymbol{p}_1, \boldsymbol{p}_2, \boldsymbol{p}_3\}$ is assumed noncollinear. In addition, neither $\{\boldsymbol{p}_1, \boldsymbol{p}_2, \boldsymbol{p}_4\}$ nor $\{\boldsymbol{p}_1, \boldsymbol{p}_3, \boldsymbol{p}_4\}$ may be collinear, as each of these sets contains points from R_1, R_2, and R_3. Collinearity of either of these sets would in turn imply that each rigid component contains the same rod. If $\{\boldsymbol{p}_2, \boldsymbol{p}_3, \boldsymbol{p}_4\}$ were collinear, then interchanging of $\boldsymbol{p}_4$ and $\boldsymbol{p}_5$ would preserve the block rank of three (under the given hypotheses), which I show here. Because $\{\boldsymbol{p}_2, \boldsymbol{p}_3, \boldsymbol{p}_4, \boldsymbol{p}_5\}$ is assumed noncollinear, collinearity of the set $\{\boldsymbol{p}_2, \boldsymbol{p}_3, \boldsymbol{p}_4\}$ guarantees noncollinearity of the set $\{\boldsymbol{p}_2, \boldsymbol{p}_3, \boldsymbol{p}_5\}$ (see Fig. 4.1). As it may be seen that such interchanging does

not affect the rank of the previously discussed blocks, I conclude that proper choice of $\boldsymbol{p}_4$ and $\boldsymbol{p}_5$ assures full rank of the third diagonal block.

The fourth block has rank ≤ 2 only if either a four member subset of $\{\boldsymbol{p}_1, \boldsymbol{p}_2, \boldsymbol{p}_3, \boldsymbol{p}_4, \boldsymbol{p}_5\}$ is collinear—which is impossible given the hypotheses—or two three member sets of the involved constraints are both collinear. This latter situation is also impossible because $\Delta\boldsymbol{p}_{1,5}$ cannot be collinear with any of the other three constraints in the block. This statement follows from the hypothesis that $\{\boldsymbol{p}_1, \boldsymbol{p}_4, \boldsymbol{p}_5\}$ is not collinear, and from the observation that neither $\{\boldsymbol{p}_1, \boldsymbol{p}_2, \boldsymbol{p}_5\}$ nor $\{\boldsymbol{p}_1, \boldsymbol{p}_3, \boldsymbol{p}_5\}$ can be collinear (for the same reason that neither $\{\boldsymbol{p}_1, \boldsymbol{p}_2, \boldsymbol{p}_4\}$ nor $\{\boldsymbol{p}_1, \boldsymbol{p}_3, \boldsymbol{p}_4\}$ can be collinear). Therefore, because the rank of a matrix is bounded below by the sum of the ranks of its diagonal blocks, the composite rigidity matrix $\boldsymbol{X}_1 * \boldsymbol{X}_2 * \boldsymbol{X}_3$ has rank 15 and right nullspace dimension six. □

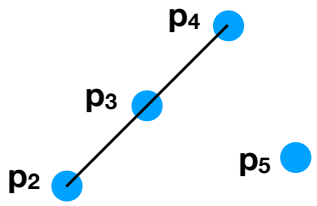

Figure 4.1: **If $\{\boldsymbol{p}_2, \boldsymbol{p}_3, \boldsymbol{p}_4, \boldsymbol{p}_5\}$ is noncollinear, then $\{\boldsymbol{p}_2, \boldsymbol{p}_3, \boldsymbol{p}_4\}$ and $\{\boldsymbol{p}_2, \boldsymbol{p}_3, \boldsymbol{p}_5\}$ cannot simultaneously be collinear.**

Motif 3D2A motif is somewhat analogous to *Motif 2D2*—as in two dimensions, individuals rods may only intersect at one point, and so at least one of the two bodies in this motif must contain more than one rod. However, the hypothesized condition—that not all of the intersections share the same rod—necessitates that neither R_1 nor R_2 is a single rod, and therefore both $n_r^1 > 1$ and $n_r^2 > 1$. The case that one of these components is a single rod begs a different motif, beginning the consideration of rigid motifs featuring compositions of individual rods with other (non-axisymmetric) rigid components.

Theorem 4.3. *Motif 3D2B: The composition of a rigid body R_1 ($n_r^1 > 1$) with a single rod R_2 is rigid if R_1 and R_2 intersect at ≥ 2 points ($\boldsymbol{p}_1$ and $\boldsymbol{p}_2$).*

Proof. Choose the coordinate labeling for R_2 to be $\{\boldsymbol{p}_1, \boldsymbol{p}_2\}$ and that for R_1 to be $\{\boldsymbol{p}_1, \boldsymbol{p}_2, \boldsymbol{p}_{R_{1a}}, \boldsymbol{p}_{R_{1b}}\}$. The constraint graph of the composition is then exactly the same as that for R_1 individually, which is rigid by hypothesis. □

Theorem 4.4. *Motif 3D3C: If two rigid bodies R_1 and R_2 ($n_r^1, n_r^2 > 1$) intersect at ≥ 2 points $\boldsymbol{p}_1$ and $\boldsymbol{p}_2$, and also each intersect another distinct rod R_3 ($n_r^3 = 1$) at one point apiece, such that $R_1 \cap R_3 = \boldsymbol{p}_3$ and $R_2 \cap R_3 = \boldsymbol{p}_4$, then the composite body is rigid—so long as neither $\boldsymbol{p}_3$ nor $\boldsymbol{p}_4$ is collinear with both $\boldsymbol{p}_1$ and $\boldsymbol{p}_2$.*

Proof. I choose as coordinate labelings $\{\boldsymbol{p}_1, \boldsymbol{p}_2, \boldsymbol{p}_3, \boldsymbol{p}_{R_1}\}$ for R_1, $\{\boldsymbol{p}_1, \boldsymbol{p}_2, \boldsymbol{p}_4, \boldsymbol{p}_{R_2}\}$ for R_2, and $\{\boldsymbol{p}_3, \boldsymbol{p}_4\}$ for R_3, where $\boldsymbol{p}_{R_1}$ is not collinear with any pair of points in $\{\boldsymbol{p}_1, \boldsymbol{p}_2, \boldsymbol{p}_3\}$ and $\boldsymbol{p}_{R_2}$ to not be collinear with any pair of points in $\{\boldsymbol{p}_1, \boldsymbol{p}_2, \boldsymbol{p}_4\}$. Upon row rearrangement, this choice gives the rigidity matrix:

$$\boldsymbol{X}_1 * \boldsymbol{X}_2 * \boldsymbol{X}_3 = \begin{bmatrix} \Delta\boldsymbol{p}_{1,2} & -\Delta\boldsymbol{p}_{1,2} & \mathbf{0} & \mathbf{0} & \mathbf{0} & \mathbf{0} \\ \Delta\boldsymbol{p}_{1,3} & \mathbf{0} & -\Delta\boldsymbol{p}_{1,3} & \mathbf{0} & \mathbf{0} & \mathbf{0} \\ \mathbf{0} & \Delta\boldsymbol{p}_{2,3} & -\Delta\boldsymbol{p}_{2,3} & \mathbf{0} & \mathbf{0} & \mathbf{0} \\ \Delta\boldsymbol{p}_{1,4} & \mathbf{0} & \mathbf{0} & -\Delta\boldsymbol{p}_{1,4} & \mathbf{0} & \mathbf{0} \\ \mathbf{0} & \Delta\boldsymbol{p}_{2,4} & \mathbf{0} & -\Delta\boldsymbol{p}_{2,4} & \mathbf{0} & \mathbf{0} \\ \mathbf{0} & \mathbf{0} & \Delta\boldsymbol{p}_{3,4} & -\Delta\boldsymbol{p}_{3,4} & \mathbf{0} & \mathbf{0} \\ \Delta\boldsymbol{p}_{1,R_1} & \mathbf{0} & \mathbf{0} & \mathbf{0} & -\Delta\boldsymbol{p}_{1,R_1} & \mathbf{0} \\ \mathbf{0} & \Delta\boldsymbol{p}_{2,R_1} & \mathbf{0} & \mathbf{0} & -\Delta\boldsymbol{p}_{2,R_1} & \mathbf{0} \\ \mathbf{0} & \mathbf{0} & \Delta\boldsymbol{p}_{3,R_1} & \mathbf{0} & -\Delta\boldsymbol{p}_{3,R_1} & \mathbf{0} \\ \Delta\boldsymbol{p}_{1,R_2} & \mathbf{0} & \mathbf{0} & \mathbf{0} & \mathbf{0} & -\Delta\boldsymbol{p}_{1,R_2} \\ \mathbf{0} & \Delta\boldsymbol{p}_{2,R_2} & \mathbf{0} & \mathbf{0} & \mathbf{0} & -\Delta\boldsymbol{p}_{2,R_2} \\ \mathbf{0} & \mathbf{0} & \mathbf{0} & \Delta\boldsymbol{p}_{4,R_2} & \mathbf{0} & -\Delta\boldsymbol{p}_{4,R_2} \end{bmatrix}, \tag{4.7}$$

which has diagonal blocks:

$$\left\{ \begin{bmatrix} \Delta\boldsymbol{p}_{1,2} & -\Delta\boldsymbol{p}_{1,2} \end{bmatrix}, \begin{bmatrix} -\Delta\boldsymbol{p}_{1,3} \\ -\Delta\boldsymbol{p}_{2,3} \end{bmatrix}, \begin{bmatrix} -\Delta\boldsymbol{p}_{1,4} \\ -\Delta\boldsymbol{p}_{2,4} \\ -\Delta\boldsymbol{p}_{3,4} \end{bmatrix}, \begin{bmatrix} -\Delta\boldsymbol{p}_{1,R_1} \\ -\Delta\boldsymbol{p}_{2,R_1} \\ -\Delta\boldsymbol{p}_{3,R_1} \end{bmatrix}, \begin{bmatrix} -\Delta\boldsymbol{p}_{1,R_2} \\ -\Delta\boldsymbol{p}_{2,R_2} \\ -\Delta\boldsymbol{p}_{4,R_2} \end{bmatrix} \right\}. \tag{4.8}$$

To establish that the middle block has full rank, I first claim that—while it is not directly stated in the hypothesis—neither $\boldsymbol{p}_2$ nor $\boldsymbol{p}_1$ lie collinear with both $\boldsymbol{p}_3$ and $\boldsymbol{p}_4$. Otherwise, one of $\boldsymbol{p}_2$ or $\boldsymbol{p}_1$

would lie along the rod R_3, which is nonsensical. This noncollinearity, along with the noncollinearity of the sets $\{\boldsymbol{p}_1, \boldsymbol{p}_2, \boldsymbol{p}_3\}$ and $\{\boldsymbol{p}_1, \boldsymbol{p}_2, \boldsymbol{p}_4\}$, establishes the full rank of the middle block. Because I have chosen $\boldsymbol{p}_{R_1}$ and $\boldsymbol{p}_{R_2}$ to not be collinear with any pair of points in their respective coordinate labelings, and because of noncollinearity of the sets $\{\boldsymbol{p}_1, \boldsymbol{p}_2, \boldsymbol{p}_3\}$ and $\{\boldsymbol{p}_1, \boldsymbol{p}_2, \boldsymbol{p}_4\}$, it is trivial that each of the remaining blocks has full row rank. Therefore $\boldsymbol{X}_1 * \boldsymbol{X}_2 * \boldsymbol{X}_3$ has rank 12 and right nullspace dimension 6. □

Theorem 4.5. *Motif 3D4A: If one rigid body R_1 ($n_r^1 > 1$) intersects three rods R_2, R_3, R_4 ($n_r^2, n_r^3, n_r^4 = 1$) at the points $\boldsymbol{p}_1, \boldsymbol{p}_2, \boldsymbol{p}_3$ (respectively); R_2 intersects R_3 at $\boldsymbol{p}_4$; and R_3 intersects R_4 at $\boldsymbol{p}_5$, then the composite body is rigid unless $\boldsymbol{p}_1$, $\boldsymbol{p}_2$ and $\boldsymbol{p}_3$ are collinear.*

Proof. I choose as (minimal) coordinate labelings $\{\boldsymbol{p}_1, \boldsymbol{p}_2, \boldsymbol{p}_3, \boldsymbol{p}_{R_1}\}$ for R_1 (where $\boldsymbol{p}_{R_1}$ is a point in R_1 that is not collinear with any pair of points in $\{\boldsymbol{p}_1, \boldsymbol{p}_2, \boldsymbol{p}_3\}$), $\{\boldsymbol{p}_1, \boldsymbol{p}_4\}$ for R_2, and $\{\boldsymbol{p}_3, \boldsymbol{p}_5\}$ for R_4. However, the rod R_3 contains three intersection points. Therefore, either pair can be chosen as an appropriate coordinate labeling (I choose $\{\boldsymbol{p}_4, \boldsymbol{p}_5\}$), but an augmented constraint must be added to enforce the condition that these three points must remain collinear (as in *Motif 2D5* of Sec. 3.2):

$$\boldsymbol{u}_2 = s\boldsymbol{u}_4 + (1-s)\boldsymbol{u}_5, \tag{4.9}$$

where $s = \frac{|\Delta \boldsymbol{p}_{2,5}|}{|\Delta \boldsymbol{p}_{4,5}|}$. Letting $\boldsymbol{I_3}$ be the 3×3 identity matrix, and $\mathbf{0_3}$ the 3×3 all-zero matrix, these augmented constraints give the composite rigidity matrix:

$$\boldsymbol{X}_1 * \boldsymbol{X}_2 * \boldsymbol{X}_3 * \boldsymbol{X}_4 = \begin{bmatrix} \Delta \boldsymbol{p}_{1,2} & -\Delta \boldsymbol{p}_{1,2} & \mathbf{0} & \mathbf{0} & \mathbf{0} & \mathbf{0} \\ \Delta \boldsymbol{p}_{1,3} & \mathbf{0} & -\Delta \boldsymbol{p}_{1,3} & \mathbf{0} & \mathbf{0} & \mathbf{0} \\ \mathbf{0} & \Delta \boldsymbol{p}_{2,3} & -\Delta \boldsymbol{p}_{2,3} & \mathbf{0} & \mathbf{0} & \mathbf{0} \\ \Delta \boldsymbol{p}_{1,R_1} & \mathbf{0} & \mathbf{0} & -\Delta \boldsymbol{p}_{1,R_1} & \mathbf{0} & \mathbf{0} \\ \mathbf{0} & \Delta \boldsymbol{p}_{2,R_1} & \mathbf{0} & -\Delta \boldsymbol{p}_{2,R_1} & \mathbf{0} & \mathbf{0} \\ \mathbf{0} & \mathbf{0} & \Delta \boldsymbol{p}_{3,R_1} & -\Delta \boldsymbol{p}_{3,R_1} & \mathbf{0} & \mathbf{0} \\ \Delta \boldsymbol{p}_{1,4} & \mathbf{0} & \mathbf{0} & \mathbf{0} & -\Delta \boldsymbol{p}_{1,4} & \mathbf{0} \\ \mathbf{0} & \mathbf{0} & \Delta \boldsymbol{p}_{3,5} & \mathbf{0} & \mathbf{0} & -\Delta \boldsymbol{p}_{3,5} \\ \mathbf{0} & \mathbf{0} & \mathbf{0} & \mathbf{0} & \Delta \boldsymbol{p}_{4,5} & -\Delta \boldsymbol{p}_{4,5} \\ \mathbf{0_3} & \boldsymbol{I_3} & \mathbf{0_3} & \mathbf{0_3} & s\boldsymbol{I_3} & (1-s)\boldsymbol{I_3} \end{bmatrix}. \tag{4.10}$$

Elementary row operations give that this matrix is rank equivalent to:

$$\begin{bmatrix} \Delta \boldsymbol{p}_{1,2} & -\Delta \boldsymbol{p}_{1,2} & \mathbf{0} & \mathbf{0} & \mathbf{0} & \mathbf{0} \\ \Delta \boldsymbol{p}_{1,3} & \mathbf{0} & -\Delta \boldsymbol{p}_{1,3} & \mathbf{0} & \mathbf{0} & \mathbf{0} \\ \mathbf{0} & \Delta \boldsymbol{p}_{2,3} & -\Delta \boldsymbol{p}_{2,3} & \mathbf{0} & \mathbf{0} & \mathbf{0} \\ \Delta \boldsymbol{p}_{1,R_1} & \mathbf{0} & \mathbf{0} & -\Delta \boldsymbol{p}_{1,R_1} & \mathbf{0} & \mathbf{0} \\ \mathbf{0} & \Delta \boldsymbol{p}_{2,R_1} & \mathbf{0} & -\Delta \boldsymbol{p}_{2,R_1} & \mathbf{0} & \mathbf{0} \\ \mathbf{0} & \mathbf{0} & \Delta \boldsymbol{p}_{3,R_1} & -\Delta \boldsymbol{p}_{3,R_1} & \mathbf{0} & \mathbf{0} \\ \Delta \boldsymbol{p}_{1,4} & \mathbf{0} & \mathbf{0} & \mathbf{0} & -\Delta \boldsymbol{p}_{1,4} & \mathbf{0} \\ \mathbf{0} & -\frac{1}{1-s}\Delta \boldsymbol{p}_{3,5} & \Delta \boldsymbol{p}_{3,5} & \mathbf{0} & \frac{s}{1-s}\Delta \boldsymbol{p}_{3,5} & \mathbf{0} \\ \mathbf{0} & \frac{-1}{1-s}\Delta \boldsymbol{p}_{4,5} & \mathbf{0} & \mathbf{0} & \left(1+\frac{s}{1-s}\right)\Delta \boldsymbol{p}_{4,5} & \mathbf{0} \\ \mathbf{0_3} & -\boldsymbol{I_3} & \mathbf{0_3} & \mathbf{0_3} & s\boldsymbol{I_3} & (1-s)\boldsymbol{I_3} \end{bmatrix}, \tag{4.11}$$

which has full rank blocks of rank $1, 2, 3, 3$, and 3. The first three and last of these claims are trivial, given that $\boldsymbol{p}_1$, $\boldsymbol{p}_2$, and $\boldsymbol{p}_3$ are noncollinear. The penultimate claim is true because it would be nonsensical for any collinearities to exist between $\Delta \boldsymbol{p}_{1,4}$, $\Delta \boldsymbol{p}_{3,4}$, and $\Delta \boldsymbol{p}_{4,5}$. □

The final two motifs proven here involve individual rods only. The first (*Motif 3D3B*) is obviously analogous to *Motif 2D3*, although *Motif 3DB* is only applicable at the scale of single rods. Together, Motifs *3D3B* and *3D2B* show that a 3-clique community is also rigid in three dimensions. The last is analogous to *Motif 2D5*, but an additional rod is apparently needed to constrain this structure in three dimensions.

Theorem 4.6. *Motif 3D3B: A 3-clique of rods ($n_r^1, n_r^2, n_r^3 = 1$), wherein R_1 intersects R_3 at $\boldsymbol{p}_1$, R_1 intersects R_2 at $\boldsymbol{p}_2$, and R_2 intersects R_3 at $\boldsymbol{p}_3$, is rigid.*

Proof. Choose as the coordinate labelings the respective intersection points. The resulting rigidity matrix is of size 3×9 and trivially has full row rank. □

Theorem 4.7. *Motif 3D6A: If six rods ($n_r^1 = 1, \cdots, n_r^6 = 1$) intersect in the strutted fashion of* Motif 2D5*—such that $\boldsymbol{p}_1 \in (R_1 \cap R_3)$, $\boldsymbol{p}_2 \in (R_2 \cap R_3)$, $\boldsymbol{p}_3 \in (R_1 \cap R_4)$, $\boldsymbol{p}_4 \in (R_2 \cap R_4)$, $\boldsymbol{p}_5 \in (R_1 \cap R_5)$, $\boldsymbol{p}_6 \in (R_2 \cap R_5)$, $\boldsymbol{p}_7 \in (R_1 \cap R_6)$, and $\boldsymbol{p}_8 \in (R_2 \cap R_6)$—then their composition is rigid.*

Rather, then prove this analytically, I form the corresponding rigidity matrix, and use symbolic algebra to find that it has full row rank. I choose as minimal coordinate labelings $\{\boldsymbol{p}_1, \boldsymbol{p}_5\}$ for R_1, $\{\boldsymbol{p}_2, \boldsymbol{p}_6\}$ for R_2, $\{\boldsymbol{p}_1, \boldsymbol{p}_2\}$ for R_3, $\{\boldsymbol{p}_3, \boldsymbol{p}_4\}$ for R_4, $\{\boldsymbol{p}_5, \boldsymbol{p}_6\}$ for R_5, and $\{\boldsymbol{p}_7, \boldsymbol{p}_8\}$ for R_6. As in *Motif 2D5* and *Motif 3D4A*, I introduce augmented constraints to ensure that the positioning of $\boldsymbol{p}_3$ and $\boldsymbol{p}_5$ each stay fixed relative to $\boldsymbol{p}_1$ and $\boldsymbol{p}_7$ (and both $\boldsymbol{p}_4$ and $\boldsymbol{p}_6$ each stay fixed relative to $\boldsymbol{p}_2$ and $\boldsymbol{p}_8$) for all time.

$$\boldsymbol{X}_1 * \ldots * \boldsymbol{X}_5 = \begin{bmatrix} \Delta\boldsymbol{p}_{1,2} & -\Delta\boldsymbol{p}_{1,2} & \mathbf{0} & \mathbf{0} & \mathbf{0} & \mathbf{0} & \mathbf{0} & \mathbf{0} \\ \mathbf{0} & \mathbf{0} & \Delta\boldsymbol{p}_{3,4} & -\Delta\boldsymbol{p}_{3,4} & \mathbf{0} & \mathbf{0} & \mathbf{0} & \mathbf{0} \\ \Delta\boldsymbol{p}_{1,5} & \mathbf{0} & \mathbf{0} & \mathbf{0} & -\Delta\boldsymbol{p}_{1,5} & \mathbf{0} & \mathbf{0} & \mathbf{0} \\ \mathbf{0} & \mathbf{0} & \mathbf{0} & \mathbf{0} & \Delta\boldsymbol{p}_{5,6} & -\Delta\boldsymbol{p}_{5,6} & \mathbf{0} & \mathbf{0} \\ \mathbf{0} & \Delta\boldsymbol{p}_{2,6} & \mathbf{0} & \mathbf{0} & -\Delta\boldsymbol{p}_{2,6} & \mathbf{0} & \mathbf{0} & \\ \mathbf{0} & \Delta\boldsymbol{p}_{2,6} & \mathbf{0} & \mathbf{0} & \mathbf{0} & \mathbf{0} & \Delta\boldsymbol{p}_{7,8} & -\Delta\boldsymbol{p}_{7,8} \\ s_1\boldsymbol{I_3} & \mathbf{0} & -\mathbf{1} & \mathbf{0} & \mathbf{0} & \mathbf{0} & (1-s_1)\boldsymbol{I_3} & \mathbf{0} \\ s_2\boldsymbol{I_3} & \mathbf{0} & \mathbf{0} & \mathbf{0} & -\mathbf{1} & \mathbf{0} & (1-s_2)\boldsymbol{I_3} & \mathbf{0} \\ \mathbf{0} & s_3\boldsymbol{I_3} & \mathbf{0} & -\mathbf{1} & \mathbf{0} & \mathbf{0} & \mathbf{0} & (1-s_3)\boldsymbol{I_3} \\ \mathbf{0} & s_4\boldsymbol{I_3} & \mathbf{0} & \mathbf{0} & -\mathbf{1} & \mathbf{0} & \mathbf{0} & (1-s_4)\boldsymbol{I_3} \end{bmatrix}, \quad (4.12)$$

where $s_1 = \frac{|\Delta \boldsymbol{p}_{1,3}|}{|\Delta \boldsymbol{p}_{1,7}|}$, $s_2 = \frac{|\Delta \boldsymbol{p}_{1,5}|}{|\Delta \boldsymbol{p}_{1,7}|}$, $s_3 = \frac{|\Delta \boldsymbol{p}_{2,4}|}{|\Delta \boldsymbol{p}_{2,8}|}$, $s_4 = \frac{|\Delta \boldsymbol{p}_{2,6}|}{|\Delta \boldsymbol{p}_{2,8}|}$. It is quite tedious to show that the row rank of this matrix is 18 (and therefore right nullspace dimension 6)—instead, I have verified this only with *Mathematica*.

While I conjecture that these motifs sufficiently characterize rigid graphs with size $n_r \leq 3$, the complexity of these motifs clearly increases greatly with the number of components involved. I have outlined a method to search for motif candidates containing any number of individual components $\leq x$ for some x in Sec. 4.5. A contact graph representation of the seven motifs proven above is shown in Fig. 4.2.

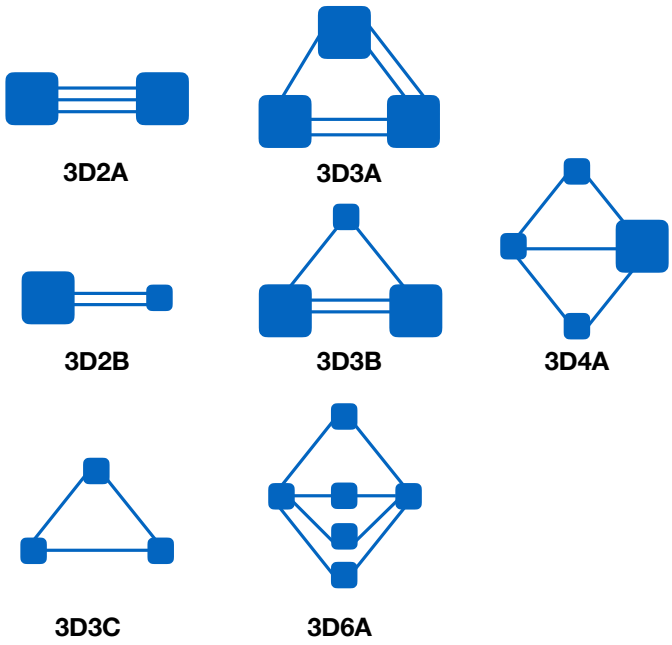

Figure 4.2: **Seven motifs featuring individual rods (small) and other non-axisymmetric ($n_r > 1$) rigid components (big) are proven to be rigid in Sec. 4.2.** In the rod contact graph representation, nodes represent rigid components and edges represent contacts. These images do not depict certain conditions regarding which constacts may or may not be rod-sharing.

4.3 Algorithmic implementation

The algorithmic framework of *3D-RGC* is essentially similar to that of *2D-RGC* (discussed in Sec. 3.3)—however, some important differences do arise. First, as discussed in Sec. 4.2.1, it is essential to distinguish between rigid components that are individual rods ($n_r = 1$) and those which are not. Therefore, a graph attribute 'rods_in_node' is employed to track the size of each

rigid component throughout RGC (this is also used to identify the sizes of the rigid components at the conclusion of the algorithm), and each motif identification function discriminates accordingly. For instance, Motifs *3D3B* and *3D6A* are employed first, as these act exclusively on individual rods. As in the two dimensional case, *3-clique communities* (which are rigid via *Motif 3D3B* and successive application of *Motif 3D2B*) are compressed rather than explicit *3-cliques*, for the sake of computational efficiency. However, care must be taken to ensure that each node in this *3-clique community* is a rod, as *3-clique communities* of non-axisymmetric rigid bodies are not necessarily rigid in three dimensions. After identification/compression of all *3-clique communities* and of all instances of *Motif 3D6A*, the same identification/compression *while* loop of Algorithm 2 is applied iteratively (using the remaining rigid motifs of the previous subsection) upon the candidate graph.

Additionally, a *multi-graph* representation is used to keep track of which edges in the contact graph are rod-sharing. The original contact graph, in which each node represents a single rod ,contains no multi-edges. But as compressions occur, multiple contacts between rods are represented via *multi-edges* rather than with weights (which are used to this end in Algorithm 2). Each of these edges is associated with a tuple edge attribute 'original_edge,' which refers to the corresponding edge in the original contact graph. Rod-sharing contacts are distinguished by multi-edges that share a node in the original contact graph—motif identification functions distinguish accordingly.

A final consideration differentiating *2D-RGC* and *3D-RGC* is that, while I conjecture that rigidity percolation is indiscriminate to the order of motif compression in the former case (see Sec. 3.3), this is certainly not the case in three dimensions. A simple example in which RGC identifies different rigid components for different motif compression orderings is displayed in Fig. 4.3. Ideally, I could account for this dependence on motif compression order by implementing upon each candidate graph all possible 7! orderings of *3D-RGC*. As this algorithm is by design a 'sufficient but not necessary' rigidity detection algorithm, detection using any of these possible orderings would guarantee the candidate configuration is rigid. However, given the computational cost of *3D-RGC* as implemented in this study (see Sec. 4.4.3), such exhaustive analysis is prohibitively expensive. Instead, the ordering is determined for each candidate graph using a random permutation. After identification/compression of *3-clique communities* and instances of *Motif 3D6A*, the remaining identification-compression order is chosen at random and fixed until convergence. In Sec. 4.4.2, I show that while this role of

ordering may affect the rigidity analysis of a particular candidate graph in certain cases, it has no effect on the macroscopic characterization of rigidity percolation.

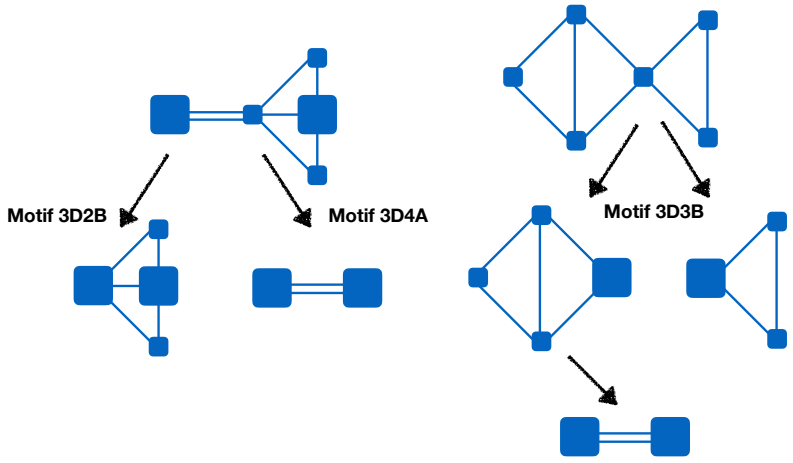

Figure 4.3: **Different orderings of motif compression in *3D-RGC* can give different results for certain graphs.** *Left*: The top five-node graph could be compressed into either four nodes (via *Motif 3D2B*) or two nodes (*3D4a*). Depending on whether the objective is to reduce the number of vertices in the graph, or to agglomerate the most rods into a single node (greedily), one or the other option may be preferable. *Right*: Even in the initial identification/compression of *3-clique communities*, choices must be made—the base contact graph can be compressed into either four or three nodes, depending on which 3-clique community is compressed first. Graphs with adjacent *3-clique communities* could be compressed in alternative ways, as shown here. In the implementation of the next section, *3-clique communities* will be compressed greedily (the largest will be compressed first, as in the right path which leaves three nodes). Note that such a choice is not necessary in two dimensions, wherein *2D-RGC-5* need not distinguish whether a node represents a rod or a larger rigid body (giving that any adjacent 3-clique communities are mutually rigid). An observation related to this problem is that the middle node—that shared by both 3-clique communities—is rigid with respect to either 3-clique community, but the algorithm of *3D-RGC* necessitates that it be identified as being part of a single rigid component only.

One more detail is used for computational purposes—as in the two-dimensional case, each rod in a three-dimensional rigid component (containing $n_r > 1$ rods) trivially must have at least two contacts. In the language of graph theory, rigid components (of more than one rod) are therefore contained only in the 2-core of the contact graph. Therefore, during initialization, *3D-RGC* extracts from the full candidate graph the 2-core subgraph, upon which rigid motifs are identified and compressed. (This time-saving procedure ought have been implemented in the two-dimensional case

as well, but it is certainly not as important to efficiency as in the study of Shi et al. 2014, which considers sparser networks.) Furthermore, non-percolating nodes with degree 1 can be eliminated throughout the identification-compression process (however, this does not seem to significantly enhance the speed of the algorithm).

A reader at this point may wonder: why is there not a number at the end of *3D-RGC* as in *2D-RGC-3,5*? Because there is an exact method for two dimensional rigidity characterization, I could equivocally show that *2D-RGC-5* exactly characterizes rigid components containing up to $n_r = 5$ (actually 6 as shown in Sec. 3.5) individual rigid bodies. This is not the case in three dimensions—I will show in Sec. 4.5 that the current version of *3D-RGC* identifies all rigid components containing ≤ 5 *rods* but not necessarily all rigid components containing ≤ 5 rigid components (which may or may not be axisymmetric).

4.4 Numerical experiments

4.4 Experimental design

A model fully true to the experimental system of nanoparticle packings would involve sequentially packing fibers of some aspect ratio (with rejection in the case that they take up the same volume). However, I assume for simplicity (and computational expediency) that this is not terribly significant to capturing the statistical physics of rigidity (as in Shi et al. 2014 as well as other simulation-based studies). Future study could verify this assumption, using a grid-based random sequential adsorption process akin to that of Viot et al. (1992). Such an approach, which is implemented for study of contact percolation by Berhan and Sastry (2007), would also require a distinction between the radius of impenetrable volume and that of particle interaction. Instead, I simply modify the measure of measurement of volume fraction ϕ from the raw geometry-free assumption to Balberg's formula (for sphereocylinders of unit length):

$$\phi = 1 - \exp\left(-\frac{n_r \pi(\gamma_r^2 + \frac{4}{3}\gamma_r^3)}{L^3}\right), \tag{4.13}$$

where n_r is again the number of rods (Balberg, 1986). Note that because this volume is used to generate the contact network via intersections of the individual spherocylinders—it is not equivalent to the volume fractions measured in the experiments discussed in Ch 1. In the latter case, ϕ only

includes the volume composed of the particles themselves, which is necessarily lower than the effective volume fraction measure considered here.

As in Sec. 3.4, unit length rods (spherocylinders) are placed with uniform position and orientation into a cubic volume of length L. However, boundary conditions are slightly modified to allow for more accurate density measurement. That is, periodic boundary conditions are implemented in all three dimensions (as opposed to the scheme used in two dimensions). All experiments are performed at one aspect ratio $\zeta = 1/(2\gamma_r) = 50$, while domain box size is varied such that $5 \leq L \leq 10$. At each box size, I generate an ensemble of configurations at $\sim 20 - 50$ different volume fractions. The number of configurations per volume fraction and domain size varies between $20 - 100$, depending on L and ϕ. From each configuration, I find the contact network representation using a tree-based search (as in two dimensions), and then implement *3D-RGC*.

In order to explicitly check for the presence of a spanning rigid component within a configuration, I must first define such a component explicitly. First, a spanning component may be defined as in two dimensions. In this definition (I), I consider the upper and lower ends of the simulation box (in one dimension, say the x dimension) to be rigid plates, and define a spanning rigid component as a rigid component containing these two plates. Computationally, checking for this spanning component amounts to connecting each node which touches the lower (upper) x-boundary to a lower (upper) x-boundary node, and then searching for a rigid component containing these two boundary nodes after implementationof *3D-RGC*. In order for this criterion to be nontrivial, rods touching the lower boundary must be dissociated from their periodic duplicates on the right boundary and vice versa. As a simple alternative, I consider a second definition wherein a spanning rigid component simply contains rods which touch both boundaries along the x-dimension (II), and also study the behavior of the relative size of the largest rigid component (III), which could also be used to define a spanning rigid component.

One may be tempted to suppose that any rigid component defined as spanning by (I) is also spanning by (II). However, in many simulations, rigid components are instead identified by (I) and not by (II), as the highly connected boundary nodes tend to template growth of rigid components throughout RGC (see Fig. 4.4). While there are certainly configurations with spanning rigid components by definition (II) but not (I), these were never observed in the simulations of this study (some were found at $L = 1$).

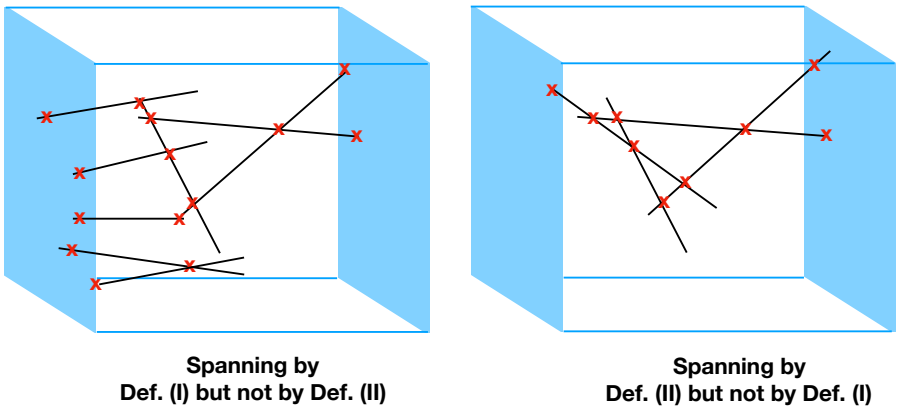

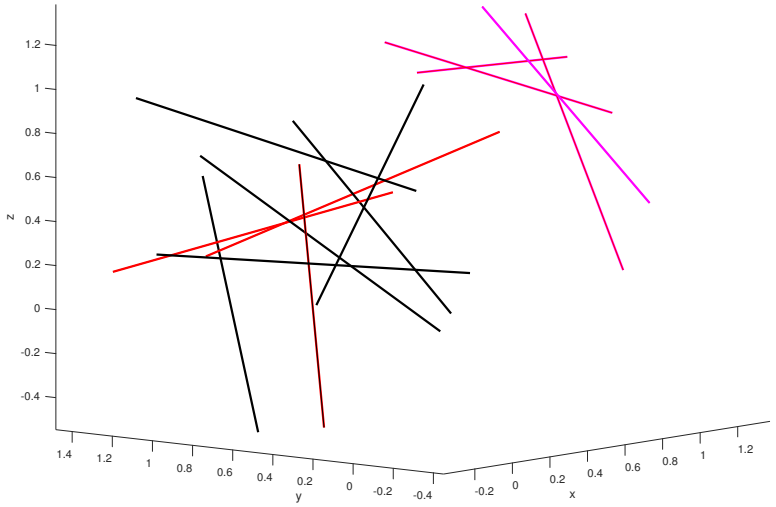

Figure 4.4: **Differing definitions of rigidity percolation.** *Top*: Two rod dispersions contain rigid components that are identified as spanning by either definition (I) or (II) but not both. In the left configuration, the boundaries template growth of the rigid component, which is spanning according to definition (I). Only the triangle of touching rods is identified as rigid if the boundary nodes are not present, and because this triangle intersects only the right boundary, it is not spanning according to (II). In the right, the entire component is rigid without the boundary nodes. Because the component intersects both boundaries, it is rigid according to definition (II). However, if boundary nodes were introduced, this component would be singly connected to each boundary node and thus would not be identified as spanning by (I). The case of the left panel (II but not I) occurs with far greater frequency in simulation (see Fig. 4.6). *Bottom*: If boundary nodes are introduced as in definition (I), *3D-RGC* identifies two components in the initial 3-clique community compression—these are the magenta rods in one component, and both the red and black rods together in one component. The latter component is a 3-clique community only if the boundary node is included—it fragments into the red triangle of rods (one 3-clique community) and assorted rods if the corresponding boundary node is not included. Consequentially, this configuration (including ~ 90 rods excluded from this depiction for clarity) is identified as having a spanning rigid component according to definition (I) but not (II) after full implementation of *3D-RGC*.

4.4 Results

Interestingly, results indicate that at finite L, $\pi_I(\phi, L) \geq \pi_{II}(\phi, L)$ for all ϕ (with the bound being proper for $\phi \leq \phi_{min,II}$), and that the largest rigid component becomes giant alongside the formation of a spanning rigid component according to II (see Fig. 4.5). However, the finite-size scaling analysis to follow seems to indicate that the three rigidity percolation thresholds may be equal (i.e. $\phi_{min,I} = \phi_{min,II} = \phi_{min,III} \doteq \phi_{min}$), though more samples are needed to show this unequivocally.

I conduct finite size scaling analyses to find the rigidity percolation thresholds (I and II) and associated correlation parameters using exactly the same procedure as that used in the previous chapter, assuming here that $\phi(\phi, L) = \Pi([\phi - \phi_{min}]L^{1/\nu})$, for some function Π and the rigidity percolation threshold ϕ_{min} (according to either of the definitions). For each domain size L, I fit a cumulative logistic distribution to the set of values $\pi_{II}(\phi, L)$ and estimate $\Delta\phi_{min}(L)$, the variance of the rigidity percolation window in terms of volume fraction, as well as $\phi_x(L)$, the probability distribution defined by $\pi_{II}(\phi_x(L), L) = x$ for $x = 0.2, 0.4, 0.6, 0.85$ (see Fig. 4.6). Using these fits, I determine ν by fitting a relationship between $\Delta\phi_{min}$ and $\log L$ according to the scaling relation of Eq. 3.15. I attain that $\nu_I \doteq 0.728$ with 95% confidence intervals of $(0.223, 2.04)$; and that $\nu_{II} \doteq 0.978$ with 95% confidence intervals of $(0.745, 1.29)$. Then, I use Eq. 3.16 to find that $\phi_{min,I} \doteq 0.0604$ with 95% confidence intervals of $(0.0603, 0.0607)$; and that $\phi_{min,II} \doteq 0.0603$ with 95% confidence intervals of $(0.0600, 0.0607)$. Large confidence intervals suggest certain points are undersampled. For simplicity, I omit a finite size scaling analysis of π_{III} in this study.

As noted in Sec. 4.3, the results of *3D-RGC* are subject to the ordering of motif compression. In order to determine the significance of this somewhat unfortunate observation, I conduct rigidity analyses on the same configurations using repeated implementations of *3D-RGC* (with randomized motif compression orderings). Implementing *3D-RGC* five times upon the same 10 configurations for all 46 different volume fractions at $L = 6$, I find no instances in which *3D-RGC* finds differing results according to I or II based on compression. In three of these 460 total runs, the size of the largest component varies slightly, with differences no greater than 0.02 (relative to the number of rods in the configuration).

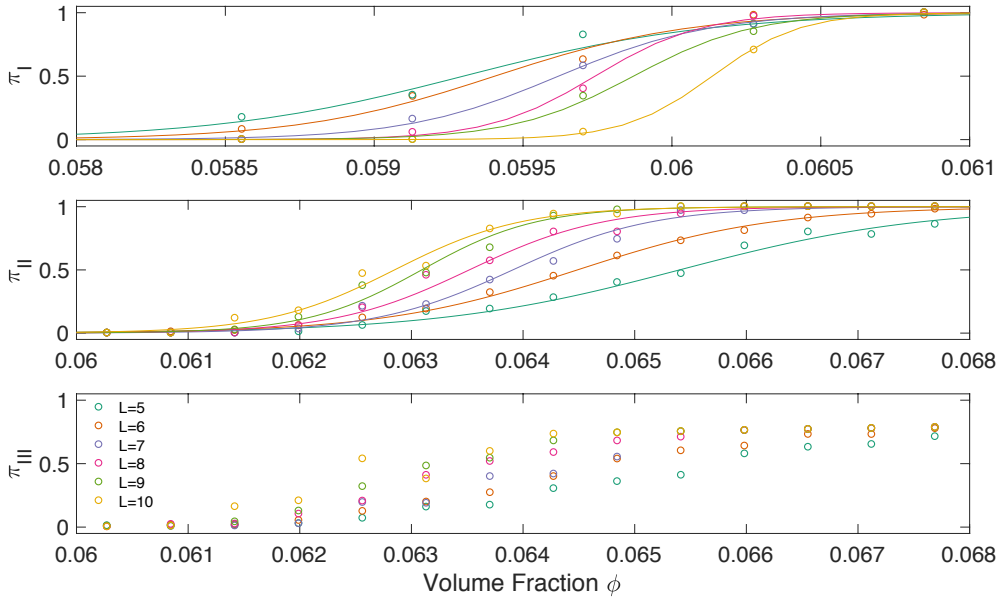

Figure 4.5: **Rigidity Percolation as Measured by Three Definitions.** While the rigidity percolation threshold corresponding to definition I is be lower than that corresponding to II for any finite L, these thresholds seem to converge as $L \to \infty$ (see Fig. 4.6). The dependence of the relative size of the largest rigid component on L and ϕ seems to be similar to that of π_{II}.

4.4 A note about computational efficiency

I have largely spared the computational details of motif-finding in this documentation. However, in order to identify any of the motifs of size $n_r > 3$, I rely on the well-known graph-theoretic property that the number of paths of length k between two nodes i and j is given by A^k_{ij}, the i, j entry of the kth power of the adjacency matrix, A. In particular, identification of *Motif 3D4A* involves finding instances in which two adjacent nodes are connected (in addition to the edge between them) by two paths of length 2. (Further checks on 'rods_in_node' and on whether the involved edges are rod-sharing are also performed in accordance with the motif's hypotheses.) As well, identification of instances of Motif *3D2A* and *3D2B* involve construction of the (weighted) adjacency matrix, and querying for entries of appropriate size. Identification of these motifs at any stage thus involves forming a contact graph's (weighted) adjacency matrix, (sparse) matrix multiplication, and finding certain entries in the resulting matrix. These operations are rather slow in Python's NetworkX library (Hagberg et al., 2008), presumably because it stores graphs using edgelists rather than with sparse matrices. Indeed, I find that identification of instances of *Motif 3D4A* can be as much as 40 times

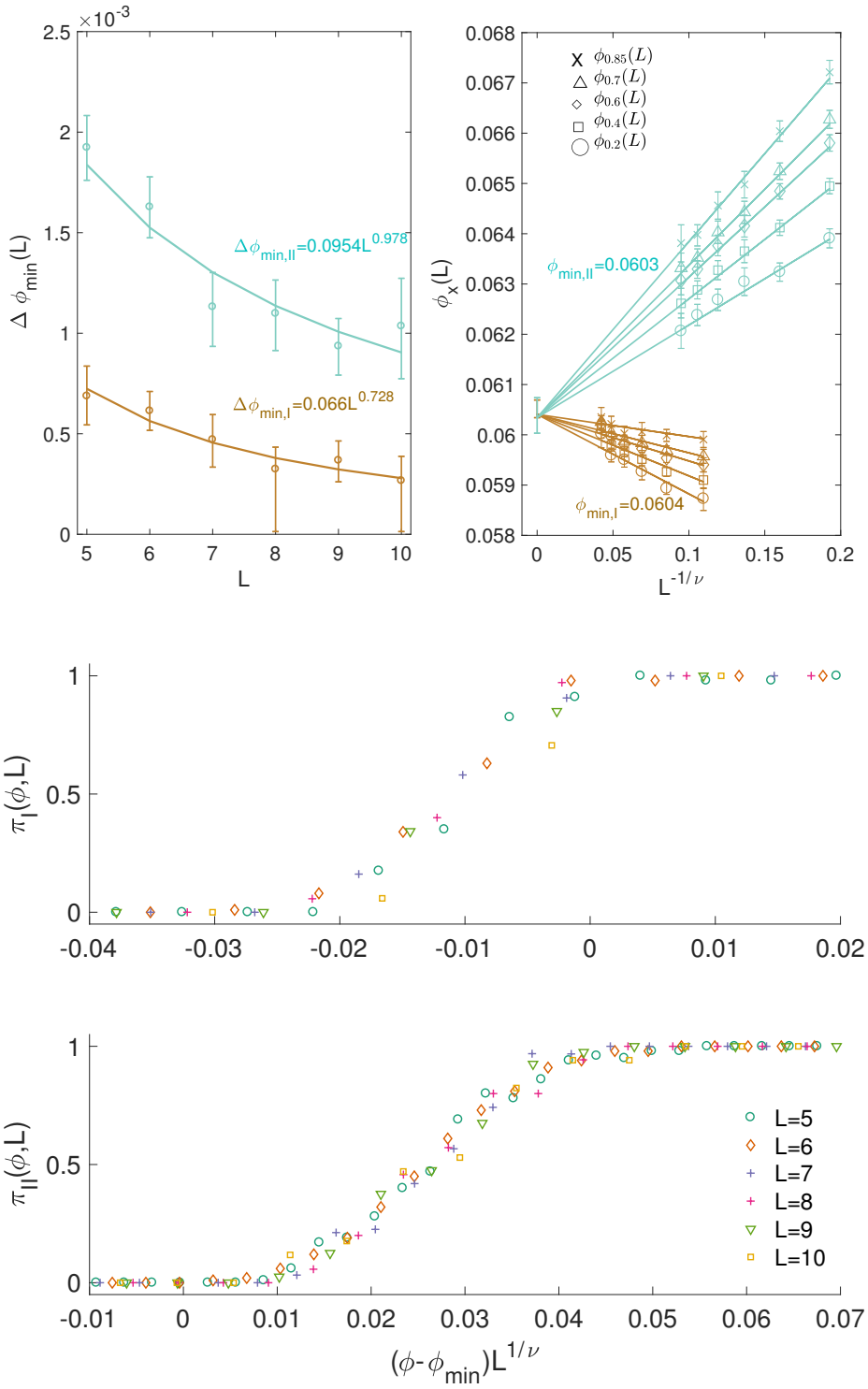

Figure 4.6: **Finite-size scaling analysis (top) and data collapse (bottom) for rigidity percolation as measured by (I) and (II).** Using the standard scaling analysis of Stauffer and Aharony (1992), I find that $\pi_I(L) = \Pi_I([\phi - 0.0604]L^{1/0.728})$ and that $\pi_{II}(L) = \Pi_{II}([\phi - 0.0603]L^{1/0.978})$.

faster in MATLAB than in NetworkX for networks generated from dispersions of size $L = 9$. It may be worthwhile to rewrite this code in a more amenable language for future study at larger domain sizes (keeping in mind that some functionality in Networkx, for example the use of multi-graphs, will perhaps be lost). As shown in Fig. 4.7, the computational time of the current implementation scales as $L^{7.9}$ or $V^{2.6}$ (though the accompanying constant is rather low)—this implementation also requires significant memory allocation.

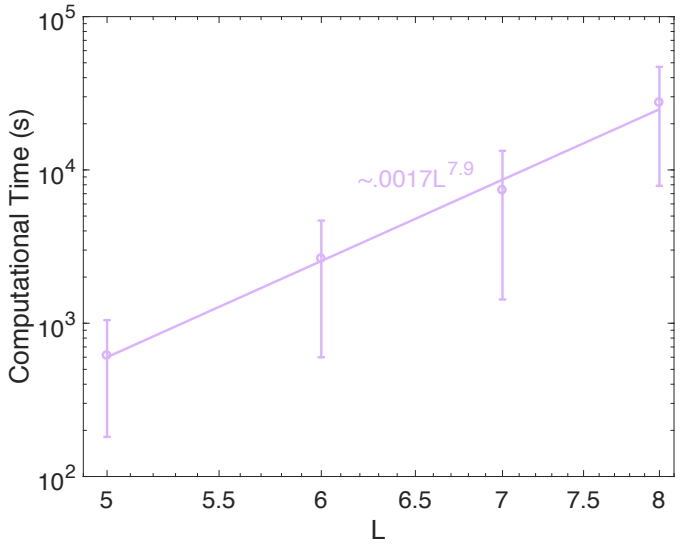

Figure 4.7: **Scaling of *3D-RGC* as currently implemented.** Computational efficiency could surely improved, but the current implementation is sufficient for deducing the rigidity percolation threshold at the studied aspect ratio.

4.5 Accuracy of the rigidity percolation threshold estimation

The previous section attains an upper bound for the rigidity percolation threshold of disordered 3D fiber systems (with uniformly random position and orientation). However, none of this analysis is sufficient to determine how close this bound is to the actual rigidity percolation threshold. With further effort, it would be easy but tedious to identify and prove more rigid motifs in this 3D system. However, the more important task is to determine some measure of accuracy. Here, I outline some methods for demonstrating the convergence of *3D-RGC*'s ϕ_{min} estimation to the true threshold.

First, I construct graphlets of size up to $n_r = x$ for $x \leq 7$, and—interpreting these graphlets as rod contact networks—I classify them as either rigid or not (as in Sec. 3.5). However, this is less powerful here, owing to the difference of scales between rods and non-linear rigid components:

showing that *3D-RGC* exactly characterizes the rigidity of components containing up to x individual rigid bodies is more ambitious than stating it does so for components containing up to x rods. Nonetheless, I am able to identify candidate rigid motifs—composed of single rods or of other rigid bodies—using this approach. Along with implementing *3D-RGC*, I compute whether or not the graph satisfies the global Maxwell counting rigidity condition as applied to 3D fiber systems with hinge-like contacts (Connelly et al., 2009):

$$5|V| - 6 - 3|E| \leq 0, \tag{4.14}$$

where $|V|$ is the number of nodes (rods) in the graphlet and $|E|$ is the number of edges (contacts). I also classify which graphlets are contained within their 2-cores. As both of these conditions are necessary but not sufficient conditions for rigidity, I use these to identify candidate rigid motifs, finding that *3D-RGC* identifies all candidates for $n_r \leq 5$. Nine graphlets of size $|V| = 6$ are identified as rigid candidates via the 2-core/Maxwell condition (see Fig. 4.8). While 57 graphlets of size $|V| = 7$ are identified as rigid candidates, all but 24 of these contain one of the nine $|V| = 6$ graphlets as subgraphs. Furthermore, among the nine $|V| = 6$ candidates, I identify only two of these as rigid (by computing their corresponding rigidity matrices—such analysis is excluded here). Future work involves distinguishing which $|V| = 7$ candidates are truly rigid ('true positives') from those which are not ('false positives'), and furthermore exploring whether this analysis can recover any motifs that act on larger rigid bodies, rather than solely on rods.

Ideally, it would be useful to develop a method (in addition to *3D-RGC*) which exactly characterizes rigidity percolation for small dispersions. A candidate for this method is the spring-based optimization routine discussed in Sec. 2.2.4. However, this method suffers from considerable numerical instability in three dimensions. Notably, in analysis of small $L < 2$ systems, I find no cases in which the spring-based method identifies a larger rigid component than does *3D-RGC* (yet many in which this method does not identify the largest rigid component, due to this aforementioned instability).

Given the instability of applying a spring-based method to this system, the most hopeful determination of accuracy for *3D-RGC* probably lies in use of the graphlet-based analysis described above. Having determined the accuracy of *3D-RGC-x* up to some number of components x, I can reasonably

claim that if the difference between the rigidity percolation thresholds as found via *3D-RGC-(x-1)*,..., approach that of *3D-RGC-x*, then the number of motifs incorporated into *3D-RGC-x* is likely sufficient (begging a very informal comparison to Cauchy convergence). The closeness of the rigidity percolation thresholds attained by *2D-RGC-3* and *2D-RGC-5* motivates this approach.

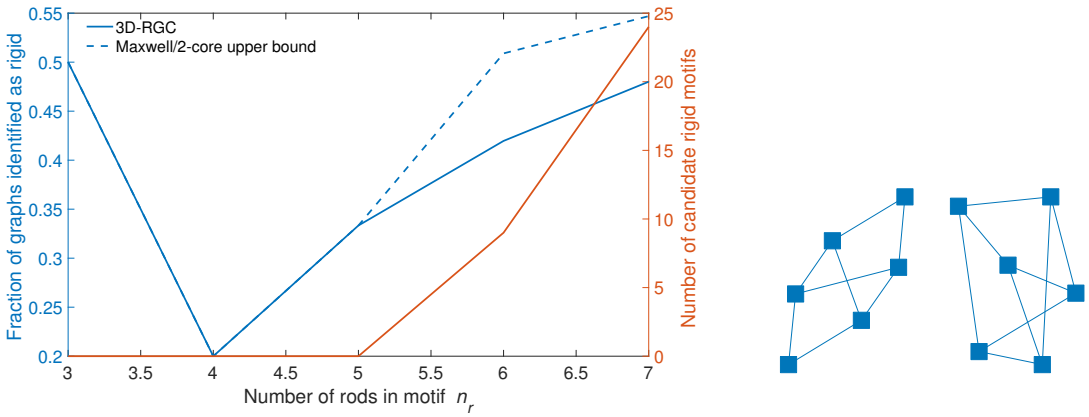

Figure 4.8: **Graphlet-based analysis of the accuracy of *3D-RGCLeft***: The sufficient but necessary algorithm *3D-RGC* identifies as rigid all those graphlets containing at most 5 vertices (i.e. $n_r \leq 5$), which both satisfy the Maxwell counting condition (Eq. 4.14) and the requirement that a rigid graph is contained in its 2-core. These latter two conditions are necessary but not sufficient for rigidity—9 graphlets of size $|V| = 6$ (signifying $n_r = 6$) and 57 of size $|V| = 7$ meet these latter conditions but are not classified as rigid by *3D-RGC*. Of these 57, only 24 do not contain one of the former $|V| = 6$ candidate motifs as a subgraph, and thus merit consideration. *Right*: Upon further inspection, two of the $|V| = 6$ graphlets are rigid when viewed as rod contact networks—the other seven satisfy 4.14 and are contained in their 2-cores but are nonetheless floppy.

4.6 Maxwell prediction

As noted in Sec. 2.2.1, the Maxwell prediction of the rigidity percolation threshold is quite low relative to the true threshold in two dimensional fiber networks. In three dimensions, a similar derivation reveals that Maxwell counting in three dimensions predicts that the rigidity percolation threshold occurs when the average number of contacts per rod or mean contact number $\frac{2N_c}{n_r}$ reaches $10/3$. Previously, it has been derived that for long rods (such that $L >> \gamma_r$), the mean contact number scales approximately linearly with volume fraction (Philipse, 1996):

$$< 2N_c/n_r >= \phi \frac{L}{2\gamma_r} \left[8\frac{L}{\gamma_r} + \frac{3L/(2\gamma_r)}{3L/(2\gamma_r) + 2} \right]. \tag{4.15}$$

Setting this equation equal to $10/3$ gives $\phi_{min} = 0.0637$, an unexpected *overprediction* of ϕ_{min}. I offer two explanations for this effect. First, the random contact equation seems to slightly overpredict

N_c in the simulated dispersions (see Fig. 4.9). Second, in many studies it is common to first remove any unbonded particles from the system before applying the Maxwell count (Huisman and Lubensky, 2011). As there is no analytical expression for the number of contacts with degree ≥ 1, I simply plot the rigidity percolation probability $\pi_{II}(\phi, L)$ against ϕ (Fig. 4.9) and find that the threshold is apparently very close to $10/3$ (more analysis should be undertaken to give an explicit prediction). Given that a spanning rigid component must be contained in the two-core, I also plot this percolation probability against the within-2-core mean contact number. This latter calculation suggests that the critical contact number within the 2-core is greater than $10/3$, which shows that there are still many redundant contacts at the onset of rigidity percolation (though certainly less than was the case in two dimensions).

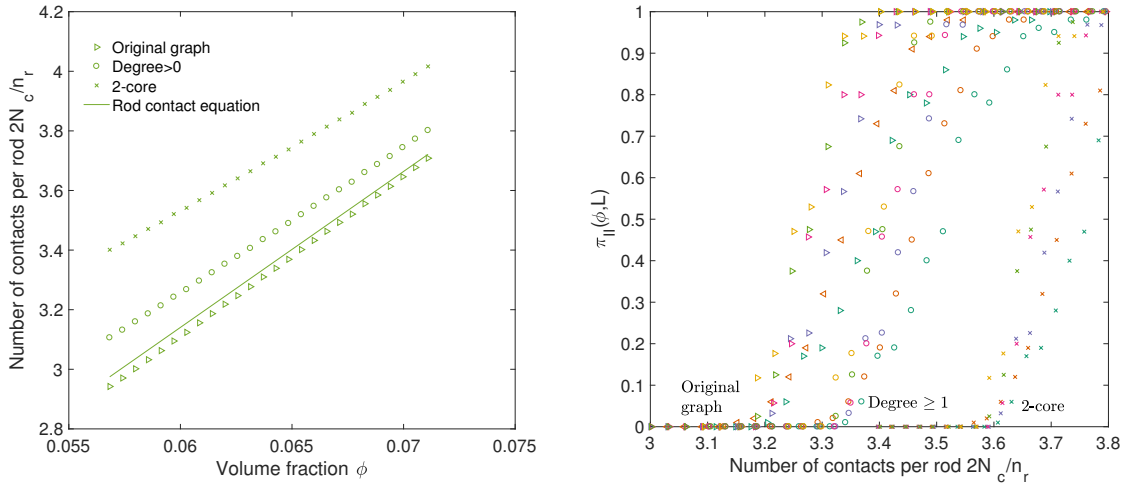

Figure 4.9: **Comparison of Maxwell prediction with observed rigidity percolation threshold.** *Left*: The rod contact equation seems to slightly overpredict the mean number of contacts per rod in these simulations (only one box size is used in this graphic, but symbols overlap completely when the six sizes are included). This overprediction may be either the result of some slight approximations used in the employment of periodic boundary conditions, or of correlations between contacts not considered in the equation's derivation. *Right*: Curiously, the Maxwell prediction $2N_c/n_r = 10/3$ seems to be quite accurate only when the degree zero nodes are not included in this calculation. Information from all six box sizes is used in this box (with colors corresponding to those of Fig. 4.5).

CHAPTER 5: CHARACTERIZATION OF NANOCOMPOSITES WITH INTERFACIAL CRYSTALLINE GROWTH

> I beheld the wretch—the miserable monster whom I had created. He held up the curtain of the bed; and his eyes, if eyes they may be called, were fixed on me. His jaws opened, and he muttered some inarticulate sounds, while a grin wrinkled his cheeks. He might have spoken, but I did not hear; one hand was stretched out, seemingly to detain me, but I escaped and rushed downstairs. I took refuge in the courtyard belonging to the house which I inhabited, where I remained during the rest of the night, walking up and down in the greatest agitation, listening attentively, catching and fearing each sound as if it were to announce the approach of the demoniacal corpse to which I had so miserably given life. $\sim$ Victor Frankenstein

5.1 Overview

At this point of the dissertation, I turn from an abstract perspective on nanocomposites' mechanical properties towards study of real materials and laboratory data. In particular, I use two different approaches to characterize the geometry of the nanocomposite of interest; and then use network analysis of simulated rod dispersions (as in the rest of this dissertation), in order to assess the nanocomposite's mechanical properties.

The system I consider in this chapter is rather complex—rather than being a two-phase nanocomposite in which nanoparticles are dispersed in polymer, this nanocomposite contains a third phase formed by polymer crystallizing around nanoparticles. Precise details are available in associated experimental publications (Hegde et al., 2013, 2014, 2015; Hegde, 2014), but I will briefly describe the system in the following subsection.

5.1 Description of experimental system

In the experiments of interest, a nanocomposite with promising thermomechanical properties is synthesized in two main steps. First, single-walled carbon nanotubes (SWCNTs) are dispersed by probe sonification in solvent (N-Methyl-2-pyrrolidone, or NMP) until absorbance values plateau (indicating maximum exfoliation), at which point the mixture is subjected to three more hours of sonification under a bath. The relatively linear poly-imide (PEI) ODPA-P3 (see Fig. 5.1) is then stirred into this intermediate, which undergoes *in-situ* polymerization for 24 hours. In the second step,

the nanocomposite is subjected to film casting, vacuum drying, and thermal imidization according to established protocols for preparation of the final ODPA-P3 SWCNT nanocomposite film.

This carefully prepared nanocomposite is notable for containing highly ordered interface around dispersed SWCNTs, as observed via X-ray diffraction and transmission electron microscopy (while their having only one wall may be important, SWCNTs are from this point forward simply referred to as CNTs). Indeed, this is the only studied composite in which the host polymer depends on the CNTs for crystallization. Other polymers have been observed to crystallize around CNTs, but such polymers do not *require* CNTs for nucleation as does ODPA-P3. As a result, the nanocomposite has impressive mechanical properties that persist over a wide temperature range. Specifically, property measurements indicate that nanocomposites containing CNT volume fractions $0.001,\ 0.003,\ 0.006$, and 0.012 have broad industrial appeal. Experimentalists have synthesized higher loadings as well, but the resulting composites are brittle and lack the desirable properties of these sparser nanocomposites.

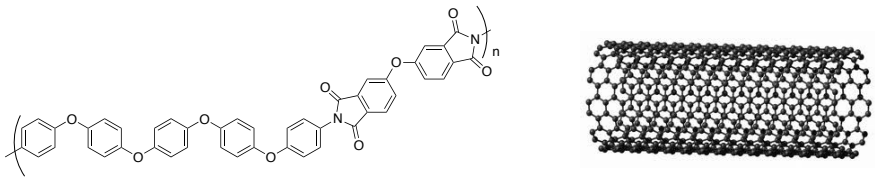

Figure 5.1: **Favorable interactions between the polyimide and CNTs give rise to a third phase of crystal coating.** The principal ingredients of the nanocomposite of interest are the amorphous polyetherimide 3,3',4,4'-oxdiphthalic dianhydride (ODPA-P3), shown left—and single walled carbon nanotubes (SWCNTs), shown right.

5.1 Modeling goals

The goal of this modeling is to better understand the microstructural mechanism responsible for the ODPA-P3/CNT nanocomposite's measured high performance properties, and to guide future experimentation. This latter goal may be broken into parameter optimization (i.e. pinpointing the highest promise CNT volume fraction), and qualitative analysis (i.e. understanding the property implications of improving dispersion quality). Whereas experimentalists have extensively characterized the nanocomposite's mechanical and thermomechanical properties, each of which is of interest to potential applications, this study will focus on just a few specific, temperature-fixed material properties (italicized below). The rest of this chapter is organized as follows.

First, in Sec. 5.2, I use a statistical/probabilistic modeling approach to relate the observed *crystallinity* to the input volume fraction of CNTs, and furthermore use these results to predict *elastic modulus* using well-established homogenization techniques (elastic modulus measures the material's elasticity, and is equal to the stress/strain ratio at low deformations). Then, in Sec. 5.3, I further explore the relationship between CNT volume fraction and crystallinity by developing a simple discrete characterization scheme for CNT dispersions of varying spatial distribution. In Sec. 5.4, I consider the network properties of homogeneous and heterogeneous CNT dispersions, and explore a network-based hypothesis which accounts for observed stress-strain measurements. While there doesn't seem to be a clear relationship between the CNT concentration and tensile stress, the material has the most desirable stress-strain behavior at the lowest CNT concentration studied (volume fraction 0.001). This can be seen by measurements of *% elongation at break* and *toughness* (area under the stress-strain curve) for the different CNT loadings.

5.2 Geometric characterization of CNT-facilitated crystallinity

In this section, I attend to purely geometric considerations in studying crystalline growth around dispersed CNTs. The central assumption of this chapter is that crystal grows radially up to some thickness γ_{max} around the nucleating CNTs (of radius γ_c), but this growth is impeded by the condition that crystalline layers from two or more CNTs cannot occupy the same space. While this latter condition is a truism, the assumption represents an admittedly very simple picture of semicrystalline composites—the inherent physics are much more complicated, and it would be useful to reconcile the results of this analysis with a more physics-based modeling effort of the crystallization, but such work is beyond the scope of this study. Nonetheless, I suspect this assumption is sufficient for understanding global properties—it is consistent with the tendency of semicrystalline nanocomposites' inclusions to efficiently promote crystallization at low volume fractions and for this efficiency to taper with increasing volume fraction (Laird and Li, 2013).

5.2 Probabilistic modeling

If no crystalline layers overlap, and each grows uniformly to some thickness γ_{max}, it is quite simple to relate crystallinity V_{crys} to γ_{max} and ϕ_c (the volume fraction of CNTs with non-varying radii γ_c and length ℓ):

$$V_{crys} = \phi_c \left[\left(\frac{\gamma_{max} + \gamma_c}{\gamma_c} \right)^2 - 1 \right], \tag{5.1}$$

under the assumption that $\ell \gg \gamma_c$. In real materials, ℓ and γ_c may be distributions rather than constants, and this equation—which I refer to as the *unimpeded growth model*—may be modified to account for this using a probabilistic argument (in this entire dissertation, I assume this effect is not greatly significant and that CNTs as well as their associated crystalline layers may be treated as monodisperse). One can then measure crystallinity for dispersions of different CNT volume fraction, and use the linear dependence of Eq. 5.1 on ϕ_c to estimate γ_{max} (Coleman et al., 2004; Hegde et al., 2013). Here, I use the condition that two cylinders cannot occupy the same space to modify Eq. 5.1—this basically amounts to Balberg's formula (used in Eq. 4.13). Whereas I previously used this formula to account for the effect of nonsequential rod packing on rod volume fraction, the formula derives from a probabilistic argument used to determine the total expected surface-enclosed volume ($V_{crys} + \phi_c$ here) in a random packing of fully penetrable surfaces with uniform shape as well as uniformly random position and orientation (Balberg, 1986). The stated condition above assumes that the crystalline layers are instead impenetrable, in that one crystalline layer cannot occupy another's excluded volume. However, as would-be multiply-occupied volumes do not contribute to V_{crys}, this problem is essentially equivalent to Balberg's. In this scenario, the bare CNTs ought be sequentially packed prior to crystalline growth, but I assume this effect is small as $V_{crys} \gg \phi_c$ in all of the experimental measurements. Hence, using measured values of V_{crys} and ϕ_c, I am able to estimate γ_{max} by fitting this data to a slight modification of Balberg's equation, which I refer to as the *homogeneous geometric model*:

$$V_{crys} = 1 - \exp\left[-\phi_c \left(\frac{\gamma_{max} + \gamma_c}{\gamma_c}\right)^2\right] - \phi_c. \tag{5.2}$$

While this equation presents a more sophisticated geometric model than does Eq. 5.1, it is still quite crude. In particular, this model assumes that the CNTs are both uniformly dispersed and isotropically oriented. In real nanocomposites, dispersions are imperfect and optical microscopy images illustrate a very spatially heterogeneous distribution of CNTs (Fig. 5.2).

As a first approach, I modify the homogeneous geometric model of Eq. 5.2 to reflect the hypothesis that CNTs are clustered entirely within a fractional volume $v_c = f(\phi_c)$ of the material's

domain (the *confinement model*):

$$V_{crys} = v_c \left\{ 1 - \exp\left[-\frac{\phi_c}{v_c} \left(\frac{\gamma_{max} + \gamma_c}{\gamma_c} \right)^2 \right] \right\} - \phi_c \; ; \tag{5.3}$$

$$v_c = k\phi_c, \tag{5.4}$$

for some constant k. Furthermore, the second equation constrains this fractional volume $v_c(\phi_c)$ to scale linearly with ϕ_c. Therefore, the local concentration of CNTs (ϕ_c/v_c) within the occupied volume is set as a constant for all ϕ_c (clearly, $v_c \in (0, 1]$). While I note that my study is certainly not the first to consider the implications of CNT aggregation in polymer nanocomposites (see e.g. Ma et al. 2017), such effects have perhaps not received due theoretical attention. Spatial heterogeneity in this class of materials is difficult to model, but an understanding of its effect would undoubtedly be very useful to guiding future experimentation.

In order to inverse predict γ_{max} (and v_c for the confinement model), each of these simple crystalline growth models is fit to experimental crystallinity results using a standard least squares optimization routine (these crystallinity measurements are obtained via the standard wide angle X-ray scattering protocol, as noted in any of the previously cited *Hegde* references). The predicted crystalline radius increases with model complexity ($\gamma_{max} = 2.5,\ 3.0,\ 3.5$ nm for the unimpeded growth, homogeneous geometric, and confinement models, respectively), as seen in Figure 5.3–left. Unsurprisingly, the two parameter confinement model (with selected local concentration $\phi_c/v_c = 0.0175$) prediction gives the lowest residual sum of squares. Generally, more than four points ought be used for training of any model—however, the confinement model seems to fit the data reasonably well. The point corresponding to the lowest CNT loading has the highest residual for each model. As noted in Sec. 5.4, the behavior of this nanocomposite seems to have different properties than the other three, and it may be inappropriate to assume it follows the same crystalline growth model.

Finally, I use these crystalline growth models to predict the bulk Young's modulus E_{bulk} as a function of γ_{max} for the four composites of varied CNT loadings, using the random fiber Halpin Tsai

equation (Affdl and Kardos, 1976; Coleman et al., 2005):

$$E_{bulk} = \left[\frac{3}{8}\left(\frac{1+\zeta\eta_L(V_{crys}+\phi_c)}{1-\eta_L(V_{crys}+\phi_c)}\right)+\frac{5}{8}\left(\frac{1+2\eta_T(V_{crys}+\phi_c)}{1-\eta_T(V_{crys}+\phi_c)}\right)\right]E_m \tag{5.5}$$

$$\eta_L = \frac{E_{comp}/E_m - 1}{E_{comp}/E_m + \zeta} \qquad \eta_T = \frac{E_{comp}/E_m - 1}{E_{comp}/E_m + 2}, \tag{5.6}$$

where $\zeta = \ell_n/\gamma_c = 2000$ is the CNT aspect ratio, $E_m = 2.6\ GPa$ is the experimentally measured Young's modulus of the pure PEI, and $E_{comp} = 10.4\ GPa$ is the Young's modulus of the CNT-containing PEI crystal complexes (Hegde, 2014). This two-body modulus prediction seems to perform reasonably well in comparison to experimental measurements of Hegde et al. (2013) (see Fig. 5.3–right). However, as above, the prediction at the lowest CNT loading seems to be less accurate than those of the other loadings.

The differences between each of the three crystalline growth models at any given CNT loading has an interesting materials engineering interpretation. Under the assumption that CNT agglomeration and spatial crowding of crystalline layers are the limiting factors to crystallinity, the gap between the prediction of the homogenous growth model and that of the confinement model (in Fig. 5.3) represents the maximum possible gain in crystallinity and elasticity, were the CNTs to be uniformly dispersed. While each of these models are quite crude, such maximum possible gains might be considered in future experiments when weighing the consideration of dispersion quality.

5.3 Discretized geometric characterization

The models of the previous section apply probabilistic methods to the task of predicting crystallinity from radial crystalline growth (or the inverse problem). In this section, a different, discretized approach is used to predict crystallinity from radial growth in any given simulated CNT dispersion. While it will be shown that the homogeneous geometric model considered above agrees very strongly with the discretized method considered here (for uniformly random CNT dispersions), this latter method has some advantages for future applications, in that it may be modified for different, and perhaps more accurate CNT dispersion models than that considered in the confinement model. Furthermore, it may be used to approximate to any desired accuracy the exact locations of crystalline layer in a simulated dispersion (which could be used for a finite element or other discretized approach in related modeling, should that be desired).

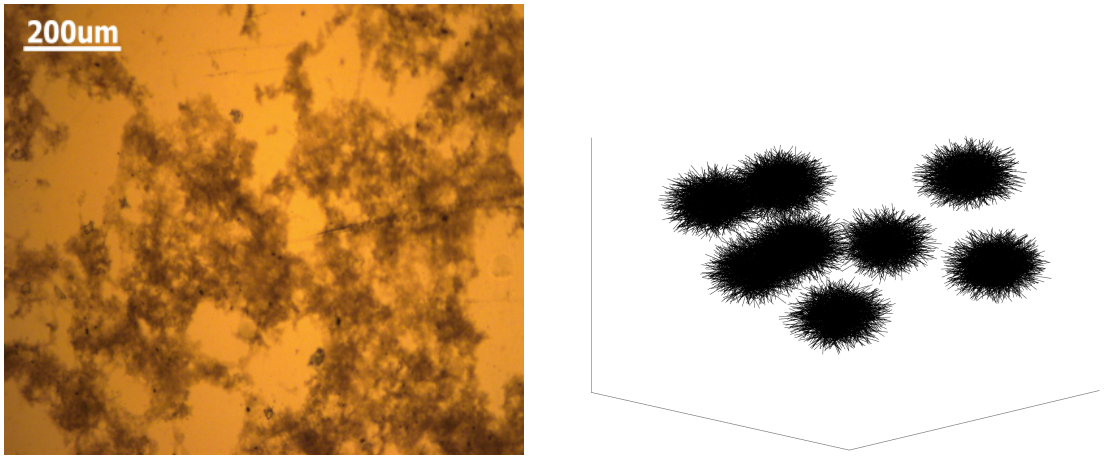

Figure 5.2: **Observed CNT agglomeration guides simulation-based study.** *Left*: On account of Van der Waals attractions, chemical bonds, and impurities, CNTs tend to agglomerate—while sonication and other procedures are frequently used to disaggregate them, it is highly difficult to attain a dispersion that can be considered anything close to uniform. The film shown in this optical microscopy image corresponds to the study introduced in Sec. 5.1.1 and discussed throughout this chapter. Here, PEI is shown to crystallize around CNTs of concentration $\phi_c = 0.001$ (Figure adapted from Hegde et al. 2013). *Right*: In order to mimic the CNT/crystal distribution observed in microscopy, a simple spatial model (the *Matérn* process of Sec. 5.3.1) is used to generate clustered rod dispersions.

Given any dispersion of rods in a cubic domain of size L^3, it is simple but tedious to determine the entire volume that is within some radius $\gamma_{max} + \gamma_c$ of the rods' central axes. There are two approaches for this type of brute force calculation. One could find the volume within $\gamma_{max} + \gamma_c$ distance of any rod's central axis, checking for overlapping regions simultaneously and discounting these. In a dilute dispersion, this might be the most efficient solution. However, in denser packings, a less rod-centered approach is perhaps more sensible. The basic approach of this method is to divide the space into cubic voxels, and identify all voxels which fall within $\gamma_{max} + \gamma_c$ distance of any rod's central axis. While the computational expense of this method necessarily grows cubically with the size of the domain box, the routine may be parallelized immensely.

First, the cubic domain is divided into cubic subdomains of size L_s^3 containing a sufficient but tractable number of voxels of size L_v^3 (as with any parallelization, there is a tradeoff between the number of cores/CPUs used and computational time per CPU). Then within each cubic subdomain, a procedure (commonly used in video game design) is used to check which rods (line segments) intersect the cube, and then to determine the rod endpoints which are local to the subdomain. If a rod has an endpoint in a cubic subdomain, then this endpoint is a local (and global) endpoint; if not, the

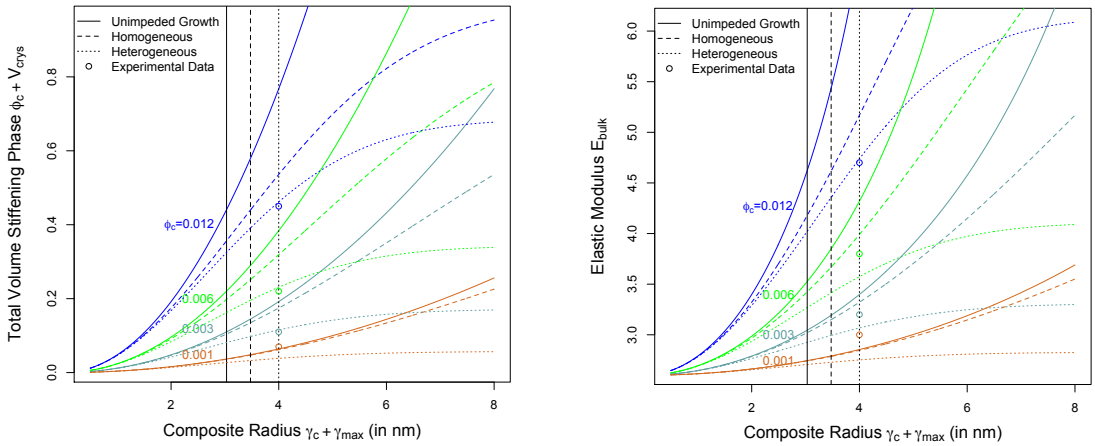

Figure 5.3: **Statistical fitting results for various models of crystalline growth about CNTs.** *Left*: Three simple models (indicated by line style) are used to predict total crystallinity for four different CNT loadings (indicated by color) as a function of maximum radial crystalline growth γ_{max}. For each value of ϕ_c and γ_{max}, there is an obvious ordering of V_{crys} predictions (the unimpeded growth model predicts the greatest crystallinity followed by the homogenous geometric model and then by the heterogeneous crystalline model). Experimental measurements of crystallinity (Hegde et al., 2013) as a function of ϕ_c are fit using each model to inverse predict γ_{max}—the predictions of the three models are $\gamma_c + \gamma_{max} \doteq 3.0, 3.5, 4.0$ nm for each of the respective models, as indicated by vertical lines. *Right*: The simple models are here used to predict Young's modulus as a function of radial crystalline growth for the four different CNT loadings considered experimentally. No fitting of the displayed experimental data is undertaken. Rather, the vertical lines correspond to the inverse predictions of γ_{max} given in the left figure.

local endpoint is its intersection with the surface of the cubic subdomain. Then, all of the rods within the subdomain are discretized into a point cloud and a K-dimensional tree (or *KD-tree*) is formed to cluster the spatial locations within this point cloud efficiently. In the rod discretization step, a rod's central axis is discretized into n_ℓ evenly spaced points. Then, the $(L_s/L_v)^3$ voxels' centroids in the subdomain are treated as a second point cloud, and a large calculation is performed to determine which of these points are within $\gamma_{max} + \gamma_c$ distance from any of the points of the subdomain's rod point cloud. This latter procedure is implemented for all subdomains to find the positions of all crystalline/CNT-occupied voxels, the number of which can be simply divided by the total number of voxels in the domain $(= L/L_v)^3$ to attain the fraction of space occupied by both CNTs and crystal $(V_{crys} + \phi_c)$.

Both n_ℓ and L_v are parameters which control the accuracy of the total calculation. In particular, as n_ℓ becomes large, these points along the rods' central axes become finely packed together so that any points falling within $\gamma_c + \gamma_{max}$ of the rod point cloud are counted as occupied by crystal or

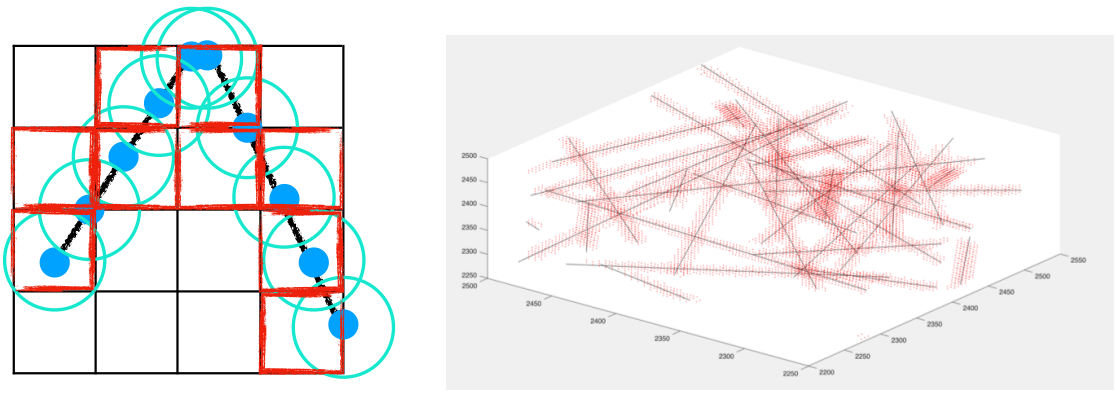

Figure 5.4: **Basic approach of discrete geometric characterization scheme** *Left*: In this 2D schematic of the discretized geometric characterization approach, CNTs (fuzzy) are first discretized into n_ℓ evenly spaced points apiece along their central axes (the local endpoints must also be selected). Then, a KD-tree is used to determine which voxels (squares) have centroids within some radius $\gamma_c + \gamma_{max}$ of the rod point cloud (teal circles represent the coverage of this point cloud). Voxels identified as occupied are here marked as red-bordered squares, while the others have black border. Note that some voxels that are counted vacant may have some volume within the crystal/CNT-occupied regions, while some counted occupied have some volume not within such regions–the fineness of the approximation is controlled by ℓ_n and L_v. *Right*: In this 3D realization, voxels identified as occupied are denoted by red points, which surround their nucleating CNTs.

rod. In the limit $n_\ell \to \infty$, the intersection of balls of radius $\gamma_c + \gamma_{max}$ converge to their containing cylinder. However, as n_ℓ is increased, less points are contained in rod point cloud and the routine becomes faster, but certain regions of the domain that are within $\gamma_c + \gamma_{max}$ distance from the rods are not identified via the procedure (see Fig. 5.4). Calculus can be used to determine the exact fraction A of the enclosing cylinder that is occupied by n_ℓ intersecting balls of some radius γ:

$$\frac{n_\ell(4\pi\gamma^3/3) - (n_\ell - 1)\pi/12(4\gamma + \ell/n_\ell)(2\gamma - \ell/n_\ell)^2}{4\pi\gamma^3/3 + \ell\pi\gamma^2} = A. \tag{5.7}$$

In the experiments discussed below, n_ℓ is chosen such $A \geq .9995$. Lacking theoretical justification for any particular choice of L_v, I show in Fig. 5.5–left that the crystallinity calculation converges as L_v becomes small (I choose $L_v = 2$ nm in the below experiments).

Using the approach described above, I predict the crystallinity as a function of γ_{max} in uniformly distributed CNT dispersions at the four different CNT loadings considered in the modeling of Sec. 5.2.1, as well as two higher density loadings. At each CNT loading, I implement the discrete characterization technique on five sampled CNT dispersions apiece (for a total of 30 samples). Because the main time-intensive step in each run is generation of the KD-trees, it is easy to estimate

V_{crys} using many values of γ_{max}—here, I choose eight. As can be seen in Fig. 5.5–right, the homogeneous geometric model of Sec. 5.2.1 agrees very closely with the results of this discrete approach at every value of γ_{max} and ϕ_c.

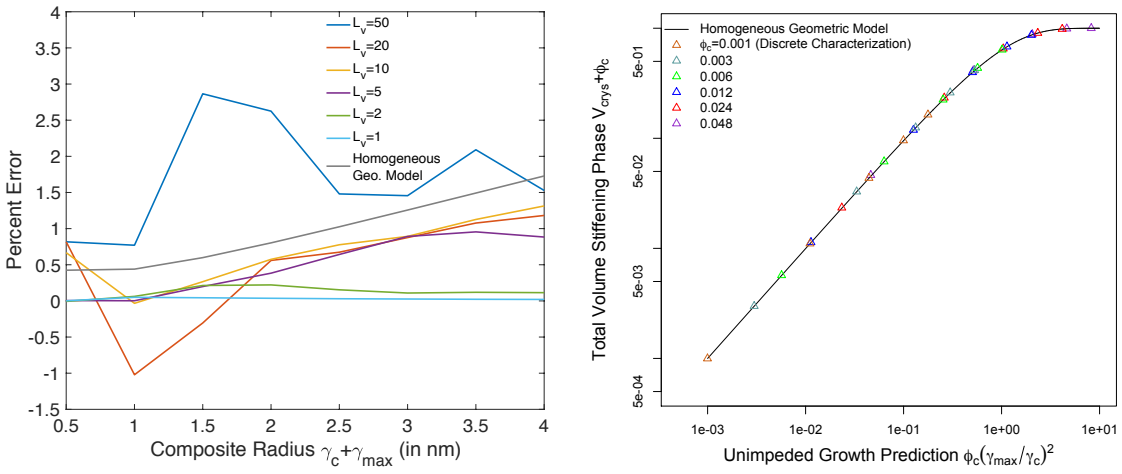

Figure 5.5: **Accuracy of discrete geometric characterization** *Left*: Estimations of crystallinity converge as $L_v \to 0$—treating the calculation with $L_v = 0.5$ nm as ground truth, I calculate the percent error for varying γ_{max} in characterization routines wherein the chosen voxel size varies between 50 and 1 nm. For the rest of the simulations in this study, I balance accuracy and efficiency in choosing $L_v = 2$ nm. *Right*: When implemented on CNT dispersions of uniform position and orientation (with periodic boundary conditions), the discretized geometric approach agrees strongly with the homogeneous geometric model. Error bars are not shown here but standard deviations (across the five different samples per point) are smaller than plot symbols.

5.3 Models for heterogeneous CNT dispersions

In Sec. 5.2, I introduced a very simple statistical model (Eq. 5.4) reflecting observed spatial heterogeneity of CNT/crystal complexes. This model assumes that all stiffening phase ($\phi_c + V_{crys}$) is contained in a fractional volume of the material's domain. This idealization is simple, and whereas it may be sufficient for relating crystalline growth to bulk crystallinity, it cannot fully reflect the complex spatial heterogeneity of the studied nanocomposite. Capturing this spatial heterogeneity is a challenging problem and one of the key challenges in this research direction (which I discuss further in Ch. 6). Here, I consider two very simple *Poisson cluster processes* for computationally simulating heterogeneous dispersions that attempt to mimic the empirically observed CNT aggregation.

There is a slight vocabulary challenge in defining such heterogeneous dispersions. When I have thus far referred to heterogeneous dispersions, I mean that the distribution of rod placement is nonuniform. However, if these rods are to be centered in clusters, the distribution may not be

uniform but still *statistically homogeneous* if these clusters themselves are placed according to a random uniform distribution. A thorough treatment of spatial statistics in materials modeling is given in Torquato (2002). In this dissertation, I equate heterogeneity with nonuniformity, even though this may be undesirable to the heterogeneous materials modeling community.

Poisson cluster processes refer to processes in which $Poisson(\lambda_s L^3)$ 'seed' points are placed at random within a simulation's domain volume (λ_s is called the *intensity* of the point process). Then, a probability distribution is used to determine the placement of the final 'daughter' points (rod centers, in this case) around these seeds. In a *Matérn* process, this latter distribution is uniform, and the $Poisson(\lambda_d)$ daughter points are located within γ_M nm of the seed points. Given $Poisson(\lambda_s)$, λ_d is attained in order to give a predetermined expectation of ϕ_c. In concept, this process is similar to the confinement model, which also considers rods to be uniformly dispersed in a fractional domain—but in the Matérn process, only the CNT centers are confined to this fractional domain. Regions of thickness $\ell/2$ around the seed balls also contain portions of CNT-crystalline volume. Additionally, these clusters may overlap, and so the within-cluster concentration is not necessarily uniform. In a similar model, termed a *Thomas process*, the rod center distribution is a multivariate Gaussian distribution centered at the seed points (with some covariance matrix $\mathbf{\Sigma}$). For a more in-depth study of these clustering processes and others, see Buryachenko (2007).

As I will discuss in Ch. 6, a highly accurate computational rendering of the experimental system likely requires a less restrictive model than the Poisson cluster processes, in addition to a statistical learning algorithm to fit the model to data. Nonetheless, I can illustrate the effect of agglomeration on crystallinity using the simple models discussed above. In the models of Sec. 5.2, it was relatively easy to derive expectations for the volume of stiffening phase given the probabilistic argument of Balberg. Attaining such an expectation from these cluster process models is far too difficult, and so I use the discrete characterization scheme of the previous subsection to approximate this expectation for $\phi_c = 0.001, 0.003$ and varying γ_{max}. I use the Matérn and Thomas processes to generate these heterogeneous dispersions, varying γ_M as well as $\mathbf{\Sigma}$ accordingly. Specifically, $\mathbf{\Sigma}$ is chosen such that the distribution is symmetric with variance σ^2. In order to heuristically realize the observation that the CNTs' local concentration varies little for samples of different ϕ_c, I let $\lambda_s(\phi_c = 0.003) = 3\lambda_s(\phi_c = 0.001)$. Because the expected overlap between these clusters increases

with the density of clusters, this condition is similar to but not quite equivalent to the relevant condition in the confinement model (that ϕ_c/v is constant).

As can be seen in Fig. 5.6, the results of these heterogeneous dispersions sit between those of the homogeneous and confinement models. Even though these clusters take up a relatively small portion of the domain (especially when λ_s and γ_M/σ are low), given the implemented simulation parameters they are never quite so low as the fitted values of v_c at these volume fractions ($\doteq 0.057, 0.171$ for $\phi_c = 0.001$ and $\phi_c = 0.003$, respectively, as found in Sec. 5.2.1).

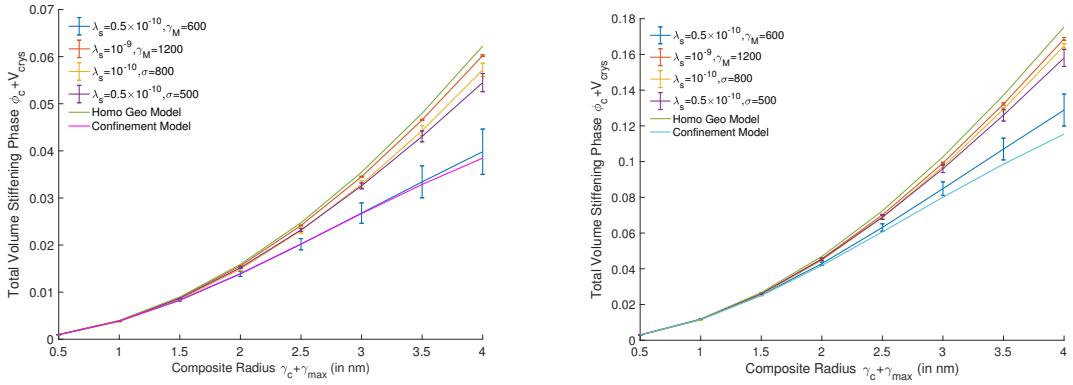

Figure 5.6: **Discrete geometric characterization of heterogeneous CNT dispersions** *Left*: At $\phi_c = 0.001$ (left) and $\phi_c = 0.003$ (right), the dispersion parameters λ_s and γ_M (if the process is Matérn) or σ (Thomas) affects the calculation of crystallinity, as more clustered dispersions are marked by crowding and less efficient growth. For each curve, data points represent averages of five simulations and error bars represent standard deviations.

5.4 Network-based assessments for property characterization

In addition to predicting the composition of the PEI-CNT nanocomposite, simulated reconstructions of the system can be used for inferring network properties of mechanical significance. As noted in the introduction to this dissertation, the impact of a giant rigid component may have different interpretations depending on the nature of the inherent inter-particle interactions as well as of the interactions between nanoparticles and polymer. In particular, interactions between two crystal-CNT complexes in the system of Sec. 5.1.1 may be viewed as grain boundaries between overlapping crystal domains (Hegde et al., 2013). A large part of this dissertation is aimed at supporting the hypothesis that rheological or mechanical percolation occurs with the emergence of a large rigid cluster of interacting CNTs in nanocomposites (see Ch. 1). In such systems, my work implicitly assumes that the dominant contribution to mechanical reinforcement comes from CNT-CNT interactions rather

than from CNT-polymer interactions. The internal stresses generated by crystal-crystal interactions have the opposite effect, and the mechanical reinforcement of this system instead originates from CNT-polymer (crystal) interactions.

The effect of a large rigid component (or even a large connected component) therefore does not have a wholly beneficial interpretation regarding the nanocomposite's bulk mechanical properties. Considering the high experimental measurements of crystallinity, it is hard to envision that these nanocomposites do not possess some regions in which contacting crystalline domains are ubiquitous—yet these composites are nonetheless stable and even have considerable elongation at break. However, being that the composite is composed largely of what has been termed *secondary agglomerates* (Alig et al., 2012), inhomogeneous clusters of CNT-crystal complexes, these internal stresses may be considered as localized.

In particular, an interesting experimental result is the observed advantage in toughness and percent elongation (or strain) at break in the $\phi_c = 0.001$ nanocomposites (Fig. 5.7). Whereas yield strength does not show any clear dependence on CNT volume fraction, toughness and % strain both peak at $\phi_c = 0.001$ and then decline with ϕ_c (when $\phi_c = 0.044$, the resulting nanocomposites are too brittle to handle). Whereas the decline in these mechanical properties at high ϕ_c is expected, no current theoretical model can be used to predict or explain these peaks at low ϕ_c.

This discussion begs the question of what mechanism leads to brittleness and fracture in the semi-crystalline nanocomposite of interest. That is, what network property (if this can be captured as a network property) differentiates stressed yet mechanically strong nanocomposites from brittle materials of no practical use? I tentatively express that a tipping point occurs when the rigid components containing internal stresses merge from secondary agglomerates into one globally rigid component, which has no outlet with which to transmit internal stresses. Because more sophisticated methodology is necessary to mimic the heterogeneity of experimental systems (as suggested in the previous section), it is not in the scope of this work to fully engage this hypothesis. In this analysis, I show (with an eye towards this hypothesis) how network properties are influenced by crystalline growth within both homogeneous CNT dispersions and the simple Matérn process dispersions introduced in Sec. 5.3.1.

5.4 Numerical experiments

In the experiments of this subsection, I study the formation of connected and rigid components in CNT dispersions as crystal grows about the CNTs. That is, I first simulate random bare CNT dispersions (without sequential packing, as in other experiments of this dissertation) and study the rigidity/connectivity of this relatively sparse network. Then, I vary the radius of the crystal-rod complexes according to the results of Sec. 5.2—letting crystalline growth vary ($\gamma_{max} = 0.5, 1.0, 1.5, 2.0, 2.5, 3.0, 3.5$ nm) about the bare CNTs ($\gamma = 0.5\ nm$, $\ell = 1\ \mu m$)—and performing the same analysis for each value of γ_{max}. First, I perform this rigidity analysis upon random homogeneous rod dispersions (uniformly random position and orientation as in the experiments of Ch. 4). The results for this analysis in five simulations at which $\phi_c = 0.001$ and $\phi_c = 0.003$ are displayed in Fig. 5.8–top. Even when the CNTs are relatively sparse, increasing γ_{max} in these homogeneous dispersions facilitates the formation of a giant connected component at $\gamma_{max} \leq 0.5$ nm, and of a giant rigid component at

$gamma_{max} \leq 2.0$ nm in the $\phi_c = 0.001$ dispersions. The bare rods are already connected in the $\phi_c = 0.003$ dispersions, but crystalline growth facilitates the formation of a giant rigid component at $\gamma_{max} \leq 1.0$ nm in these denser packings.

As noted above, agglomeration certainly has an important effect on the composite's network properties. Reliable inference of these properties will ultimately depend on the accuracy of the material reconstruction. Here I demonstrate the effects of crystallinity on network properties in a simple heterogeneous simulation—namely, the Matérn process discussed in Sec. 5.3.1. In this simple heterogeneous model, clusters have dense CNT concentration (while the rest of the volume is sparse) and the number of within-cluster contacts can become very high when $\gamma_{max} > 0$. Because rigid graph compression of such highly connected networks is very time-consuming, I only consider a rather small simulation size ($L = 4$). In order to avoid having a great amount of variance between results at this small box size, rather than setting the density of clusters equal to $Poisson(\lambda_s)$ in these experiments, I simply fix the number of clusters in the domain. At $\phi_c = 0.001$, I set this number to be three, and then set at $\phi_c = 0.003$, I set it to be nine (in accordance with the hypothesis that the local concentration stays approximately constant across the different CNT loadings). I also set the cluster radius to be $\gamma_M = 700$ nm for each dispersion.

Again, analysis is carried out for five dispersions apiece with CNT concentrations $\phi_c = 0.001$ and 0.003, and varying crystalline radius $\gamma_{max} = 0.0, 0.5, 1.0, 1.5, 2.0, 2.5, 3.0, 3.5$ nm (Fig. 5.8–bottom). In four of the five sparser dispersions, clusters form separate large but not quite network-spanning connected/rigid components when $\gamma_{max} > 0$ due to spatial separation of the clusters. Because the number of clusters scales with volume fraction, lesser separation of clusters in the $\phi_c = 0.003$ case allows the clusters to join together into one giant connected (rigid) component for $\gamma_{max} > 0.5$.

These heterogeneous results indicate that the spatial separation of clusters determines whether the CNT-crystal complexes form a globally rigid component, or whether they form an array of secondary rigid components. As mentioned above, these results are somewhat contrived and more sophistication is required to accurately capture the spatial heterogeneity of real material samples. However, I note that if the hypothesized presence of a globally rigid cluster is indeed responsible for brittleness, then the clustering of CNTs into these secondary agglomerates may actually have mechanical benefits. Even at very low CNT concentration, the homogeneous dispersions form a global spanning rigid component as γ_{max} reaches experimentally relevant quantities—whereas this is not necessarily so in heterogeneous dispersions. This hypothesis ought be considered in design of new experiments, as better dispersion quality may not then be the best avenue for optimizing mechanical properties.

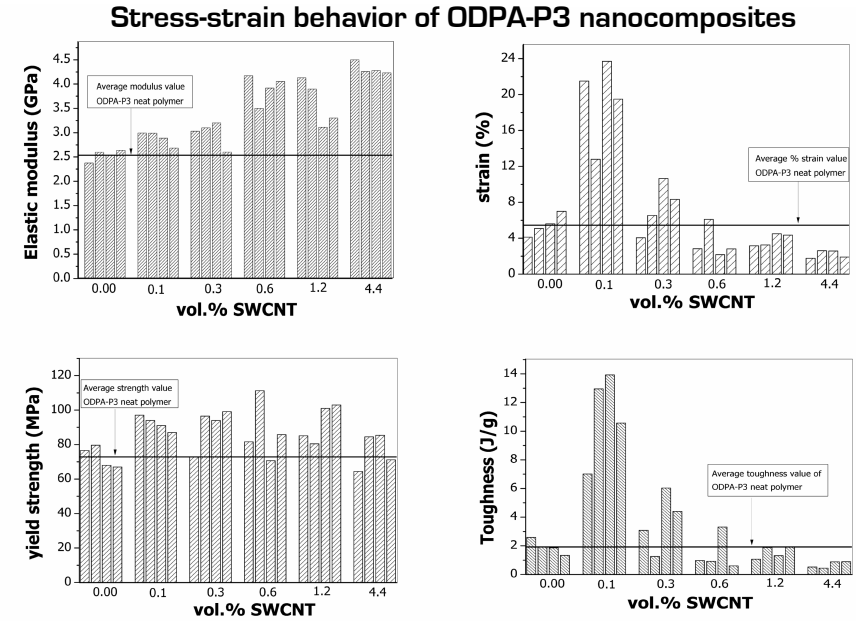

Figure 5.7: **Experimental characterization of nanocomposite strength.** Whereas experimental data shows clearly that increasing CNT vol % (or volume fraction) gives a higher modulus, the relationship between % CNTs and other mechanical properties are more complicated. In particular, the toughness and % strain at break both peak at $\phi_c = 0.001$ and then decline with higher CNT vol %. Tensile strength measurements do not indicate any clear dependence on vol %. Figure reproduced from Hegde et al. (2014).

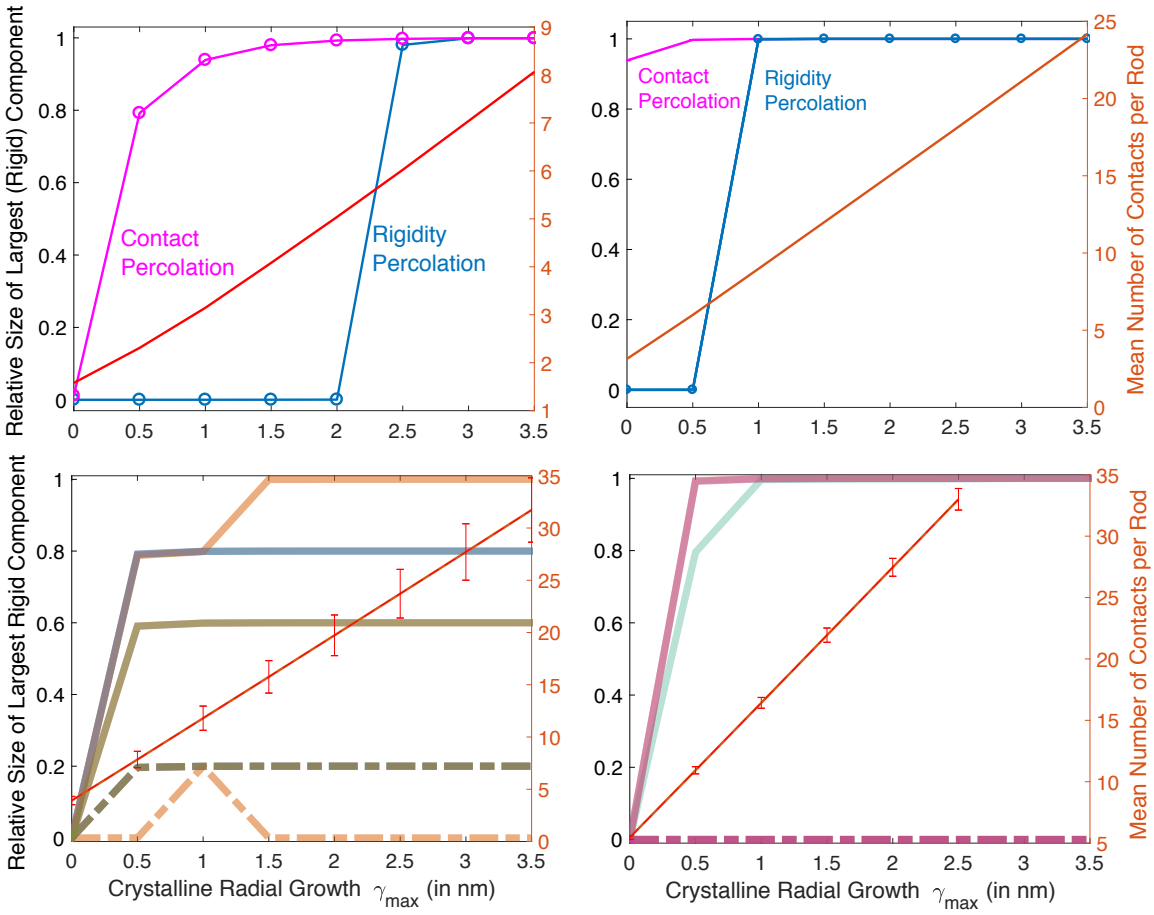

Figure 5.8: **Network Characterization of Crystallization about Homogeneous and Heterogeneous CNT Dispersions** *Top*: As polymer crystallizes around CNTs, more contacts (red line) facilitate the agglomeration of rod-crystal complexes into rigid components. First, the complexes form a giant connected component and then as the crystalline layers expand a giant rigid component. Each data point represents the average of results for five different simulations of rod dispersions with random position and orientation (*Left*: $\phi_c = 0.001$ nm, *Right*: $\phi_c = 0.003$ nm). *Bottom*: In clustered (Matérn) CNT dispersions (*Left*: $\phi_c = 0.001$ nm, *Right*: $\phi_c = 0.003$ nm), the proximity of CNTs gives rise to even higher mean contact numbers. Each blue curve here represents the rigidity analysis output of one simulation in which three clusters contain all CNTs in a 0.1% dispersion. If the clusters are isolated, the network condenses into five separate rigid components. Should these clusters intersect, these clustered rigid components may join into a lesser number rigid components. In the sparser case, only one of these (small) dispersions condense into one rigid component—but in the $\phi_c = 0.003$ case, less spatial separation between clusters allows these clusters to join into just one (rigid) component within each dispersion.

CHAPTER 6: CONCLUSIONS AND FUTURE DIRECTIONS

> Farewell! I leave you, and in you the last of humankind whom these eyes will ever behold. Farewell, Frankenstein! If thou wert yet alive and yet cherished a desire of revenge against me, it would be better satiated in my life than in my destruction. But it was not so; thou didst seek my extinction, that I might not cause greater wretchedness; and if yet, in some mode unknown to me, thou hadst not ceased to think and feel, thou wouldst not desire against me a vengeance greater than that which I feel. Blasted as thou wert, my agony was still superior to thine, for the bitter sting of remorse will not cease to rankle in my wounds until death shall close them forever. $\sim$ 'the monster'

The central goal of my doctoral study is to accurately characterize rigidity percolation in disordered 3D particle systems with hinge-like contacts. This dissertation describes its mathematical underpinnings (Ch. 2), the success of the root algorithm *RGC* in characterizing rigidity percolation in systems of disordered 2D fibers (Ch. 3), and promising results in application towards systems of disordered 3D fibers (Ch. 4). While this latter portion is not yet complete, the current work is sufficient for attaining an upper bound for the associated rigidity percolation threshold. Pending complete analysis of rigidity percolation in systems wherein fibers have uniformly random position and orientation, the next step is to apply this technique towards dispersions of realistic processing conditions.

I describe in the introduction the hypothesis that rigidity percolation underlies the dramatic gains ('mechanical' or 'rheological percolation') in various nanocomposites' mechanical properties seen at critical volume fractions above the corresponding electrical percolation thresholds. But as discussed in both Ch. 1 and Ch. 5, these real systems are far from the homogeneous ones considered in Ch. 3 and Ch. 4. Especially when the inclusions phase consists of carbon nanotubes, nanoparticle agglomeration is unavoidable and likely has importance consequences on the resulting network properties. Moreover, in Ch. 5, I illustrate this effect using simple clustering models wherein the increased local contacts facilitate the emergence of large rigid clusters at relatively low CNT volume fractions as compared to their homogeneous analogues. The cluster models used in the study, while perhaps valuable for their illustrating the effects of spatial heterogeneity on network properties, cannot reproduce the experimental images seen in real nanocomposites (see Fig. 6.1). Similar work

illustrates the effect of agglomeration on the contact percolation threshold (Seidel and Puydupin-Jamin, 2011; Gong et al., 2014; Tarlton et al., 2017). But, there is (as far as I have found) no study involving network properties of particle distributions learned from experimental data itself.

There is, however, much work in the more general task of reconstructing materials computationally from images. In one approach, pioneered by Yeong and Torquato (1998), the 2-point correlation function (for distance in pixels $0 < d < d_{max}$) of the inclusion phase is computed from images and denoted the target correlation function $\hat{f}(d)$. Then, the same correlation functions are computed for an initial 'trial' microstructure $f_0(d)$ and a simulated annealing procedure is used to evolve the trial microstructure towards the target, by minimizing an energy function $E = \sum_{i=0}^{d_{max}} [f_t(d_i) - \hat{f}(d_i)]^2$, for discrete pixel distance (or physical distance, if appropriate conversions are made) d_i. This procedure can readily be adapted to materials with more than one phase, and the minimization can certainly incorporate more than a single point correlation function (Torquato, 2002). A number of modifications have been made to adapt this method to a variety of heterogeneous materials (other than carbon nanocomposites)—in particular, an interesting adaptation relevant to the composite considered in Ch. 5 utilizes 'auxilary microstructures' throughout the energy minimization process to simulate real dynamical processes such as grain growth (Chen et al., 2015). Other studies use deep learning for the material reconstruction problem (see e.g. Cang et al. 2016), yet none consider carbon nanocomposites, possibly on account of the difficulty of reconstructing such a disordered system along with the difficulty of attaining appropriate images. However, even if the sharpness of the reconstruction would likely be underwhelming compared to those of other media, learning reconstructions even only at the mesocopic level (i.e. the size and distribution of agglomerates) can inform more realistic geometries and allow for exploration of their network properties, which are clearly very different from those of naive homogeneous dispersions. Future work in nanocomposite modeling would do well to pursue this data-oriented approach.

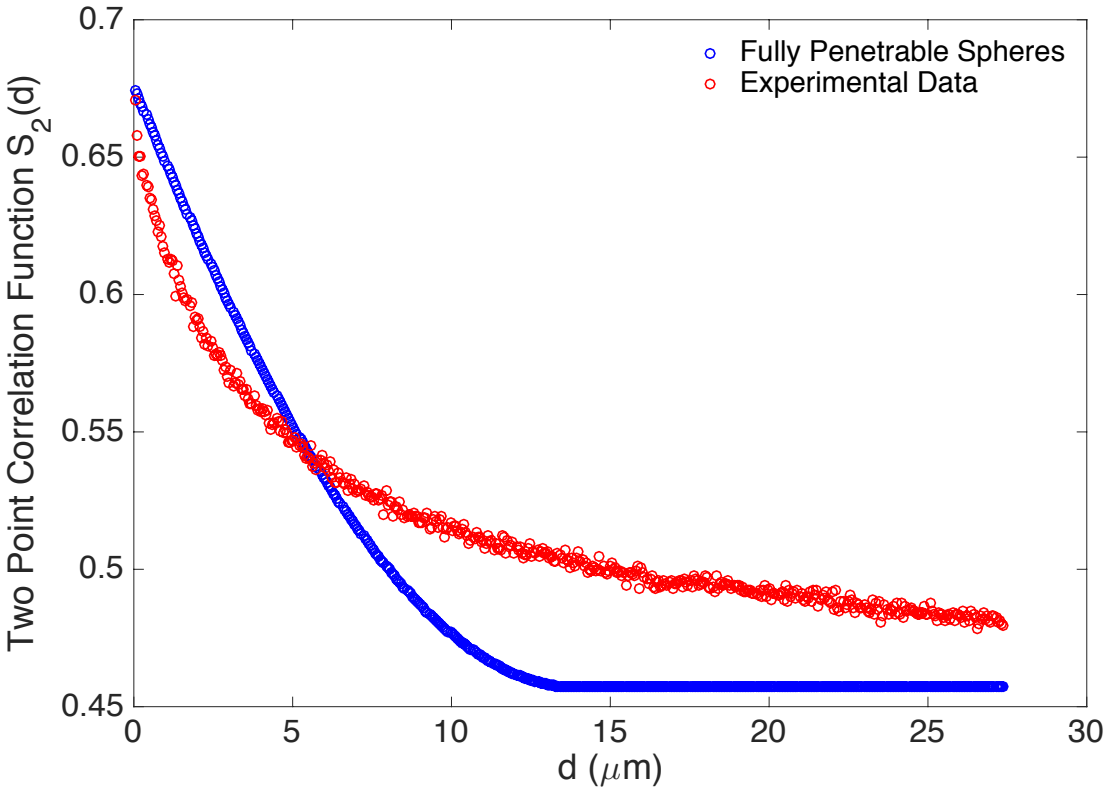

Figure 6.1: **A Poisson cluster process model cannot adequately model the carbon nanocomposite system of Ch. 5.** The 2-point correlation function for the pore-space between randomly packed, fully penetrable spheres has been derived by Torquato and Stell (1983) as a (discontinuous) function of the sphere radius and number density. Here, I use a genetic algorithm to minimize the pointwise distance between this two point correlation function (for the radial distance d in μm) to that computed from the experimental image shown in Fig. 5.2. Being that this is the best fit possible, a simple Poisson cluster process (of which this sphere packing is an idealization) likely cannot accurately capture the complexity of this real system.

BIBLIOGRAPHY

Affdl, J. and Kardos, J. (1976). The halpin-tsai equations: a review. *Polym. Eng. Sci.*, 16(5):344–352.

Alig, I., Potschke, P., Lellinger, D., Skipa, T., Pegel, S., Kasaliwal, G., and Villmow, T. (2012). Establishment, morphology and properties of carbon nanotube networks in polymer melts. *Polymer*, 53(1):4–28.

Balberg, I. (1986). Excluded-volume explanation of archie's law. *Phys. Rev. B*, 33(5):3618–3620.

Balberg, I. and Binenbaum, N. (1984). Percolation thresholds in the three-dimensional sticks system. *Phys. Rev. Lett.*, 52(17):1465–1468.

Baxter, S., Burrows, B., and Fralick, B. (2016). Mechanical percolation in nanocomposites: Microstructure and micromechanics. *Probabilist. Eng. Mech.*, 44:35–42.

Baxter, S. and Robinson, C. (2011). Pseudo-percolation: Critical volume fractions and mechanical percolation in polymer nanocomposites. *Composite Science and Technology*, 71(10):1273–1279.

Berhan, B. and Sastry, A. (2007). Modeling percolation in high-aspect-ratio fiber systems. i. soft-core versus hard-core models. *Phys. Rev. E*, 75(4):041120.

Buryachenko, V. (2007). *Micromechanics of Heterogeneous Materials*. Springer, New York, 1st edition.

Cang, R., Xu, Y., Chen, S., Liu, Y., Jiao, Y., and Ren, M. (2016). Microstructure representation and reconstruction of heterogeneous materials via deep belief network for computational material design. *J. Mech. Des.*, 139(7):071404.

Cederberg, J. (2001). *A course in modern geometries*. Springer, New York, 2nd edition.

Celzard, A., Krzesinska, M., Mareche, J., and Puricelli, S. (2001). Scalar and vectorial percolation in compressed expanded graphite. *Physica A*, 294(3–4):283–94.

Chen, S., Li, H., and Jiao, Y. (2015). Dynamic reconstruction of heterogeneous materials and microstructure evolution. *Phys. Rev. E*, 92(2):023301.

Chubynsky, M. and Thorpe, M. (2007). Algorithms for three-dimensional rigidity analysis and a first-order percolation transition. *Phys. Rev. E*, 76(4):041135.

Coleman, J., Cadek, M., Blake, R., Nicolosi, V., Ryan, K., Belton, C., Fonseca, A., Nagy, J., Gun'ko, Y., and Blau, W. (2004). High-performance nanotube-reinforced plastics: understanding the mechanism of strength increase. *Adv. Funct. Mater.*, 14(8):791–798.

Coleman, J., Khan, U., Blau, W., and Gun'ko, Y. (2005). Small but strong: A review of the mechanical properties of carbon nanotube-polymer composites. *Carbon*, 44(6430):1624–1652.

Coleman, J., Khan, U., Blau, W., and Gun'ko, Y. (2006). Small but strong: A review of the mechanical properties of carbon nanotube-polymer composites. *Carbon*, 44(9):1624–1652.

Connelly, R., Fowler, P., Guest, S., Schulze, B., and Whitely, W. (2009). When is a symmetric pin-jointed framework isostatic? *Int. J. Solids Struct.*, 46(3–4):762–773.

Cucuringu, M., Singer, A., and Cowburn, D. (2012). Eigenvector synchronization, graph rigidity and the molecule problem. *Information and Inference*, 1(1):21–67.

De Volder, M., Tawfek, S., Baughman, R., and Hart, A. (2013). Carbon nanotubes: Present and future commercial applications. *Science*, 339(6119):535–539.

Favier, V., Canova, G., Shrivastava, S., and Cavaillé, J. (1997). Mechanical percolation in cellulose whisker composites. *Polym. Eng. Sci.*, 37(10):1732–1739.

Favier, V., Chanzy, H., and Cavaillé, J. (1995a). Polymer nanocomposites reinforced by cellulose whiskers. *Macromolecules*, 28(18):6365–67.

Favier, V., Chanzy, H., and Cavaillé, J. (1995b). Small but strong: A review of the mechanical properties of carbon nanotube-polymer composites. *Macromolecules*, 28(18):6365–6367.

Forest, M., Wang, Q., and Zhou, R. (2004). The flow-phase diagram of doi-hess theory for sheared nematic polymers ii: Finite shear rates. *Rheol. Acta*, 44(1):80–93.

Forest, M., Wang, Q., and Zhou, R. (2008). The weak shear kinetic phase diagram for nematic polymers. *Rheol. Acta.*, 43(1):17–19.

Fralick, B., Gatzke, E., and Baxter, S. (2012). Three-dimensional evolution of mechanical percolation in nanocomposites with random microstructure. *Probabilist. Eng. Mech.*, 30(3):1–8.

Gluck, H. (1975). Almost all simply connected closed surfaces are rigid. *Geometric Topology, Lecture Notes in Mathematics*, 438:225–239.

Gong, S., Zhu, Z., Li, J., and Meguid, S. (2014). Modeling and characterization of carbon nanotube agglomeration effect on electrical conductivity of carbon nanotube polymer composites. *J. Appl. Phys.*, 116(19):194306.

Graver, J. (1991). Rigidity matroids. *SIAM J. Discrete Math.*, 4(3):355–368.

Hagberg, A., Schult, D., and Swart, P. (2008). Exploring network structure, dynamics, and function using networkx. In Varoquaux, G., Vaught, T., and Millman, J., editors, *Proceedings of the 7th Python in Science Conference (SciPy2008)*, pages 11–15. Pasadena, CA.

Head, D., Levine, A., and MacKintosh, F. (2003a). Deformation of cross-linked semiflexible polymer networks. *Physical Review Letters*, 91(10):108102.

Head, D., Levine, A., and MacKintosh, F. (2003b). Distinct regimes of elastic response and deformation modes of cross-linked cytoskeletal and semiflexible polymer networks. *Physical Review E*, 68(6):061907.

Hegde, M. (2014). *Design and Properties of SWCNT-Polyetherimide nanocomposites*. PhD thesis, Delft University of Technology.

Hegde, M., LaFont, U., Norder, B., Picken, S., Samulski, E., Rubinstein, M., and Dingemans., T. (2013). Swcnt induced crystallization in an amorphous all-aromatic poly(ether imide). *Macromolecules*, 46(4):1492–1503.

Hegde, M., LaFont, U., Norder, B., Samulski, E., Rubinstein, M., and Dingemans., T. (2014). Swcnt induced crystallization in amorphous and semi-crystalline poly(etherimide)s: Morphology and thermo-mechanical properties. *Polymer*, 55(16):3746–3757.

Hegde, M., Samulski, E., Rubinstein, M., Pickten, S., and Dingemans., T. (2015). The role of crystallinity in swcnt-polyetherimide nanocomposites. *Compos. Sci. Technol.*, 110:176–187.

Hendrickson, B. (1992). Conditions for unique graph realizations. *SIAM J. Comput.*, 21(1):65–84.

Henneberg, L. (1911). *Die Graphische Statik der Starren Systeme*. B.G. Teubner, Leipzig, 1st edition.

Huisman, E. and Lubensky, T. (2011). Internal stresses, normal modes, and nonaffinity in three-dimensional biopolymer networks. *Langmuir*, 106(8):088301.

Iijima, S. and Ichihashi, T. (1993). Single-shell carbon nanotubes of 1-nm diameter. *Nature*, 363(9):603–605.

Jacobs, D. and Hendrickson, B. (1997). An algorithm for two-dimensional rigidity percolation: the pebble game. *J. Comput. Phys.*, 137(2):346–365.

Jacobs, D. and Thorpe, M. (1995). Generic rigidity percolation: The pebble game. *Phys. Rev. Lett.*, 75(22):4051–4054.

Kalia, S., Dufresne, A., Cherian, B., Kaith, B., Avrous, L., Njuguna, J., and Nassiopoulos, E. (1976). Cellulose-based bio- and nanocomposites: A review. *Int. J. of Polym. Sci.*, 16(5):344–352.

Kallmes, O. and Corte, H. (1960). Structure of paper i. the statistical geometry of an ideal two dimensional fiber network. *TAPPI*, 43(9):737–752.

Laird, E. and Li, C. (2013). Structure and morphology control in crystalline polymer?carbon nanotube nanocomposites. *Macromolecules*, 46(8):2877–2891.

Laman, G. (1970). On graphs and rigidity of plane skeletal structures. *J. Eng. Math.*, 4(4):331–340.

Latva-Kokko, M. and Mäkinen, J. (2001). Rigidity of random networks of stiff fibers in the low-density limit. *Phys. Rev. E*, 64(6):066117.

Latva-Kokko, M., Mäkinen, J., and Timonen, J. (2001). Rigidity transition in two-dimensional random fiber networks. *Phys. Rev. E*, 63(4):046113.

Liu, Y., He, X., Hanlon, D., Harvey, A., Khan, U., Li, Y., and Coleman, J. (2016). Electrical, mechanical, and capacity percolation leads to high performance mos_2/nanotube composite lithium ion battery electrodes. *ACS Nano*, 10(6):5980–5990.

Ma, X., Zare, Y., and Rhee, K. (2017). A two-step methodology to study the influence of aggregation/agglomeration of nanoparticles on young's modulus of polymer nanocomposites. *Nanoscale Res. Lett.*, 12(621):1–7.

Maxwell, J. (1864). On the calculation of the equilibrium and stiffness of frames. *Philosophical Magazine*, 27(182):294–299.

Niklaus, M. and Shea, H. (2011). Electrical conductivity and young's modulus of flexible nanocomposites made by metal-ion implantation of polydimethylsiloxane: The relationship between nanostructure and macroscopic properties. *Acta Materialia*, 59(2):830–840.

Noël, A., Faucheu, J., Chenal, J., Viricelle, J., and Bourgeat-Lami (2014). Electrical and mechanical percolation in graphene-latex nanocomposites. *Polymer*, 55(20):5140–5145.

Ouali, N., Cavaillé, J., and Pérez, J. (1991). Elastic, viscoelastic and plastic behavior of multiphase polymer blends. *J. Plast., Rubber Comp. Process. Appl.*, 16(55):5560–72.

Palla, G., Derényi, I., Farkas, I., and Vicsek, T. (2005). Uncovering the overlapping community structure of complex networks in nature and society. *Nature Letters*, 435(7043):814–818.

Penu, C., Hu, G., Fernandez, A., Marchal, P., and Choplin, L. (2012). Rheological and electrical percolation thresholds of carbon nanotube/polymer nanocomposites. *Polym. Eng. Sci.*, 52(10):2173–81.

Philipse, A. (1996). The random contact equation and its implications for (colloidal) rods in packings, suspensions, and anisotropic powders. *Langmuir*, 12(5):1127–1133.

Phillips, J. and Thorpe, M. (1985). Constraint theory, vector percolation and glass formation. *Solid State Commun.*, 53(8):699–702.

Pike, G. and Seager, C. (1974). Percolation and conductivity: A computer study. i. *Phys. Rev. B*, 10(4):1421–1434.

Qiao, R. and Brinson, L. (2009). Simulation of interphase percolation and gradients in polymer nanocomposites. *Composite Science and Technology*, 69(3–4):491–499.

Seidel, G. and Puydupin-Jamin, A.-S. (2011). Analysis of clustering, interphase region, and orientation effects on the electrical conductivity of carbon nanotube?polymer nanocomposites via computational micromechanics. *Mechanics of Materials*, 43(12):755–774.

Shi, F., Wang, S., Forest, M., and Mucha, P. (2013). Percolation-induced exponential scaling in the large current tails of random resistor networks. *Multiscale Model. Simul.*, 11(4):1298–1310.

Shi, F., Wang, S., Forest, M., and Mucha, P. (2014). Network-based assessments of percolation-induced current distributions in sheared rod macromolecular dispersions. *Multiscale Model. Simul.*, 12(1):249–264.

Silva, J., Simoes, R., Lanceros-Mendez, S., and Vaia, R. (2011). Applying complex network theory to the understanding of high-aspect-ratio carbon-filled composites. *Europhys. Lett.*, 93(3):37005.

Simoes, R., Silva, J., Vaia, R., Sencadas, V., Costa, P., Gomes, J., and Lanceros-Méndez, S. (2008). Low percolation transitions in carbon nanotube networks dispersed in a polymer matrix: dielectric properties, simulations and experiments. *Nanotechnology*, 20(3):035703.

Stauffer, D. and Aharony, A. (1992). *Introduction to Percolation Theory*. Taylor & Francis, Washington, DC, 2nd edition.

Tarlton, T., Sullivan, E., Brown, J., and Derosa, P. (2017). The role of agglomeration in the conductivity of carbon nanotube composites near percolation. *J. Appl. Phys.*, 121(8):085103.

Tay, T. and Whitely, W. (1985). Generating isostatic frameworks. *Structural Topology*, 11:21–69.

Thorpe, M., Jacobs, D., Chubynsky, N., and Rader, A. (1999). Generic rigidity of network glasses. In Thorpe, M. and Duxbury, P., editors, *Rigidity Theory and Applications*, pages 239–77. Plenum Publishing, NY.

Torquato, S. (2002). *Random Heterogeneous Materials*. Springer, New York, 1st edition.

Torquato, S. and Stell, G. (1983). Microstructure of two?phase random media. iii. the n?point matrix probability functions for fully penetrable spheres. *J. Chem. Phys.*, 3(79):1505–1510.

Viot, P., Tarjus, G., Ricci, S., and Talbot, J. (1992). Random sequential adsorption of anisotropic particles. i. jamming limit and asymptotic behavior. *J. Chem. Phys.*, 97(7):5212–5218.

Wilhelm, J. and Frey, E. (2003). Elasticity of stiff polymer networks. *Phys. Rev. Lett.*, 91(10):108103.

Yeong, C. and Torquato, S. (1998). Reconstructing random media. *Phys. Rev. E*, 57(1):495–506.

Zhang, J., Jiang, D., and Peng, H. (2013). Two-stage mechanical percolation in the epoxy resin intercalculated buckypaper with high mechanical performance. *RSC Advances*, 3(35):15290–15297.